LBNL-39588
UC-404

ERNEST ORLANDO LAWRENCE
BERKELEY NATIONAL LABORATORY

Joining of Silicon Carbide using Interlayer with Matching Coefficient of Thermal Expansion

T. Perham
Materials Sciences Division

November 1996
M.S. Thesis

LBNL 39588

Joining of Silicon Carbide using Interlayer with Matching Coefficient of Thermal Expansion

Tim Perham

Department of Materials Science and Mineral Engineering
University of California

and

Center for Advanced Materials
Materials Sciences Division
Lawrence Berkeley National Laboratory
University of California
Berkeley, CA 94720

November 1996

This work was supported by the Director, Office of Energy Research, Office of Basic Energy Sciences, Materials Sciences Division, of the U.S. Department of Energy under Contract No. DE-AC03-76F00098.

Joining of Silicon Carbide Using Interlayer with Matching Coefficient of Thermal Expansion

by

Timothy James Perham

B.S. (University of Arizona) 1990

A thesis submitted in partial satisfaction of the

requirements for the degree of

Master of Science

in

Engineering:

Materials Science and Mineral Engineering

in the

GRADUATE DIVISION

of the

UNIVERSITY of CALIFORNIA, BERKELEY

Committee in charge:

Professor L.C. DeJonghe
Professor R.O. Ritchie
Dr. A.P. Tomsia

1996

Joining of Silicon Carbide Using Interlayer with
Matching Coefficient of Thermal Expansion

Table of Contents

Table of Figures

Table of Tables

The author gratefully acknowledges Dr. Warren MoberlyChan for contributing the TEM work in this project; and Dr. Ian Brown for the ion-implantation of silicon carbide substrates.

Chapter 1 Background and Objectives

1.1 Silicon Carbide Ceramics

Silicon Carbide (SiC) is a key ingredient in the refractory, metalworking, and abrasive industries. It is also used in the manufacture of heat exchangers, superfine grinding wheels, metal-matrix composites, polishing slurries, and many specialized technical designs requiring high refractoriness and high hardness and wear resistance. In recent years SiC and SiC matrix composites have received considerable attention as potential high temperature structural materials. Silicon carbide retains its strength at high temperature, and has good oxidation, corrosion, and thermal shock resistance. It has been considered as a potential material for high efficiency diesel and turbine engines. Piston crowns, valve seats, exhaust valves, fuel nozzles, and turbocharger wheels are examples of components in which the high temperature properties of SiC might be exploited. Since SiC possesses good environmental stability it has been discussed for use in ultra high temperature combustion chambers, and as nuclear fusion reactor insulator rings.[1,2]

These advantageous material properties are largely due to the nature of bonding in SiC. SiC will assume either the zinc blende or wurtzite crystal structure, both of which are tetrahedrally coordinated covalent solids. Due to the strong covalency, the bond length is short (1.88 Å) and the cohesive energy per bond high. Because the bonding is highly directional and the coordination number of 4 is low, the atomic packing density, and thus the bulk density, is low (3.21 g/cc), allowing for greater thermodynamic efficiency in energy conversion processes. Its low (compared to metals) thermal conductivity allows for greater efficiencies associated with reduced cooling requirements.

Due to the high cohesive energy, SiC is extremely stable to most corrosives, and the formation of a dense SiO_2 oxidation product layer makes it relatively oxidation resistant. The high interatomic forces present give SiC a low coefficient of thermal expansion and good thermal shock resistance, allowing for tighter design tolerances in high temperature applications. The strong bond directionality leads to a very high elastic modulus (> 600 GPa), and thermally induced crack tip relaxation gives it the best high temperature strength of any material.[3] However, the same high strength bonding and directionality that lead to high mechanical strength and good high temperature properties also produce high lattice drag to dislocation motion, making SiC very brittle. Hence the possibility of catastrophic failure has severely restricted the use of SiC in mechanical design applications.

The high interatomic forces present in SiC also make this material very difficult to process, as they give rise to low defect concentrations and low diffusion coefficients. Densification is difficult because of the low thermodynamic driving force for sintering due to the small free energy difference between the individual particle surface energy and the grain boundary energy of a sintered body.[4] Until 1977 it was not feasible to densify SiC without the use of high external pressure. The difficulties surrounding the sintering process make producing complex shapes very expensive and time consuming, as extensive machining and non-destructive testing are required. However, simple hot-pressed components with superior properties (such as bars, tubes, and discs) can be economically manufactured and proof tested, enabling the fabrication of a complex part where the joint between the parts has a far higher probability of failure than the base materials. Thus ensuring reliability becomes possible and rework becomes feasible from a

manufacturability standpoint. It therefore remains to develop techniques for making complex parts out of simple shapes without compromising the performance of the joined ceramic.

1.2 Joining

For widespread application of specifically engineered advanced materials equally advanced joining techniques are needed: to meet the size and/or shape requirements of complex designs, to optimize materials and reduce waste, and to tailor properties to improve performance by combining different materials.[5] The joining process must be developed so that the advanced properties of the materials to be joined are preserved after the joint is formed. The selection criteria for a joining method must encompass the requirements for strength, service temperature, reliability, hermeticity, environmental stability, rework, non-destructive testing, and low cost.[6]

The three fundamental methods for joining materials are 1) mechanical fastening; 2) adhesive bonding; and 3) welding. They differ primarily in the degree and type of chemical bonding effecting the join. In mechanical fastening, only the physical forces (both static and frictional) on the components are utilized. Devices such as rivets, pins, screws, and bolts are required, although joining without fasteners by way of interlocking designs and shrinkfitting is also possible. This technique allows for joining without changing the composition of the base materials, and for easy disassembly and rework. In adhesive bonding, the primary mechanism for bonding is the formation of weak secondary bonds (e.g. Van der Waals) where the bonding does not seriously disrupt the composition or structure. Glues and epoxy resins represent the majority of adhesives finding

widespread usage. In welding, a strong primary bond is formed which significantly alters the composition, structure, and properties of the materials being joined. Soldering and brazing are low temperature welding processes wherein a molten filler flows into the joint area, wets the substrate, and forms chemical bonds without melting the base materials. In metals, the bonds formed are metallic solid solutions or intermetallics; in ceramics they are ionic or ionic/covalent. Fusion bonding requires high temperatures and is characterized by the formation of welds with compositions and/or structures completely distinct from either of the base materials. The joint assumes the morphology and composition dictated by the solidifying weld pool. In diffusion bonding the base materials are brought into intimate contact under high pressure and temperature causing bonding via solid state diffusion.

1.3 Joining of Silicon Carbide

Four of the most promising technologies being investigated for joining SiC are 1) active metal brazing; 2) brazing with oxide frit; 3) reaction bonding; and 4) diffusion bonding. Active metal brazing has been used successfully with Cu-Ti, Ni-Ti, and Cu-Ag-Ti alloys, among others. The advantages of this technique are that a ductile metal interlayer is used to alleviate thermal stresses during processing, and active metals such as Ti react and wet SiC thoroughly. The disadvantages are that high temperature strength and oxidation resistance is limited by the metals used, and an intermediate metallization process is sometimes required. Strong joints using oxide frit brazes have been reported based on oxynitride glass of the basic composition Si_3N_4-Y_2O_3-La_2O_3-MgO. This technique exploits the intrinsically better strength and stability of oxides in an oxidizing atmosphere, but utilizes a low toughness interlayer that does not aggressively wet SiC.

Relatively high strength joints which show little reduction in strength at temperatures approaching 1200°C have been achieved via a reaction bonding process using a Si-SiC-C interlayer. In this method a reaction bonded SiC joint is produced which very closely matches both the coefficient of thermal expansion and elastic modulus of the base material. But the excess metal present leads to questionable oxidation resistance and microcracking under neutron irradiation. Diffusion bonding techniques have yielded the highest strength values reported, greater than 80% of the rupture strength of the original SiC bodies. The advantages of this technique include the high strength obtainable, and the process design similarity to sintering. The disadvantages include the necessity for external pressure and high temperature, limited geometry, high flatness and finish requirements, and the formation of brittle intermetallic reaction byproducts (for bonding to metals). Table 1 summarizes some of the reported research on the joining of SiC.

Table 1-1 Summary of SiC Joining

Base Materials	*Interlayer*	*Atmosph.*	*Temp. (°C)*	*Pressure (MPa)*	*Strength (Mpa)*	*Comments*	*Reference*
			Active Metal Brazing				
SiC	Ge	VAC	1180	N/A	200		7
SiC	Al	VAC	800-1000	N/A	120-250	Al_4C_3	8
SiC	Cu-35Mn	Argon	870	0.5	150		9
SiC	Cu-Ti	VAC	1000	N/A	64-80	TiC,Ti_5Si_3	10
SiC	Ni-Ti	VAC	1250	N/A	60		10
SiC	Cu-Ag-Ti	VAC	950	N/A	386		11
			Oxide Frit Brazing				
SiC	Kaolin	Air	1500	N/A	130	CaF_2 flux	12
SiC	Oxynitride	Argon	1700	N/A	400	glass	13
SiC	PbO-B_2O_3-SiO_2	Air	1150	N/A	67	Kaolin glaze	14
SiC	MgO-Al_2O_3-SiO_2	Air	1100	N/A	8	Glass-Ceramic	15
			Reaction Bonding				
SiC	Ti-C-Ni	Argon	1400	20-50	N/A	TiC + Ni	16
SiC	Si-SiC-C	VAC	1480	N/A	340		17
			Diffusion Bonding				
SiC	SiC-YAG	VAC	1900-2000	25	350		18
SiC	Mg or Al	UH VAC	25	0	not spec.	surf. finish	19
SiC	None	VAC	1200	40	270		20
SiC	SiC-Al-B-C	Argon	1650	50	400-540		21
SiC	Ti	VAC	1500	0.6	300		22
KOVAR	Al-10Si	VAC	610	10	100		23
Nimonic 80	Al	VAC	610	13	60		24
Inconel 718	None	VAC	1160	103	120-140		25

1.4 Objectives

The primary objective of this study is to develop a technique for joining a commercially available Silicon Carbide that gives good room temperature strength and the potential for good high temperature strength. One secondary objective is that the joining technique be adaptable to SiC_f/SiC composites and/or Nickel based superalloys, and another secondary objective is that the materials provide good neutron irradiation resistance and low activation for potential application inside nuclear fusion reactors.

1.5 References

1. M. Ferraris, C. Badini, M. Montorosi, P. Appendino, and H. W. Scholz, "Joining of SiC_f/SiC Composites for thermonuclear fusion reactors," *J. Nuclear Materials*, **212-215** 1613-16 (1994).
2. M. Ward and J. Napier, "Development of a Ceramic Tube Heat Exchanger with Relaxing Joint," DOE Tech. Report FE-2556-17, (1978).
3. K. Yamada and M. Mohri, "Properties and Applications of Silicon Carbide Ceramics," in Silicon Carbide Ceramics--1, edited by S. Somiya and Y. Inomata, Elsevier Applied Science, New York (1991), 37-41.
4. J. Cao, "In Situ Toughened SiC Ceramics with Al-B-C Additions and Oxide-Coated SiC Platelet/SiC Composites," Ph.D. Thesis, University of California at Berkeley, (1996).
5. R. Messler, Jr., "Joining of Advanced Materials," *SAMPE* Journal, **31** [2] 41-45 (1995).
6. R. Rice, "Joining of Ceramics," in Advances in Joining Technology, edited by J. Burke, A. Gorum, and A. Tarpinian, Brook Hill Pub. Co., Massachusetts (1976), 69-111.
7. T. Iseki, K. Yamshita, and H. Suzuki, "Joining of self-bonded SiC containing free silicon by germanium metal," *Yogyo-Kyokai-Shi*, **89** [4] 171-5 (1981).
8. T. Iseki, K. Yamashita, and H. Suzuki, "Joining of dense Silicon Carbide by aluminum metal, Yogyo-Kyokai-Shi, **91** [1] 1-6 (1983).

9. H. Okamura, K. Miyazaki, and K. Matsuzaka, "Bonding of SiC ceramics to copper and thermal characteristics of bonding elements," *Quart. J. Japan Weld. Soc.*, **4** [2] 476-83 (1986).

10. M Naka, T. Tanaka, and I. Okamoto, "Joining of SiC using amorphous titanium filler metal," *J. High Temp. Soc. (Japan)*, **12** [2] 81-9 (1986).

11. J. Boadi, K. Yano, and T. Iseki, "Brazing of pressureless-sintered SiC using Ag-Cu-Ti Alloy," *J. Mater. Sci.*, **22** [7] 2431-34 (1987).

12. Y. Ebata, Y. Fuji, and R. Hayami, "Development and applications of inorganic adhesive for non-oxide ceramics, *Eng. Mater. (Japan)* **31** [1] 101-5 (1983).

13. N. Tamari, M. Honda, and M. Ebata, "Joining of SiC Ceramics with Si_3N_4-Y_2O_3-La_2O_3-MgO mixture, *Yogyo-Kyokai-Shi*, **94** [10] 1087-91 (1986).

14. L. Lay, A. Morrell, and R. Wallis, "Joining 'REFEL' silicon carbide to porcelain," *Brit. Ceram. Proc.*, No. 34 231-9 (1984).

15. D. Coon, "Vitreous joining of SiC fiber reinforced SiC composites," DOE Technical Report NTIS DE90-01295 (1989).

16. B. Rabin, "Joining of fiber-reinforced SiC composites by *in situ* reaction methods," *Mat. Sci. Eng.*, **A130** L1-L5 (1990).

17. B. Rabin and G. Moore, "Reaction processing and properties of SiC-to-SiC joints," in Joining and Adhesion of Advanced Inorganic Materials, edited by A. Carim, D. Schwartz, and R. Silberglitt, *Mater. Res. Soc. Symp. Proc.*, **314** 197-203 (1993).

18. A. Gehris Jr, "High Temperature Bonding of Silicon Carbide," M.S. Thesis, New Mexico Institue of Mining and Technology, Socorro, NM, (1989).

19. H. Pries and J. Ruge, "Welding of heterogeneous materials without a liquid phase," *DVS-Berichte*, **66** 9-14 (1980).

20. R. Rottenbacher and G. Willmann, "Diffusionsschweissen von siliziumcarbid," *Z. Werkstofftech*, **12** 227-29 (1981).

21. T. Iseki, K. Arakawa, and H. Matsuzaki, "Joining of dense silicon carbide by hot-pressing," *Yogyo-Kyokai-Shi*, **91** [8] 349-54 (1983).

22. S. Morozumi, M. Endo, and M. Kikuchi, "Bonding mechanism between silicon carbide and thin foils of reactive metals," *J. Mater. Sci.*, **20** [11] 3976-82 (1985).

23. A. Kohno, T. Yamada, and K. Yokoi, "Bonding of ceramics to metals with interlayers of Al-Si Clad aluminum," *J. Japan Inst. Metals*, **49** [10] 876-83 (1985).

24. T. Yamada, H. Sekiguchi, and H. Okamoto, *Nippon Kokan Technical Report*, No. 113 60-67 (1986).

25. S. Moseley and R. Walker, "The Diffusion Bonding of Engineering Ceramics to Nickel Based Superalloys by Hot Isostatic Pressing," in Diffusion Bonding--2, edited by D. Stephenson, Elsevier Applied Science, New York, 183-99 (1991).

Chapter 2 Methodology and Materials Selection

2.1 Background

Methods for producing high strength SiC joints often operate at temperatures and pressures which would degrade the SiC fibers in ceramic matrix composites, cause degradation of in-situ toughened materials due to uncontrolled microstructural evolution, or melt a Nickel based superalloy. Moreover, the constraints imposed by the processing conditions required often limit the geometric design of the base materials. Environmental stability is of concern when the technique involves the use of a reactive metal, which may limit the corrosion and oxidation resistance, or leave excess unreacted metal which may lead to loss of strength under high temperature and/or neutron irradiation.[1]

Nicalon fibers used in the fabrication of SiC_f/SiC CMC's are known to degrade at temperatures above 1200°C,[2] although recent work has indicated that strength can be maintained to 1400°C by first coating the fibers with carbon.[3] Superalloys such as Inconel 600 and Inconel 718 melt at temperatures above 1260-1354°C, and lose the advanced properties associated with dispersion strengthening at 0.80 T_m. Since the service temperature projected for these materials approaches or exceeds 1000°C, the temperature range for the joining process is limited. Some attempts have been made to process a low temperature joint which can withstand a higher service temperature by way of a partial transient liquid phase.[4] Other attempts include the use of a crystallizable glass to improve the refractoriness of the resultant joint.[5,6]

2.2 Methodology

A successful joint can be achieved if the following conditions are met: 1) an intimate contact interface is formed; 2) a chemical and/or solid state reaction proceeds at the interface leading to the formation of compatible equilibrium phases; and 3) thermal stress relaxation during processing and use allows for a reliable joint.[7] During this study, several candidate materials were evaluated based on one or more of these criterion, employing a low temperature low pressure processing route, and the most promising, a cordierite glass-ceramic, was selected for more detailed investigation.

2.3 Materials selection

2.3.1 Reaction bonding with Al-Si/Si/SiC/C

2.3.1.1 Background

During reaction bonding, metallic silicon and carbon in the form of carbon black are placed in contact in the joint and reaction allowed to proceed to the liquid state. SiC particles are dispersed throughout the mixture to provide nucleation sites for the growth of SiC. The process must be carried out above the melting point of Si (1414°C) and excess silicon must be available to ensure complete reaction. Two problems generally arise during processing; 1) development of local porosity; and 2) Si segregation to the interface. In this study, an attempt was made to address these issues while at the same time lowering the processing temperature.

It is well known that aluminum metal acts as a sintering aid for densifying SiC by providing a liquid phase which promotes mass transport.[8] This liquid phase also promotes

particle rearrangement by a process such as described by the classic theory of liquid phase sintering. The included secondary phases which develop, however, are quite large, because of the unavailability of aluminum metal powders as small as the starting SiC powders.[9] Using an 88/12 eutectic Al-Si alloy presents the possibility of grinding the aluminum to a smaller grain size for better dispersion throughout the matrix, promoting better distribution of reactants in the liquid phase and lower final porosity. This could also, in principle, lower the tendency of brittle silicon to segregate to the interface by forming a silicon rich transient liquid phase which prefers solid solution with aluminum over reaction with SiC. Referring to the Al-Si binary phase diagram in Figure 2-1, increasing the silicon content of the system results in a single phase liquid with increasingly higher melting point. It should therefore be possible to produce a transient liquid phase with a reduced liquidus temperature with respect to pure silicon.

2.3.1.2 Experimental procedure

a. Grinding of Al-Si alloy

An eutectic Al-Si alloy[i] was mixed with hexane and placed in a planetary ball mill[ii] with zirconia balls. Samples were retrieved after 1, 2, and 4 hours and examined with an optical microscope at 500X magnification. Particle shear was severe even after only 1 hour milling time, with 200 micron diameter flakes resulting. Milling at longer times only served to increase the flattening effect. It was concluded that the original 45 micron

[i] Alfa Aesar; Ward Hill, MA

[ii] Duke Scientific Corp.; Palo Alto, CA

powders would be more advantageous for homogeneity during processing. Cryogrinding remains as an unexplored possibility for reducing the Al-Si particle size.

b. Film deposition and firing

A solvent binder system similar to the one chosen by Rabin[10] was used to deposit thick layers (~ 1 mm) of the reaction bonding mixture directly on fine polished (1μ) SiC substrates. Table 2-1 lists the composition and characteristics of the powder mixture used, and Table 2-2 the slip formulations used for the tape casting process.

Table 2-1 Composition and characteristics of tape casting powder mixture

Composition	*Description*	*Particle size (μm)*	*Content (wt. %)**
SiC	beta[i]	0.15	34.7
Si	99.999 %[ii]	1-5	39.9
Al-Si	88/12 eutectic[iii]	45	6.1
C	Acetylene black[iv]	.02	19.2

* Percentages based on formation of 75/25 Si/Al solid solution and eventual conversion of Al to Al_4C_3 and Si and C to SiC

[i] H.C. Starck; Berlin, Germany

[ii] Alfa Aesar; Ward Hill, MA

[iii] Alfa Aesar; Ward Hill, MA

[iv] Chevron Chemical Company; Baytown, TX

Table 2-2 Slip formulation for tape casting

Material	*Function*	*Parts by weight*[*]
Powder mixture	Joint material	100
2-Butanone (MEK)	Solvent	150
Menhaden fish oil[i]	Dispersant	5
Tertiary amide polymer[ii]	Binder	12
Glycerol	Plasticizer	1

It was important to keep the viscosity of the mixture as high as possible to prevent the metallic particles from settling. This was accomplished by starting with a thin slurry and stir drying the mixture until the highest viscosity possible was obtained that still enabled casting (approx. 1.0 g/ml of solids). This mixture was deposited directly onto the SiC substrates with a doctor blade on a surface ground steel plate (the plate was drilled out to allow for a .001" slip fit with the substrate). The parts to be joined were heated in air (3°C/min) to 400°C for 4 hours to remove the organics, loaded into a graphite die, and heated in argon in a graphite element furnace first to 700°C for 4 hours for the homogenization process, then to 1450°C for 30 minutes. Another part, containing a powdered mixture of pure silicon, was processed simultaneously to verify melting.

[*] Relative to weight of starting powder mixture

[i] Sigma Chemical Company; St. Louis, MO

[ii] Dow Chemical Company; Midland, MI

2.3.1.3 Results and Discussion

Although the joint containing only silicon did melt and form a bond, neither the joint of the composition listed in Table 2-1 nor a subsequent one made with 25% of excess silicon formed a bond. X-ray diffraction of the material removed from the joint (see Fig. 2-2) revealed the presence of β-SiC along with a minute amount of α. No metallic silicon or aluminum was indicated. The strong diffuse x-ray scattering at ≈ 7 Å is typically associated with silica. The small peak at 3.504 Å could be associated with alumina, but is probably due to trace contaminants in the starting SiC powders. Since no silicon was available to wet the substrate, it is reasonable to assume that it either infiltrated the substrate or was consumed in the liquid phase by the formation of an amorphous phase and/or SiC. Another possibility is that the original silicon powders were severely oxidized; but this did not prevent the control part from joining.

Referring to the SEM micrograph in Figure 2-3, very little infiltration of the silicon into the substrate was observed. Since most of the work reported on reaction bonding utilizes large lumps of metallic silicon during processing, it is possible that the capillary action accompanying infiltration is necessary for the reaction to proceed. The inability to form an intimate interface contact with silicon carbide precluded further investigation of this technique.

2.3.2 Reaction/infiltration with Calcium Aluminum Silicate

2.3.2.1 Background

In the CaO-Al_2O_3-SiO_2 (CAS) phase diagram of Figure 2-4, ternary eutectics at 1265 and 1170°C are evident as possible compositions for the formation of a framework

matrix of a SiC particle reinforced glass, to be used in joining SiC or in the fabrication of a graded joint between SiC and a metal. The thermal and elastic mismatches present in the system may be alleviated by controlling the amount of SiC and/or metal present in the composite interlayer. Since the solubility of a silicate glass in SiC at low temperature is assumed to be limited, the amount of glass to form a pore-free composite with SiC powder can be calculated by knowing the density of the glass and the green density of a pressed SiC compact. The amount of infiltration of the glass into a porous composite preform and the degree of wetting to the SiC substrate are also of interest in trying to form as thin a brittle interfacial layer as possible. Placing the eutectic glass in contact with the SiC substrate and a porous composite preform should allow infiltration and/or reaction to proceed yielding a pore-free composite with a very thin interfacial substrate layer.

2.3.2.2 Experimental procedure

a. Glass preparation

Stoichiometric mixtures of $CaCO_3$[i], Al_2O_3[ii], and SiO_2[iii] were mixed in isopropanol with 2 weight percent dispersant[iv] to obtain the 1170 and 1265°C eutectic compositions. Since $CaCO_3$ decomposes in air via the reaction

$$CaCO_3 \rightarrow CaO + CO_2\,(g)$$

the amount of weight loss occurring was first determined. In addition, the very high surface area of the amorphous silica powder necessitated drying to drive off adsorbed

[i] Aldrich Chemical Company; Milwaukee, WI

[ii] 0.32 μm, 6 m^2/g, Sumitomo Chemical America; New York, NY

[iii] 400 m^2/g amorphous fumed, Alpha Aesar; Ward Hill, MA

[iv] BRIJ-35. Aldrich Chemical Company; Milwaukee, WI

water. The powders were attritor milled with zirconia balls for 1 hour, stir dried, and melted in a platinum crucible in air at 1500°C for 4 hours. The molten glass was immediately quenched into a deionized water bath. The resulting solid pieces were crushed, attritor milled in isopropanol with 4 weight percent binder[i] for 4 hours, stir dried, then sieved through a 100 mesh screen. Some of the glass was mixed with SiC powder[ii] in order to obtain composite powders of the desired compositions.

b. Composite preform and joint preparation

Composite powders of 5, 10, 15, and 20 weight percent glass were prepared following the above procedure, and uniaxially pressed at 4000 psi into compacts which were then subjected to a variety of processes, which are summarized in Table 2-3. In addition, prototype joints were prepared by placing the porous composite preforms, containing 15 weight percent glass processed in an inert atmosphere, in contact with a porous (75-80 % dense) SiC substrate and an excess supply of the pure glass (see Figure 2-5). Reaction/infiltration was allowed to occur in air at 1200-1300°C.

2.3.2.3 Results and discussion

Table 2-3 gives a qualitative summary of the experiments conducted. Several observations were made during the experiments:

[i] Tertiary amide polymer, Dow Chemical Company; Midland, MI

[ii] 0.15 mm, H.C. Starck Co.; Berlin, Germany

- No densification in the CAS/SiC system was observed, implying that no diffusion of Si or C through the liquid phase occurred. To form a pore-free composite a larger amount of glass (31.5 wt. %) would be required.
- Processing in air significantly accelerated reaction kinetics and bonding.
- The glass wets the SiC particles well enough to prevent it from flowing out of the sides of the compact, but the hardness of the compact was not continuous throughout. Only the material near the surface was well bonded.
- Oxidation at 1300°C of the composites led to a differential stress gradient from the surface leading to radial cracking. The condition was more pronounced for the lower melting point composition, where the weight gain due to oxidation ranged from 11.5% for the 20 wt.% in SiC composite to 15.2% for the 5 wt.% in SiC composite. It is probable that the higher melting point composition formed a liquid with lower O_2 permeability as no weight gain was observed in the composite sample fired at 1300°C. For high temperature service, processing in air for sufficient times to achieve a thermodynamically stable state would be required.

Table 2-3 Summary of CAS/SiC composite experiments

Composition	*Processed in air (°C)*	*Processed in argon (°C)*	*Pressed at (MPa)*	*Densified?*	*Bonded?*	*After oxidation*[i]
5% 1170	1200		28	N	N	n/a
5% 1170		1200	28	N	N	n/a
10% 1170	1200		28	N	N, cracked	n/a
10% 1170		1200	28	N	N	n/a
15% 1170	1200		28	N	N	n/a
20% 1170	1200		28	N	80%	n/a
20% 1170		1200	28	N	N	radial crack
5% 1265		1250	1240 (cip)	N	N	n/a
10% 1265	1250		1240	N	N	n/a
10% 1265		1250	1240	N	N	no effect
15% 1265	1250		28	N	N	n/a
15% 1265		1250	1240	N	N	n/a
20% 1265	1300		28	N	N, cracked	n/a
20% 1265		1250	1240	N	N	n/a

The sequence of x-ray diffraction spectra seen in Figure 2-6 illustrates the development of crystalline phases occurring in the 1170° eutectic composites. In a) the sample fired in air at 1200°C , an amorphous region appears in the sample when the scan is run on the surface; however, when sectioned in the center, this region is smaller. Comparison of the relative peak heights of the (101) α-cristobalite at 4.5 Å and the (111) SiC peak at 2.52 Å indicates that crystallization of SiO_2 is also favored near the surface. One possibility is that the silica rich liquid tends to migrate towards the surface in an

[i] 3 hours at 1300°C

oxygen rich environment. A more likely scenario is that the crystalline silica oxidation zone near the surface formed a barrier for O_2 permeation and that longer dwell times would be required for complete reaction to occur. In b) the sample fired in air at 1350°C, several secondary cristobalite peaks appear. Finally, in c) the sample fired in air at 1500°C, cristobalite and pseudowollastonite, a calcium silicate, are seen.

The process described in Figure 2-5 is a representation of the formation of a skeletal framework of SiC particles completely wetted with CAS glass, with a thin wetting layer adhering to the substrate. Figures 2-7 and 2-8 are low magnification (50X) optical micrographs of the reaction infiltration process in prototype samples made with a porous composite (15 wt. % glass) bonded to a porous SiC substrate (75-80 % dense) with excess glass. It was desired that the low density simulate a best case scenario for infiltration in which the substrate has high surface porosity. In the 1265° eutectic material, reaction and/or infiltration is evident around the periphery of the preform, but sufficient capillary force is not present along the interface to form a continuous bond, and good contact is not maintained after cooling due to warping. In the 1170° eutectic material, better contact is maintained, as less infiltration around the periphery is observed, but infiltration into the composite preform did not proceed to completion, a thick layer of glass remained at the interface, and thermal stresses during cooling led to cracking in the preform.

One possible explanation for these effects is that the 1265° composite preform has higher surface porosity. With the assumption that the porosities are comparable, however, it is more probable that the lower viscosity (lower SiO_2 content) liquid formed with the

1265° composition wicked up the sides of the pore walls better than the higher viscosity 1170° composition, thus the excess glass was taken up into the peripheral surface areas more efficiently. Therefore warpage and loss of contact upon cooling was more severe. At the same time surface oxidation in the 1170° material may have sealed off the center of the compact from oxygen, inhibiting reaction and capillary action around the periphery. Further work would be needed to tailor the pore size/distribution, glass viscosity, and heating schedule for optimizing infiltration and reducing thermal stresses.

2.3.3 Ion exchange mechanism to form Calcium Hexaluminate

2.3.3.1 Background

Calcium hexaluminate, $CaO{\cdot}6Al_2O_3$ (CA_6), is a refractory cement known to be resistant against slag corrosion. The material is also very stable, with raw materials that are inexpensive and easy to work with. Referring to the CaO-Al_2O_3 phase diagram in Figure 2-9, compositions exceeding C/A ratios of 1:1 should be useful at temperatures exceeding 1600°C, and CA_6 has a melting point of 1830°C. However, the sintering temperatures for producing these compounds are too high for processing SiC_f/SiC CMC's or for joining to most metals. DeJonghe *et al.* demonstrated that a complex reaction zone leading to the formation of CA_6 occurs when compositions near the 1360°C eutectic are melted in contact with polycrystalline alumina at 1530°C.[11] Since CA_6 was found to be the most stable compound the CaO-Al_2O_3 system[12] it may be possible to form it in the eutectic liquid phase by diffusing in enough excess Al_2O_3 to exchange with highly mobile Ca^{2+} ions. A similar methodology was employed by DeJonghe and Goo[13] to reduce the

sintering temperature of β-alumina below 1600°C. The thermal expansion mismatch with SiC could be alleviated by dispersing SiC powder in the interlayer material. This would also serve to increase the fracture toughness of the joint.

2.3.3.2 Experimental procedure

$CaCO_3$[i] and Al_2O_3[ii] were mixed at the 1360°C eutectic composition and homogenized in air at 1420°C for 1 hour. After slow cooling at 10°C/minute the powders were attritor milled in isopropanol for 4 hours, and sieved to -325 mesh (45 μm) particle size. Compacts were made with 35 vol. % glass (theoretical pore free mixture) in SiC by procedures given in section 2.3.2, and x-ray diffraction analysis performed.

The homogenized eutectic was mixed with a coarse grain alumina powder[iii] in proportion to form stoichiometric calcium hexaluminate. The coarse grain was chosen to slow the reaction kinetics, enabling the formation of alumina rich phases in the lower melting eutectic liquid by an ion exchange mechanism. Pellets were pressed at 28 MPa with a binder and heated in air at 1500°C for 4 hours. The resulting material was examined in the x-ray diffractometer.

A thick layer (≈ 0.2 mm) of the homogenized eutectic powder was deposited on a fine polished SiC substrate and fired in air at 1400°C to examine wetting and film stability. Prototype joints were made with sandwich geometry and examined using scanning electron microscopy.

---

[i] Aldrich Chemical Company; Milwaukee, WI

[ii] 0.18 μm, 10 m^2/g, Sumitomo Chemical Americal; New York, NY

[iii] 6-10 μm, Alcoa Aluminum Company of America; Bauxite, AR

2.3.3.3 Results and discussion

X-ray diffraction of the homogenized powder (see Figure 2-10a) reveals the presence of $12CaO \cdot 7Al_2O_3$ ($C_{12}A_7$) along with a glassy phase. The x-ray spectrum of the $SiC/C_{12}A_7$ composite (Figure 2-10b) shows evidence of the crystallization of anorthite ($CaO \cdot Al_2O_3 \cdot 2SiO_2$) and the complete absence of $C_{12}A_7$.

In the x-ray spectrum shown in Figure 2-10c, taken on the powder obtained from the $C_{12}A_7$/excess Al_2O_3 powder compact, CA_6 dominates, with smaller corundum peaks also noted. It is also interesting to note that no other calcium aluminate phase is observed, indicating a complete reaction sequence taking place from $C_{12}A_7 \rightarrow CA \rightarrow CA_2 \rightarrow CA_6$. The compact was not sintered, however, and broke up into large needle-shaped crystals. Formation of a dense CA_6 without hot-pressing would require a higher liquid phase content to allow diffusion across the distances required for densification. This apparently can only be achieved at higher temperatures.

Referring to Figure 2-11, it is clear that the oxide film is highly unstable when fired on a SiC substrate in air. The prominent foaming can be attributed either to aggressive reaction or oxidation of the SiC substrate, or both. Similarly, the SEM micrograph of the joint interface (Figure 2-12) reveals a porous reaction byproduct with a different level of contrast than either the SiC or the calcium aluminate. The chemically incompatible interface is again observed in the SEM micrograph of the joint (Figure 2-13), which cracked along the interface either due to thermal stresses, or the polishing process.

2.3.4 Oxide frit braze with Cordierite

2.3.4.1 Background

Crystallizable glasses of the lead borosilicate system have been demonstrated as effective in producing hermetic seals in the microelectronics industry.[14] These materials can be fired at low temperatures and partially crystallize upon slow cooling to match the thermal expansion coefficient (CTE) of the alumina packages being sealed. The seals then exhibit good high temperature mechanical properties (primarily creep resistance) due to the crystalline microstructure, allowing for subsequent thermal processing. Minor additions of network modifier ions to a crystallizable glass (glass-ceramic) can dramatically lower its melting point and viscosity without significantly altering the crystallization path. Also, processing in the glassy state allows for thorough wetting to fill in gaps and pores in the substrate. A glass-ceramic of the lithium aluminosilicate system has been successfully used in this way to form high strength hermetic seals on a nickel-based superalloy (Inconel 718) in the manufacture of high pressure electrical connectors.[15] In this application the molten glass is allowed to flow into the metal housing and react to form a strong bond. A controlled crystallization heat treatment is added to yield a complex microstructure with a matching bulk thermal expansion coefficient.

The ceramic cordierite ($2MgO \cdot 2Al_2O_3 \cdot 5SiO_2$) has physical properties that make it a logical choice for joining SiC. It has the highest elastic modulus of any glass-ceramic material (232 GPa), relatively high strength (290 MPa) and low thermal expansion coefficient (2.5×10^{-6}/°C from 0-1000°C). In addition, the glass can be doped with minor additions of alkali earth oxides or fluoride ion in order to lower its melting point or change its wetting characteristics. In theory, the glass should remain amorphous and wet the SiC

substrate to form a strong bond when rapidly fired. Controlling the degree of crystallinity during a subsequent heat treatment should tailor the mismatch in thermal expansion coefficient and elastic moduli to improve the mechanical integrity of the joint. Finally, brazing with an oxide should provide for intrinsically greater environmental stability for high temperature service.

2.3.4.2 Experimental procedure

a. Processing atmosphere

The glass-ceramic powder (EG-0221), obtained from Ferro Corp. in Cleveland, Ohio, is used in the manufacture of substrates in microelectronic packages. The 4.9 μm powder contains 52.5% SiO2, 32.0% Al_2O_3, 13.5% MgO, and 2.0% BaO by weight. The powders were suspended in Methyl Ethyl Ketone with a binder[i] and dispersant[ii] and layers deposited by dip coating on fine polished (6 μm) SiC substrates that were surface ground flat. After burning off the binder in air at 400°C the parts were fired in air and argon at 10°C/minute to 1500°C and examined in the SEM in order to assess the sensitivity of wetting to processing atmosphere. Sandwich joint specimens were made using various coating combinations to produce different thickness. The parts were thin sectioned and the opposing fracture surfaces examined. X-ray diffraction was also performed on the exposed fracture surface.

[i] XUS40303.00 tertiary amide polymer, Dow Chemical Co.; Midland, MI

[ii] Menhaden fish oil, Sigma Chemical Co.; St. Louis, MO

b. Interfacial strength assessment

Joints of thickness ranging from 15 to 37 μm were studied by forming an indentation crack near the interface. Using a 10 kg load and a pyramidal shaped diamond indenter, the incidence angle of the crack was varied so that the interfacial adhesion and joint integrity could be qualitatively assessed.

2.3.4.3 Results and discussion

Processing in vacuum is required in order to produce a stable film and reduce bubble formation at the interface. An air atmosphere leads to vigorous reaction and a highly disrupted film. Processing in argon produces a continuous, stable coating, but fracture surfaces reveal the presence of large unwet areas due to bubbles. The fracture surface of the joint processed in vacuum shows the absence of voids due to bubbling (see Figure 2-14). X-ray diffraction of the fractured surface (Figure 2-15) shows the presence of the high intensity ($100_{\alpha}/110_{\beta}$) cordierite peak, and little or no amorphous phase (it was impossible to distinguish the α from the β phase at the step scan of .05 degrees employed). The crystallization was highly textured, as determined from the lack of secondary peaks in the proper proportion to the main peak.

The indentation crack path studies (Figure 2-16) reveal the presence of a strong bond at the interface, as none of the low angle impinging cracks preferred the interface over the bulk. Due to the similarity in density and contrast in the SEM between the bulk material and the reaction zone adjacent to the interface, the presence of a chemically compatible reaction phase can be inferred.

2.3.5 Conclusions

Oxide frit brazing with a cordierite glass-ceramic is the most promising of the four methods investigated. A stable film is obtained when fired in vacuum, and a strongly adhered, chemically compatible interface forms as demonstrated by SEM and during analysis of indentation crack paths. In contrast, the reaction bonding process attempted with Al/Si-Si-C does not form an intimate contact interface and a joint is not formed. The reaction/infiltration process with calcium aluminosilicate glass does not succeed because of insufficient capillary forces, either due to oxidation sealing off pores or inadequate control of viscosity and pore size. The material also displays cracking due to residual thermal stresses present after cooling. The ion exchange mechanism proposed for the formation of calcium hexaluminate in a low temperature eutectic liquid fails to provide for the short diffusion distances required for densification into a hard body, and the interfacial reaction product formed (probably anorthite) is not strongly adhered to the SiC substrate.

2.4 References

1. M. Ferraris, C. Badini, M. Montorsi, P. Appendino, and H. W. Scholz, "Joining of SiC_f/SiC Composites for thermonuclear fusion reactors," *J. Nuclear Materials*, **212-215** 1613-16 (1994).
2. D. Stinton, A. Caputo, and R. Lowden, "Synthesis of fiber-reinforced SiC composites by chemical vapor infiltration," *Am. Ceram. Soc. Bull.* **65** [2] 347-50 (1986).
3. B. Rabin, "Joining of fiber-reinforced SiC composites by *in situ* reaction methods," *Mat. Sci. Eng.*, **A130** L1-L5 (1990).
4. A. Glaeser, M. Shalz, B. Dalgleish, and A. Tomsia, "New Approaches to Joining Ceramics for High-Temperature Applications," *Ceramic Transactions*, **35** 301-22 (1993).
5. W. Zdaniewski, P. Shah, and H. Kirchner, "Crystallization Toughening of Ceramic Adhesives for Joining Alumina," in *Advanced Ceramic Materials*, **2** [3A] 204-08 (1987).
6. D. Coon, "Vitreous joining of SiC fiber reinforced SiC composites," DOE Technical Report NTIS DE90-01295 (1989).
7. M. Schwartz, in Ceramic Joining, ASM International, Materials Park, Ohio, (1990), 19-37.
8. H. Tanaka, "Sintering of silicon carbide," in Silicon Carbide Ceramics--1, edited by S. Somiya and Y. Inomata, Elsevier Applied Science, New York NY, (1991) 213-238.

9. J. Cao, "In Situ Toughened SiC Ceramics with Al-B-C Additions and Oxide-Coated SiC Platelet/SiC Composites," Ph.D. Thesis, University of California at Berkeley, (1996).

10. B. Rabin, "Modified Tape Casting Method for Ceramic Joining: Application to Joining of Silicon Carbide," *J. Am. Ceram. Soc.*, **73** [9] 2757-59 (1990).

11. L. DeJonghe, H. Schmid, and M. Chang, "Interreaction Between Al_2O_3 and a CaO-Al_2O_3 Melt," *J. Am. Ceram. Soc.*, **67** [1] 27-30 (1983).

12. M. Allibert, C. Chatillon, and C. Jacob, "Mass-Spectrometric and Electrochemical Studies of Thermodynamic Properties of Liquid and Solid Phases in the System CaO-Al_2O_3," *J. Am. Ceram. Soc.*, **64** [5] 307-14 (1981).

13. L. DeJonghe and E. Goo, "Transient Eutectics in Sintering of Sodium Beta Alumina," in *Processing of Crystalline Ceramics*, ed. by H. Palmour, R. Davis, and T. Hare, Plenum Publishing Co, New York (1978) 433-41.

14. R. Buchanan, in *Ceramic Materials for Electronics: Processing, Properties and Applications*, Marcel Dekker, Inc., New York, p. 20 (1986).

15. H. McCollister and S. Reed, U.S. Patent No. 4,414,282 (1983).

Chapter 3 Theory

3.1 Introduction

The mechanism of bond formation with a cordierite glass-ceramic involves 1) reactive wetting to the substrate to form an evenly distributed well adhering interface; and 2) controlled crystallization of the interlayer to improve thermomechanical properties. These topics will be discussed in some detail along with the crystallography of cordierite.

3.2 Wetting and adhesion

3.2.1 Chemical equilibrium conditions

The phenomenon of wetting can be described by the thermodynamic equilibrium between the solid, liquid, and vapor phases present in a system. Under conditions of chemical equilibrium, the contact angle of the liquid on the solid is determined solely by the mechanical forces present due to the solid-liquid interfacial energy (γ_{sl}), the solid-vapor interfacial energy (γ_{sv}), and the liquid surface tension (γ_{lv}). This relation is in part expressed by the well known Young equation (Figure 3-1):

$$\gamma_{lv} \cos \theta = \gamma_{sv} - \gamma_{sl} \qquad (3\text{-}1)$$

with the assumptions that the interfacial energies are the instantaneous values present at the time the contact angle is measured, and the mass of the liquid droplet is small enough to neglect the force of gravity. In an ideal system where no chemical reaction occurs the free energy changes in the system are associated only with changes in the interfacial areas, and the only source of adhesion is Van der Waals bonding.[1,2] The contact angle and the liquid-vapor surface tension can be readily determined; the values of γ_{sv} and γ_{sl} are

deduced for the particular system being studied. Situations where $\theta < 90°$ constitute wetting; where $\theta > 90°$, dewetting (see Figure 3-1).

The attraction between the solid and liquid phase can be expressed in terms of the work of adhesion,

$$W_{ad} = \gamma_{sv} + \gamma_{lv} - \gamma_{sl} \qquad (3\text{-}2)$$

which is the free energy change upon reversible formation of an interface from two independent surfaces.[3] Combining equations (2-1) and (2-2) gives the relation

$$W_{ad} = \gamma_{lv} (1 + \cos \theta) \qquad (3\text{-}3)$$

which is an expression relating the interface strength to two readily obtainable parameters. Another often utilized parameter that describes the driving force for a new liquid/solid interface to form is the spreading coefficient

$$S = \gamma_{sv} - \gamma_{lv} - \gamma_{sl} . \qquad (3\text{-}4)$$

It is clear that if the solid/vapor interfacial free energy is greater than the sum of the solid/liquid and liquid/vapor free energies the system can lower its total surface energy by forming an interface with the liquid, and spreading occurs. Thus, the most obvious methods for increasing the degree of wetting are increasing the value of γ_{sv} and decreasing the value of γ_{lv}. These are most easily accomplished by cleaning the substrate surface and by adding minor alloying elements to the liquid, decreasing its surface tension.

3.2.2 Chemical nonequilibrium conditions

The above equations are based on conditions of chemical equilibrium and neglect the effect of mass transport at the interface from diffusion and chemical reaction. The

extent of the interaction between the solid and liquid phases can be seen (in order of increasing interaction) as adsorption, inter-diffusion, saturation or alloy formation, and compound formation. As the interaction proceeds a dynamic situation exists whereby the composition of the solid and liquid adjacent to the interface is changing. Then there is a contribution to the reduction of the solid surface free energy by an amount equal to the free energy of the reaction per unit area as a function of time (dG_R). In this scenario the *dynamic* driving force for wetting can be expressed as (the primes indicate transient quantities)[2]

$$\sigma' = \gamma_{sv} - (\gamma'_{sl} + dG_R). \qquad (3\text{-}5)$$

Provided the flow rate of the liquid is fast enough (relative to the diffusion of reacting species) for it to remain in intimate contact with unreacted solid, the contact angle will decrease and spreading will occur when this driving force exceeds γ_{lv} in equation (3-4). As one or more of these interactions proceed the system may initially display aggressive spreading behavior as the contribution made by dG_R dominates, and γ_{sl} and γ_{lv} decrease rapidly. As the system evolves to steady state, however, γ_{sl} and γ_{lv} increase to the static interfacial tension values, with the value of γ_{sl} tending towards the lower of γ_{lv} and γ_{sv}. Neglecting complex effects, such as capillary induced ridging, the equilibrium contact angle maintained by the system is determined by the wetting characteristics of the remaining liquid on the existing top layer solid phase.

3.3 Crystallization of glass-ceramics

3.3.1 Introduction

Glass-ceramics are polycrystalline solids prepared by the controlled crystallization of glasses. The phase(s) formed are crystallized entirely from a homogeneous glass phase which distinguishes these materials from traditional ceramics.[4] These materials have found applications in electronics, as bioactive materials, as specialty optical materials, and in severe thermal mechanical environments as matrices for fiber reinforced composites.[5]

3.3.2 Glass formation

Upon cooling a melt to induce a phase transformation, the driving force for formation of the stable phase can be expressed as the difference between the bulk free energies of the liquid and solid phases per unit volume,

$$\Delta G_v = G^{\beta} - G^{\alpha} = \Delta E_v - T\Delta S_v. \tag{3-6}$$

Since at the equilibrium transformation temperature T_E, $\Delta G_v = 0$,

$$\Delta S_v = \frac{\Delta E_v}{T_E} \tag{3-7}$$

If the transformation occurs with some degree of undercooling, the thermodynamic driving force can be expressed as

$$\Delta G_v = \frac{\Delta E_v \Delta T}{T_E}. \tag{3-8}$$

In fact, the mechanism of phase transformation is not so simple; there is a free energy barrier to the formation of small β particles even at high values of undercooling due to the inability of atoms to instantaneously align themselves into the β structure. If the degree of undercooling (or supercooling) is sufficiently large, kinetic factors dominate and a

metastable state can result in which no long range crystalline order forms, and the material becomes amorphous.

3.3.3 Nucleation

In classic homogeneous nucleation theory, two opposing factors govern the free energy change: an increase in surface free energy by the formation of a new surface, and a decrease of the bulk free energy by the reduction in entropy associated with forming the new phase. Assuming the nucleus to be spherical in shape,

$$\Delta G_{tot} = \frac{4}{3}\pi r^3 \Delta G_v + 4\pi r^2 \gamma. \qquad (3\text{-}9)$$

The critical nuclear size r* corresponding to the maximum free energy change is found from the condition $(\delta \Delta G_r/\delta r) = 0$, so that

$$r^* = -\frac{2\gamma}{\Delta G_v}. \qquad (3\text{-}10)$$

Thus the activation energy barrier to homogenous nucleation can be expressed as

$$\Delta G^* = \frac{16\pi\gamma^3}{3\Delta G_v^2}. \qquad (3\text{-}11)$$

The actual nucleation rate also depends strongly on kinetic factors, i.e. not only on the number of nuclei with sufficient energy to be stable, but also on the ability of atoms to diffuse to the potentially stable nucleus,[6] or

$$\dot{N} = A \exp -\left[\frac{\Delta G^* + \Delta E_D}{kT}\right] \qquad (3\text{-}12)$$

In a glass-forming liquid, sufficient undercooling will suppress homogeneous nucleation entirely as the activation energy for diffusion ΔE_D, is so high that atom mobility across a potential phase boundary is essentially zero.

Since the activation energy for nucleus formation is proportional to γ^3 (see Eq. 3-11), a small decrease in surface energy can increase the nucleation rate dramatically. This increase can be defined in terms of the reduction in the atomic volume required to reach the critical radius size for nucleation, and is a function of the contact angle of the newly forming phase on a heterogeneous nucleation site. Thus,

$$\Delta G^*_{HET} = \Delta G^*_{HOM} f(\theta) \tag{3-13}$$

with the catalytic factor $f(\theta)$ given by (for a spherical cap nuclei)[4,7]

$$f(\theta) = \frac{(2+\cos\theta)}{4}(1-\cos\theta)^2. \tag{3-14}$$

In silicate melts, the rate of heterogeneous nucleation is also very small because complex silicates are required to provide the catalytic action and they are readily redissolved into the melt. In glass-ceramic systems, however, liquid/liquid phase separations can produce precursor phases which are similar in structure to that of the phase being nucleated. If the disregistry on low index planes is not more than 15 percent, epitaxial growth of the crystallizing species can occur on the precursor crystallite facets.[4] Such effects were demonstrated in a lithium aluminum silicate glass doped with P_2O_5, in which cristobalite, lithium metasilicate, and lithium disilicate precipitated by epitaxial growth on Li_3PO_4 crystallites.[8] In the magnesium aluminum silicate system doped with TiO_2, the mechanism of cordierite nucleation on Mg titanates was first demonstrated by Maurer *et al.* in 1962.[9]

In glass-ceramic materials doped with minor additions of modifier cations, such as Ba^{2+}, competition for oxygen ions with network formers such as Si^{4+} and Al^{3+} causes local regions of ordering where the system can do work to lower its free energy by separating into two liquid phases. At high temperatures, the low cationic field strength of the modifier is inadequate for bonding to non-bridging oxygens leaving the glass homogeneous. At lower temperatures, however, the field strength becomes sufficient to disrupt the random structure of the melt and form regions of higher coordination.[10] These regions typically form as emulsions and can serve as precursors for the crystallization of phases which closely resemble in structure the desired final crystalline product. Since the emulsion phase is finely dispersed, catalyzed nucleation followed by controlled crystallization can lead to a very fine-grained pore-free ceramic microstructure.

3.3.4 Crystal growth and properties

The objective of the heat treatment process is to convert the glass into a microcrystalline ceramic with the desired properties. In the magnesium aluminum silicate system (see Figure 3-3), mullite, tridymite, and protoenstatite are the secondary phases forming during equilibrium cooling from a stoichiometric cordierite composition. Control of the relative amounts of these phases, or any other phases which may form in practice, with respect to cordierite, is paramount in producing the desired microstructure and thermomechanical properties.

During heating of the two phase glassy emulsion, submicron crystallites will form, followed by nucleation and growth of crystals on planes of low interfacial energy. Slow heating is essential in order to avoid deformation of the glass-ceramic and maintain a rigid

skeletal network. It also enables enough viscous flow within the residual glass to relieve residual stresses accompanying volume changes upon crystallization. As crystallization proceeds, any species not easily substituting on the crystal lattice is rejected into the glassy reservoir. In the case of a BaO nucleated glass-ceramic, this could tend to increase the refractoriness of the residual glass.

Assuming that crystallization proceeds from a fixed number of nuclei, the process of crystal growth is described by the Johnson-Mehl-Avrami equation[11,12]

$$-\ln(1-\alpha) = (kt)^n \qquad (3\text{-}15)$$

where α is the volume fraction of crystallized phase at time t, and n is a parameter related to the mechanism of the process (n=1, surface crystallization; n=3, bulk crystallization). The constant k is related to the absolute temperature T by an Arrhenius type equation

$$k = AN\exp(-E_c/RT) \qquad (3\text{-}16)$$

where E_c is the activation energy for the crystal's growth, N is the number of nuclei, and A is a constant.

The residual strain upon cooling associated with the formation of a sandwich joint is a function of the thermal expansion and elastic moduli mismatches;

$$\varepsilon = \frac{E_i E_j(\alpha_i - \alpha_j)(\Delta T)}{E_i + E_j}. \qquad (3\text{-}17)$$

The thermal expansion of a multi-phase glass ceramic material can be approximated using the following expression, originally obtained by Turner:[13]

$$\alpha = \frac{\sum \alpha_i B_i W_i/\rho_i}{\sum B_i W_i/\rho_i} \qquad (3\text{-}18)$$

where α_i is the thermal expansion coefficient, B the bulk modulus, W the weight fraction, and ρ the density of the individual phases. In the case of crystalline phases embedded in a matrix of residual glass phase of higher CTE, compressive hoop stresses and tensile radial stresses can develop around the interfaces which serve to toughen the composite.[14] In joints, if the thermal expansion of the interlayer exceeds that of the base material, residual tensile stresses develop upon cooling which can weaken the joint in uniaxial tension. Conversely, if the interlayer has a lower expansion than the substrate, the joint will be left in compression, which would tend to strengthen the joint. These effects are alleviated at elevated temperature. Finally, reducing the layer thickness can increase the strength of the interlayer material to approach its theoretical value by making it more improbable that a flaw exists for brittle failure initiation, while also reducing the tendency for interface crack propagation caused by the elastic moduli mismatch by constraining the volume of stress relief

3.4 Crystallography

Cordierite, $2MgO \cdot 2Al_2O_3 \cdot 5SiO_2$, exists in two stable forms: an orthorhombic form β (low cordierite), which is stable below 1450°C, and a hexagonal form α (high cordierite), stable between 1450°C and its melting point, 1460°C. A metastable low temperature form μ has also been identified as a stuffed β-quartz derivative. The structure of high cordierite, depicted in Figure 3-2, consists of six-membered hexagonal rings of linked $(Si,Al)O_4$ tetrahedra joined above and below by sharing two of the four oxygen atoms in each tetrahedron to form a column of rings enclosing a large empty channel.

These columns are joined laterally in hexagonal array by Al ions in tetrahedral and Mg ions in octahedral coordination. The α and β phases differ only in the degree of ordering of Al and Si in the available ring sites; in the perfectly hexagonal form the distribution is entirely random. Perfect alternation of the Al and Si ions causes the slight distortion of the structure into the orthorhombic, or pseudohexagonal form, β. Although the β phase is thermodynamically stable at room temperature, its transformation from the disordered α phase is very sluggish, and is usually not observed in synthetic materials.[15-18]

Hexagonal cordierite has lattice parameters of 9.365 and 9.782 Å along the c- and a-axes, respectively. The great difference in lattice parameter and structure from SiC makes alloying impossible at any temperature. Furthermore, the processing temperatures of interest (below 1500°C) make solubility in SiC of any constituent of the cordierite glass melt unlikely. Therefore, it is certain that the formation of a strong bond would be predicated on the ability of a thin silicate reaction product or oxycarbide glassy phase to form at the interface which is chemically compatible with both SiC and cordierite.

3.5 References

1. I. Aksay, C. Hoge, and J. Pask, "Wetting under Chemical Equilibrium and Nonequilibrium Conditions," *J. Phys. Chem.* **78** [12] 1178-83 (1974).
2. J. Pask and A. Tomsia, "Wetting, Spreading and Reactions at Liquid/Solid Interfaces," in *Surfaces and Interfaces in Ceramic and Ceramic-Metal Systems*, ed. by J. Pask and A. Evans, Plenum Press, New York (1981) pp. 411-19.
3. R. Cannon, E. Saiz, and A. Tomsia, "Reactive Wetting Taxonomy," *Mat. Res. Soc. Symp* **357** pp. 279-92 (1995).
4. P. McMillan, "*Glass-Ceramics*," Academic Press, New York, 1964, chapters 1 and 2.
5. G. Beall, "Glass-Ceramics: Recent Developments and Applications," in *Nucleation and Crystallization in Liquids and Glasses*, ed. M. Weinberg, American Ceramic Society, Westerville, OH (1993) 241-66.
6. C. Barrett, W. Nix, and A. Tetelman, in *The Principles of Engineering Materials*, Prentice Hall, New Jersey (1973) chapter 5.
7. M. Ashby and D. Jones, in *Engineering Materials 2, an Introduction to Microstructure, Processing, and Design*, Pergamon Press, Oxford, (1986), chapter 7.
8. T. Headley and R. Loehman, "Crystallization of a Glass-Ceramic by Epitaxial Growth," *J. Am. Ceram. Soc.*, **67** [9] 620-25 (1984).
9. R. Maurer, *J. Appl. Phys.* **33**, 2132-39 (1962).
10. Z. Strnad, in *Glass-Ceramic Materials*, Elsevier Science Publishing Co, Inc., New York, (1986), chapter 2.

11. W. Johnson and R. Mehl, "Reaction Kinetics in Processes of Nucleation and Growth," *Trans. AIME*, **135** 416-42 (1939).

12. M. Avrami, "Kinetics of Phase Change," *J. Chem. Phys.*, 7 1103-12 (1939).

13. W. Kingery, H. Bowen, and D. Uhlmann, in *Introduction to Ceramics*, 2nd ed., John Wiley and Sons, New York, (1976), p. 604.

14. A. Evans and T. Langdon, "Structural Ceramics," *Prog. Mater. Sci.*, **21** [3-4] 171-441 (1976); p. 196.

15. G. Gibbs, "The polymorphism of cordierite I: the crystal structure of low cordierite," *Am. Mineral.*, **51** (1966) 1068-87.

16. J. Cohen, F. Ross, and G. Gibbs, "An X-ray and neutron diffraction study of hydrous low cordierite," *Am. Mineral.*, **62** (1977) 67-78.

17. E. Meagher and G. Gibbs, "The polymorphism of cordierite II: the crystal structure of indialite," *Can. Mineral.* **15** (1977) 43-9.

18. W. Deer, R. Howie, and J. Zussmann, in *Rock-Forming Minerals, Vol. 1, Ortho- and Ring Silicates*, John Wiley and Sons, New York (1962) 256-99.

Chapter 4 Experimental Procedures

4.1 Introduction

The firing schedule utilized for bonding with cordierite glass-ceramics is shown schematically in Figure 4-1. The initial ramp rate to melt the glass must be sufficiently high to prevent crystallization of cordierite and/or effect a liquid phase separation, which could affect wetting as well as the flow characteristics of the melt. The time at peak temperature must also be optimized to achieve the lowest contact angle possible while preventing the formation of bubbles at the interface. The rate of cooling from the melt must be as rapid as possible to limit crystallization of large cordierite grains nucleating at the interface. The temperature of the nucleation dwell is determined by the glass transition temperature, and the time necessary to maximize phase separation and dispersion must be determined experimentally. The time and temperature of the crystallization heat treatment can be determined by the resultant grain size and phase distribution.

The materials used in this study were a commercial SiC[i], and a commercial cordierite glass powder[ii], with the following characteristics. The processing atmosphere, as shown earlier, was vacuum.

[i] Hexoloy SA, Carborundum Co.; Niagara Falls, NY

[ii] EG-0221, Ferro Corp.; Cleveland, OH

Table 4-1 Elemental Analysis of SiC

Constituent	Weight percent
SiC	> 97.5
Free C	< 1.1
B	0.4-0.8
Free Si	< 0.18
Al	< 0.16
Fe	< 0.13
Na, Ca (each)	< 0.05
Mg, Ti (each)	< 0.02
Co, Mo, Cr, Ni, Cu, V, Mn, Zr (total)	0.01

Table 4-2 Elemental Analysis of Cordierite

Component	Weight Percent
SiO_2	52.5
Al_2O_3	32.0
MgO	13.5
BaO	2.0

4.2 Contact angle

The effects of substrate precondition, substrate surface finish, glass liquid surface tension, and quench rate were evaluated using sessile drop experiments, in a graphite element furnace,[i] in vacuum. The evolution of wetting was observed through the front viewport on the furnace. Four substrate preconditions were tested: 1) no preconditioning; 2) preoxidized in air at 1400°C for 20 hours (< 0.5 μm thick oxide); 3) glazed with kaolin in air at 1300°C; and 4) ion implanted with titanium, 150 Kev accelerator voltage, 10^{17} cm^{-2} flux (courtesy Dr. I. Brown). Two surface finishes were evaluated: 1) as-ground; and 2) 1μm fine polish. Three glass compositions were used: 1) as received; 2) doped with 1.0 weight % CaF_2; and 3) doped with 2.2% BaF_2. In addition, the effect of ramp rate and quench rate were assessed in terms of the adhesion of the sessile drop and the homogeneity of the quenched glass. The quench rate was varied by quenching in vacuum, argon, and helium gas.

The glass pieces used were prepared by traditional glass forming and homogenization techniques in a platinum crucible. The glass powders were fired in air at 1500°C for 2 hours and then quenched into deionized water. Bubble free chunks were chosen and ground flat for the experiments. Substrates were thoroughly cleaned in an acetone/isopropanol ultrasonic bath, followed by a final methanol rinse. Sessile drop samples were cross-sectioned and viewed optically for contact angle measurements, interfacial dewetting, and extent of phase separation and/or crystallization. The contact

[i] HTG-7010G, Thermal Technologies; Santa Rosa, CA

angle was determined using the formula $\theta = 2 \arctan (2H/d)$[1], where H and d are the height and diameter of the sessile droplet, respectively.

Interface characterization was performed using thin film x-ray diffraction[i] and transmission electron microscopy[ii] (courtesy Dr. W. MoberlyChan).

4.3 Tape casting

Films of varying thickness were applied using conventional tape casting techniques. To limit the amount of organic material introduced (i.e. plasticizer), and subsequent handling during a tape transfer operation, films were applied directly to the polished SiC substrate using a doctor blade on a template made from a surface-ground steel plate. The basic slip formulation was similar to that described by Richards in the production of ZrO_2-Y_2O_3 slips.[2] The solvent was an azeotropic mixture of Ethanol and Methyl Ethyl Ketone (40/60 by weight). The MEK allowed for very thin layers to be deposited, and the Ethanol reduced volatility and increased the solubility of binder. Menhaden fish oil was added as a dispersant at 3 wt. % relative to solids, determined by Tormey *et al.* as the maximum adsorption obtainable in Al_2O_3/toluene slips.[3] After mixing ultrasonically for 30 minutes, 5% tertiary amide polymer binder was mixed in and mixing was continued for another 30 minutes. It was important to add the dispersant prior to the binder to prevent agglomeration, as competition for adsorption sites occurs.[4] The slip composition was vacuum degassed, warmed to 50°C, then deposited directly onto the SiC substrate with a doctor blade. The substrates had been ground flat, then polished to a

[i] Siemens Diffraktometer D500

[ii] Phillips EM400

1μm finish on a lapping wheel to ensure coplanarity. The reservoir volume ahead of the blade and blade speed was kept as constant as possible to ensure the repeatability of the process, which was monitored by weighing the specimens before and after deposition. The concentration of solids was kept at 0.6 g/ml and the doctor blade gap height set at 50-200 μm.

4.4 Joint preparation

4.4.1 Furnace Calibration

Furnace temperature control during ramp-up was maintained with a tungsten/rhenium type C thermocouple. During ramp-down, temperature was controlled with an optical pyrometer[i] sighted on the crucible, as its cooled slower than the furnace atmosphere at the thermocouple tip. Both the thermocouple and the pyrometer were calibrated using a portable optical pyrometer[i] attached to the front viewport of the furnace (see Figure 4-2). The absolute temperature at the melting points of Nickel (1453°C) and Palladium (1554°C) were verified and found to agree to within 5 degrees.

4.4.2 Heating schedule

The binder was removed by heating in air at 400°C for 4 hours, then cooling slowly to room temperature. The SiC rods (16 mm x 19 mm DIA) with cordierite layers were placed in a graphite die and a force of 500 g applied to ensure good contact was maintained. It was important to allow for a slip-fit between the graphite foil lining in the

[i] Ircon MR-0R10-99C

die and the sample, so that viscous flow permitted a uniform thickness, while at the same time ensuring good alignment. The samples were fired using the basic heating schedule of Figure 4-1. The ramp rate from 400°C was 60°C/min., and the peak temperature and dwell time were determined during the sessile drop experiments. The furnace elements were turned off and the parts cooled in vacuum below the lowest eutectic in the MgO-Al_2O_3-SiO_2 system, 1355°C, to remove any bubbles forming at the interface due to crystallization. Subsequently, flowing argon or helium gas was used to quench to just above the glass transition temperature (815°C). Nucleation dwell times of 1 and 5 hours were studied. The crystallization time and temperature were set at 1200°C for 1.5 hours.[5]

4.5 Characterization

Microstructural characterization was accomplished with thin-film x-ray diffraction, scanning electron microscopy (SEM)[ii], energy dispersive spectrometry (EDS)[iii], wavelength dispersive spectrometry (WDS)[iv], and transmission electron microscopy (TEM)[v] (courtesy Dr. W. MoberlyChan). Polishing of joints became critical, as the lower hardness interlayer was preferentially removed. Overpolishing produced relief at the interface, which could cause artifacts during EDS analysis due to the variation in the take-off angle of x-rays leaving near the interface. For SEM sample preparation, limiting the polishing time at each step was essential in keeping the joint intact, and etching in 2% HF

[i] Leeds and Northrup 8632-C

[ii] DS130C, ISI Inc.; Milpitas, CA

[iii] DX-4, EDAX Corp.; Mahwah, NJ

[iv] WDX-3PC, Microspec Corp.; Fremont, CA

[v] Phillips EM400, and Topcon ISI-002B

for 1 minute revealed the cordierite microstructure effectively. For TEM specimens, it was critical to cut the original slice as thin as possible to limit the thinning time using diamond compounds. Carbon coating[i] was used for EDS and WDS analysis, and for SEM image analysis platinum coatings[ii] were applied.

4.6 Mechanical properties

The mechanical properties of the joint were assessed with 4-point beam bending tests. The modulus of rupture was determined using the formula, $\sigma_r = 3sp/bh^2$, with s the span width, p the load, and b and h the width and height of the sample beam. Beams were cut to 3 x 3 x 30 mm size, and polished on a lapping wheel to 1 μm finish.

[i] MED-010, Pfeifer Balzers International; Balzers, Principality of Lichtenstein

[ii] Baltec SCD 050

4.7 References

1. A. Yurkov, B. Polyak, N. Manakhova, and I. Kazantsev, "Wetting of Silicon Carbide by Molten Aluminosilicate Glasses," *Ogneupory*, No.11, pp. 12-15 (1990).
2. V. Richards, "Adsorption of Dispersants on Zirconia Powder in Tape-Casting Slip Compositions," *J. Am. Ceram. Soc.*, 72 [2] 325-27 (1989).
3. E. Tormey, R. Pober, H. Bowen, P. Calvert, "Tape Casting Future Developments," in Advances in Ceramics, Vol. 9, *Forming of Ceramics.* Ed. J. Mangels and G. Messing, Am. Ceram. Soc., Columbus, OH (1983), pp. 140-49.
4. R. Moreno, "The Role of Slip Additives in Tape Casting Technology: Part II—Binders and Plasticizers," *Am. Ceram. Soc. Bull.*, 71 [11] 1627-57 (1992).
5. E. Stadnicar, Ferro Corp., private communication.

Chapter 5 Results and Discussion

5.1 Wetting

5.1.1 Effect of ramp rate

To assess the effect of ramp rate on contact angle, one specimen was heated at 5°C/min. to 1550°C, then quenched with flowing helium gas to the glass transition temperature (815°C). In contrast to specimens heated at high ramp rates (60°C/min) the sessile drop did not remain in intimate enough contact with the surface to form a continuous bond, forming instead a hollow cap of solid which was easily flicked off. Additionally, the milky white color attested to the phase separation and/or crystallization occurring which slowed the flow rate of the droplet enough to inhibit good spreading.

5.1.2 Effect of substrate precondition

The effects of substrate precondition on the equilibrium contact angle are shown in Figure 5-1. With no preconditioning, the contact angle remained unacceptably high, 110°, after 60 minutes at 1550°C. Oxidation, kaolin glazing, and titanium ion implantation (150 KeV accelerator voltage, $10^{17}cm^{-2}$ flux, courtesy Dr. I. Brown) all served to decrease the contact angle to acceptable levels by providing a barrier to the unreacted SiC. The subsequent reaction was then not so severe as to totally disrupt the stability of the sessile drop, as evidenced by the near cessation of bubbling at the interface after approximately 30 minutes at temperature. By this time the reaction phase formed was wet by the liquid droplet. The droplets on the preoxidized SiC substrates moved across the surface until an

equilibrium phase was established, while the droplets on the titanium implanted surfaces were stationary. Although the part glazed with kaolin (hydrated aluminum silicate) showed the best result, the droplet was partially crystallized and did not adhere well after cooling.

5.1.3 Effect of peak temperature and dwell time

The effects of peak temperature and dwell time on the equilibrium contact angle were studied using preoxidized substrates and titanium implanted substrates (see Figures 5-2 and 5-3). In both cases was the contact angle minimum at a peak temperature of 1550°C, one hour dwell. However, cross-sections revealed more dewetting due to bubble formation at the interface for parts held 60 minutes. Since severe bubbling was observed to decrease dramatically at 30 minutes, a compromise of 1550°C for 30 minutes dwell was selected for further experimentation.

5.1.4 Effect of fluoride ion

The effect of a CaF_2 flux was observed on preoxidized substrates heated at 60°C/min. to just above the melting point of the undoped glass (1465°C), immediately followed by rapid cooling in flowing helium (30°C/min.) to the glass transition temperature. The flux lowered the melting point of the glass to 1400°C. In the sample without flux, two glass phases separated and wet the SiC substrate differently (Figure 5-4a). In the droplet on the right hand side, a network of needle-shaped silica crystallites is seen, interconnected with another phase which appears crystalline, and the contact angle

was measured at 100° (Figure 5-4b). In the droplet on the left hand side, however, the network is interconnected by an amorphous phase, and the contact angle was measured at 70° (Figure 5-4c). X-ray maps of Mg, Al, and Ba (Figures 5-4d-f) show enrichment of these elements in the wetting phase, and depletion in the nonwetting phase. In contrast, the sessile drop of the glass doped with 1 weight percent CaF_2 showed no phase separation, and a contact angle of 60°.

These effects can be attributed to the fluoride ion's ability to maintain a disordered network, thus inhibiting phase separation. Since phase separation is also not exhibited in non-doped glass heated to 1550°C, it is reasonable that the addition of the fluoride ion not only lowers the glass melting point, but allows for processing at lower temperatures by maintaining a homogeneous glassy state which exhibits better wetting characteristics on SiC. The fact that the glass doped with BaF_2 did not behave as well indicates that the introduction of more Ba^{2+} increases the glass surface tension and viscosity. The effects of the flux addition are shown in Figure 5-5, indicating that the CaF_2 flux enables the parts to be processed at 1500°C, lowered from 1550°C (see Figure 5-6).

5.1.5 Effect of quench rate

The effect of quench rate was observed in the color and degree of crystallinity of the sessile droplet. In parts slow cooled in vacuum, droplets were white in color and did not adhere well, indicating crystallization upon cooling. In parts quenched in flowing argon (approx. 13°C/min.), droplets were cloudy indicating some degree of phase separation had occurred.[1] By using flowing helium gas, with a much higher thermal

conductivity, 25°C/min cooling rates were obtained over the primary range of cordierite crystallization (1400-950°C). Clear sessile droplets were obtained indicating no phase separation, allowing for the controlled nucleation and crystallization of cordierite.

5.1.6 Characterization

Interface characterization was accomplished with thin-film x-ray diffraction and TEM. Thin-film x-ray spectra were taken with the incident angle set at 2° on sessile drop samples deposited on preoxidized substrates and titanium implanted substrates. The parts received the full heat treatment process, so as to identify the final interfacial phase if a phase transformation at the interface occurred during crystallization. The droplets were made large enough so that the volume contraction during crystallization aided in breaking them off, leaving a thin reaction phase behind.

The x-ray spectrum for the preoxidized substrate is shown in Figure 5-7. Three peaks other than those attributed to SiC are seen. At 10.56 Å, serpentine is seen, and at 2.384 Å, magnesium silicate hydroxide, both with the formula ($Mg_3Si_2O_5(OH)_4$). At 3.354 Å a distorted high quartz is observed, which is structurally analogous to μ-cordierite. Neither cordierite nor an oxycarbide glass phase is detected. The appearance of these phases is consistent with the theory of reactive wetting in which the SiC substrate is oxidized by the silicate glass.

The x-ray spectrum for the titanium implanted substrate is shown in Figure 5-8. The two peaks at 3.020 and 3.364 Å correspond to the titanium oxide Ti_7O_{13}, and the

peak at 4.094 Å to a silicon oxide, possibly an aluminum-stuffed silicate. Again neither cordierite or an oxycarbide glass is seen.

TEM was performed (courtesy Dr. W. MoberlyChan) on two preoxidized samples, one nucleated for one hour, and the other for five hours, prior to crystallization (see Figure 5-9). Evidence of a phase transformation at the interface is seen as the part with the short dwell shows a Ba-enriched silicate glass at the interface, contrasting with the crystalline cordierite observed in the part with the five hour nucleation dwell. This lends support to the theory that a sufficient nucleation dwell is required to precipitate the Ba containing precursor phases required for the controlled crystallization of cordierite.

5.1.7 Conclusions

The following conclusions summarize the results of the wetting experiments.

- A fast ramp rate to peak temperature (60°C/min.) was required to maintain a homogeneous glass with good flow characteristics and wetting.
- Preoxidizing or Ti-implantation was required to obtain acceptable wetting. The droplets on preoxidized parts were mobile, while those on Ti-implanted parts were stable.
- An optimum combination of peak temperature and dwell time that minimized both the contact angle and interfacial dewetting was found to be 1550°C, 30 minutes for the undoped glass; and 1500°C, 30 minutes for the glass doped with 1 weight percent CaF_2 flux. 60° contact angles were obtained.

- Doping with CaF_2 flux delayed the phase separation inherent in the glass, allowing for processing at a lower temperature (1500°C). Wetting was facilitated by the reduced surface tension of the glass. BaF_2 as the source of fluoride ion was not as effective, probably because Ba^{2+} tends to increase glass viscosity and surface tension.
- Rapid quench rates (25°C/min.) in flowing helium gas were required to limit phase separation and crystallization upon cooling.

5.2 Tape Casting

Quantification of the tape casting process was crucial in removing processing conditions as uncontrolled variables. Slurry viscosity, mixing conditions, and blade gap height were the most observable quantities of interest. Table 5-1 lists the input conditions leading to the final joint thickness obtained.

Table 5-1 Input and Output Parameters for Tape Casting Process

Slurry Viscosity (g/cc)	*Doctor Blade Gap Height (mm)*	*Mass of as-deposited film (g)*	*Final Joint Thickness (μm)*
0.6	.05	.004-.005	5
0.6	.08	.008	13
0.6	.10	.012	20
0.6	.15	.016	31
0.6	.20	.019	37

5.3 Nucleation

5.3.1 Effect of quench rate on morphology

The effect of quench rate on phase morphology is illustrated in Figures 5-10a-c, SEM micrographs of joints with slow cooling (10°C/min.) and rapid cooling (25°C/min.) to the glass transition temperature of 815°C, immediately followed by slow cooling to room temperature. Slow cooling produced nucleation and growth of large polygonal and dendritic crystals at the SiC interface (Figures 5-10a and b). EDS analysis showed the relative enrichment of aluminum in the polygonal crystals, indicative of the presence of mullite. The dendritic crystals are indicative of cordierite, as confirmed by TEM in Figure 5-11 (courtesy Dr. W. MoberlyChan). In contrast, joints with rapid cooling showed no evidence of crystallization, and the morphology appears indistinct (Figure 5-10c).

5.3.2 Effect of nucleation dwell and quench rate on phase separation morphology

The effect of the 5 hour nucleation dwell at 850°C is illustrated in Figure 5-12, SEM micrographs showing a dispersion of secondary phase in a glassy matrix. WDS line scans across such a joint indicates the relative enrichment of barium (Figures 5-12b). When enough time is allowed for the dispersion to come to completion, nucleation and growth of cordierite in the bulk is promoted, as evidenced in Figure 5-13, which shows the loss of preferential orientation of cordierite with increasing dwell time and quench rate. In (a), crystallized from slow cooling with no nucleation dwell, the x-ray scan shows the absence of secondary cordierite peaks, indicative of a high degree of crystallographic texturing. It is likely that this microstructure is comprised of interface nucleated grains which completely span the joint. In (b), crystallized from slow cooling with a 5 hour nucleation

dwell, secondary peaks occur, but they are disproportionate to the main peak, and the corresponding microstructure shows elongated grains on the order of 2 μm size.*

In Figure 5-13c, crystallized from rapid cooling with a 5 hour nucleation dwell, no texturing occurred as the proper ratio of cordierite peak intensities is observed. The corresponding microstructure shows equiaxed grains on the order of 0.3 μm size. These samples were prepared for the diffractometer by fracturing open joints; the joint of Figure 5-13c was so strong that only a small surface area could be exposed, and the spectrum had to be magnified by 10X due to the small sampling volume to compare the peak heights. Thus it can be concluded that the rapid quench rate in combination with a sufficiently long nucleation dwell promotes a controlled, evenly distributed dispersion of the secondary phase which leads to a fine grain equiaxed final microstructure.

5.3.3 Heterogeneous nucleation of cordierite

Glass-ceramics are versatile materials since they allow for the *controlled* crystallization and growth of desired phases. The dispersion of a secondary emulsion phase in the rapidly quenched glassy matrix enables the subsequent crystallization of precursor phases which closely resemble the desired phase structurally. In the BaO doped glass studied here, the barium silicate $3BaO \cdot 5SiO_2$ was shown to form in glass powders pulled after the quench and nucleation stages, and prior to crystallization. This is illustrated in Figure 5-14, thin-film x-ray spectra run at 2°. In (a), removed immediately after quench, the barium silicate peak at 3.75 Å is discernible, along with the silica peak at

* Grain size determined by drawing a series of concentric circles on the SEM micrograph, with d=C/NM, where C is the circumference, N the number of grain boundary intersections, and M the magnification.

4.17 Å. The ratio of peak heights, corrected for background, was 0.28. In (b), removed after quench and 5 hour nucleation, the same peaks occur, with a corrected peak intensity ratio of 0.37. It is likely that the SiO_2 peak noted corresponds to a stuffed β-quartz derivative, as no crystalline silica peak matches it conclusively. The higher silicate : silica peak intensity ratio after 5 hours nucleation signals the more complete phase separation with associated diffusion of barium to form the silicate.

The hypothesis that a barium silicate forms which serves as a heterogeneous nucleation site for cordierite is difficult to verify experimentally because of the "hit-and-miss" nature of transmission electron microscopy. Direct experimental evidence with the TEM was not obtained during these studies, but the silicate sanbornite, $BaO \cdot 2SiO_2$, is the most likely candidate to act as the nucleating agent. The d-spacings of three low index sanbornite planes are within 3% of those of three low index planes of α-cordierite. In addition, the peak at 3.42 Å ($2\theta = 26°$) in Figure 5-14c (x-ray spectra of powders after quench, nucleation, and crystallization at 1200 °C for 1.5 hours) matches the (121) sanbornite peak. Table 5-2 displays the crystallographic orientation relations and lattice misfits for epitaxial growth of α-cordierite on sanbornite.

Table 5-2 Crystallographic orientation relations and lattice misfits for epitaxial growth of α-cordierite. on sanbornite

Lattice Periods (Å)		Misfit (%)*
α-cordierite	Sanbornite	
d(112) = 3.379	d(220) = 3.343	1.1
d(202) = 3.138	d(140) = 3.097	1.3
d(102) = 4.094	d(101) = 3.973	3.0

*Misfit % = 100(b-a)/a, where a = lattice spacing of substrate crystal (sanbornite) and b = lattice spacing of overgrowth crystal (cordierite)

For the silicate sanbornite to be present during the heat treatment process, it must either have been formed during the nucleation stage or crystallized from the barium rich emulsion phase which formed. For example, the compound $3BaO \cdot 5SiO_2$ detected after cooling to room temperature may be the more stable low temperature compound simply to enable barium to form more bonds in the structure, thus lowering the internal energy. Otherwise the reaction $3BaO \cdot 5SiO_2 + SiO_2 \rightarrow 3(BaO \cdot 2SiO_2)$ must occur as the material is heated. To assess this possibility thermodynamically the heat capacity/temperature relation for these compounds is needed so that the free energy change can be calculated. This information is not available, but as an approximation the increase in entropy associated with this reaction would make it favorable. A comparison of the structures and lattice spacings of the two silicates supports this explanation. Transforming from one large monoclinic unit cell of $3BaO \cdot 5SiO_2$, with lattice edges 4.7, 13.9, and 20.2 Å, $\beta = 98.6°$; to three smaller orthorhombic unit cells of $BaO \cdot 2SiO_2$, with

lattice edges 4.7, 13.5, and 7.7 Å, $\beta = 90°$; would only involve a randomization in which barium and silicon, by going from a 3:5 to a 1:2 ratio, become more interchangeable on the lattice. In this scenario not only are three unit cells produced from one, but the number of ways in which barium and silicon can be arranged in the structure is increased.

5.4 Crystallization

5.4.1 Crystallization mechanism

Joints cooled slowly from the glass melting point exhibited interface nucleation of cordierite grains, as seen in Figure 5-10. To examine the growth kinetics of cordierite, WDS line scans across the joint and intersecting the cordierite dendrite were performed, with the results given in Figure 5-15. The line scans show the relative enrichment of magnesium and aluminum in the growing dendrite, with the matrix phase slightly higher in silicon. Most striking is the appearance of a large barium peak at the tip of the advancing dendrite, indicative of rejection of barium from the crystal lattice. This leaves a residual phase which is rich in barium and silicon, and poor in magnesium and aluminum.

5.4.2 Bulk crystallization in cordierite joints

The absence of an amorphous region in the powder x-ray spectrum of Figure 5-14c and in the x-ray spectrum of the exposed joint in Figure 5-13c indicates nearly complete crystallization is taking place. The question arises as to how to explain this in light of the preferential etching rates which reveal a 2-phase appearing microstructure resembling cordierite crystallizing out of a glassy matrix. Referring to the MgO-Al_2O_3-SiO_2 phase diagram (Figure 3-2) cordierite melts incongruently into a mullite containing

liquid, and mullite is detected in the x-ray spectrum of Figure 5-14c. Given that no spinel or cristobalite is observed in the spectrum, it is probable that the residual-glass appearing secondary phase is in fact a crystalline species, with x-ray peaks overlapping the main peaks in the spectra. The peak at 3.42 Å, postulated as belonging to sanbornite, would also match β-quartz, but its intensity is too small to account for the volume fraction observed in the SEM. It is likely that a stuffed β-quartz derivative structure containing magnesium and aluminum, with d-spacings close to those of cordierite, and possibly entering into solid solution with cordierite, exists. Although not a totally conclusive argument, it is in agreement with the findings of the powder and sessile drop interface thin film diffraction patterns. Thus the final microstructure observed in Figure 5-16 is likely to be composed of α-cordierite, mullite, stuffed β-quartz, and residual barium-rich silicate glass.

Figure 5-16 shows two fine-grained polycrystalline microstructures examined to demonstrate the crystallization behavior in these joints. Both were crystallized at 1200°C for 90 minutes. Etching in 2% HF preferentially removed the quartz and glassy phases and revealed the 2-phase-appearing morphology distinctly. The average grain size was approximately 0.3 μm, and the volume fraction of the preferentially etched phase (quartz and residual glass) was found to be 36% for (a) and 32% for (b), as determined by the lineal intercept method described by Kingery, *et al.*[1] The volume fraction of residual amorphous phase was taken to be 5% (a liberal estimate), accumulating in triple pockets during crystallization. The 12% volume fraction of mullite was found by direct comparison of the integrated peak intensities of the (111) mullite and (102) α-cordierite

peaks. These peaks were chosen because they are distinctly resolvable in the spectrum (no overlapping peaks), and have identical I/I_o ratios of 0.5. Table 5-3 lists the composition of the polycrystalline joint material.

Table 5-3 Composition of Interlayer Material

Phase	Volume Fraction (%)
α-cordierite	54
Stuffed β-quartz	29
Mullite	12
Barium-rich residual glass	5

5.4.3 Coefficient of thermal expansion of interlayer

The coefficient of thermal expansion (0-1000°C) of the interlayer was calculated at 5.2×10^{-6} /°C, using equation 3-17,

$$\alpha = \frac{\sum \alpha B_i W_i / \rho_i}{\sum B_i W_i / \rho_i} \qquad (5\text{-}1)$$

and the data shown in Table 5-4. The thermal expansion coefficient of the residual glass phase was determined using the empirical equation developed by Morey for silicate glasses,[2]

$$\alpha = \Sigma f_i W_i \qquad (5\text{-}2)$$

where W is the weight fraction and f a numerical constant for the oxide constituents of the glass. A liberal estimate of 25 weight % was assumed for the BaO content in the glass.

The bulk modulus was determined using the relation B = E/3(1-2ν). All other properties, unless otherwise noted, were obtained in a materials handbook.[3]

Table 5-4 Parameters for determination of coefficient of thermal expansion

Phase	*CTE (X 10^6, 0-1000°C)*	*Bulk Modulus (GPa)*	*Elastic Modulus (GPa)*	*Poisson's Ratio*	*Density (g/cc)*
α-cordierite	2.5[4]	133	232[4]	0.21	2.67[4]
Stuffed β-quartz	14.58	76.9	151	0.20	2.50
Mullite	5.1	308	484	0.238	2.93
Residual glass	4.3	76	150[4]	0.17*	2.2*
α-SiC	5.1	340	637	0.19	3.21

* Obtained for vitreous silica

It is clear from these properties that the easiest way to tailor the thermal expansion coefficient of the composite interlayer is to change the extent of cordierite crystallization. Longer hold times at the crystallization temperature would lower the CTE by furthering cordierite grain growth at the expense of the quartz phase. This would also tend to improve the toughness of the material by providing more frictional sliding surface area for grain pullout and crack deflection.[5] Since larger grains also provide for larger flaw initiation points, however, the proper trade-off between strength and toughness is necessary to optimize the mechanical integrity of the joint. Also, reducing the CTE too much will lead to thermal stresses which could weaken the joint. In any case, the absence of a glass phase is advantageous for the radiation, thermal shock, and creep resistance of the material.

5.5 Mechanical properties

Given the process parameters described here, the modulus of rupture, as determined by 4 point beam bending tests, was found to be most sensitive to the amount of coverage of the interlayer material. The main secondary effect was interlayer thickness. These effects are illustrated for the preoxidized substrates in the plots of Figures 5-17 and 5-18. The thickness effect is essentially due to three factors; 1) a smaller sampling volume reduces the probability of finding a flaw of critical size for crack initiation and propagation; 2) more and/or larger imperfections due to processing exist in thicker layers, due to the lesser control of particle distribution during tape casting, and a 3% volume contraction associated with crystallization of this material[4]; and 3) the constrained volume of stress relief reduces the driving force for interface crack propagation caused by the elastic moduli mismatch. Test beams with strengths above the quoted modulus of rupture for cordierite (290 MPa) are not unexpected in thin joints with total coverage and can be attributed to the aforementioned effects. A maximum strength of 538 MPa was measured for a specimen with 5 μm interlayer thickness; this sample fractured into the bulk ceramic (see Figure 5-19).

Since fracture mechanics can be considered an extreme value problem, the entire process in the formulation of these SiC joints can be examined using Weibull statistics. A plot of ln ln $(1/P_S)$ vs. ln σ_F, where P_S is the probability of survival and σ_F the rupture strength, gives a slope which is proportional to the critical flaw density distribution in the material, or process. For monolithic ceramics a slope of 10 is good, and 20 is considered excellent. For joints, however, the slope is not a direct indication of the flaw density

distribution in the interlayer material, rather one of the "robustness" of the entire process, including control of wetting coverage and interlayer thickness.

In the Weibull plots of Figures 5-20 through 5-23, two sets of data are presented; one displaying the distribution for the entire sample set, and the other showing the distribution for those joints which had greater than 85% wetting coverage. All parts had less than 7 μm interlayer thickness. For the preoxidized substrates, the slope of the Weibull plot shows an increase from 1.2 to 7.0 (Figures 5-20 and 5-21), while for the titanium ion-implanted substrates, the slope increases from 3.1 to 5.7 (1 μm finish), and from 3.4 to 3.9 (as-ground finish). A trend in strength is also seen. The joints prepared from preoxidized substrates had higher fracture strength values than the titanium ion-implanted joints. This is explained in terms of the residual stress in the substrate surface imposed by the implantation process, leading to a higher interface failure rate in the ion-implanted samples. It is also possible that the titanium oxide interfacial reaction product existing in the titanium-ion implanted surfaces is not as well adhered as the silicate present in the preoxidized surfaces. Of the two ion-implanted surfaces studied, the 1 μm surface finished parts were slightly stronger than the as-ground parts.. However, the as-ground parts showed more resiliency to the variability of wetting coverage than the 1 μm parts, as evidenced by the slightly higher Weibull slope in Figure 5-22 (3.4 versus 3.1) Presumably, this is due to the enhanced reactive spreading on a rougher surface with greater surface area, as the rougher surfaces showed somewhat better coverage. The situation is reversed, though, when only parts with > 85% coverage are plotted (Figure 5-23), due to smaller flaw initiation points present at the 1 μm interface. Thus it can be concluded that

if greater than 85% wetting coverage can be achieved, a fine polished surface finish is preferred. Otherwise, a rougher finish should be used. In either case, the preoxidized substrates yield the best results, and also should show superior oxidation resistance.

As an example of the usefulness of the statistical analysis of fracture, suppose a service stress of 250 MPa is expected. Assuming that wetting coverage greater than 85% can be achieved, using a preoxidized substrate, less than 5% of parts in use will fail at stresses exceeding 350 MPa. However, greater than 30% of parts with 1 μm titanium ion-implanted substrates, and greater than 60% of parts with as-ground titanium ion-implanted substrates, would fail at a stress level of 250 MPa. For this level of stress, then, the preoxidized substrate is required. Suppose, however, that 85% wetting coverage cannot be obtained, and that stress levels are much lower, for example, 100 MPa. Using 1 μm ion-implanted substrates, the failure rate would be less than 5%, while for preoxidized substrates, it would be greater than 30%.

5.6 Radiation effects

Since SiC is a prime candidate for fusion reactor first wall components, an analysis of the radiation resistance of the joining medium is essential in the design process. The two primary concerns are the activation of the elements under irradiation (for rework and repair considerations), and structural damage (for mechanical reliability concerns).[6]

5.6.1 Activation

Gamma-ray emitting radioactive nuclides formed from cordierite bombarded with high levels of neutron radiation would include at least ^{24}Na, ^{28}Al, and ^{137}Ba. ^{24}Na and ^{28}Al

would exist due to the presence of SiC itself, so the risk posed by ^{137}Ba would have to be assessed, and if necessary a substitute nucleating agent, such as TiO_2, employed.[7]

5.6.2 Structural damage

The primary reliability concern arises from amorphisation caused by lattice displacement. In this regard it has been shown that materials with high ionic character have higher threshold energies for amorphisation than purely covalent materials, as the need to maintain charge neutrality and the omnidirectionality of ionic bonding make the amorphous state less readily accommodated.[8] The high ionic character of Al_2O_3 (62%) and MgO (73%) compared to SiC (13%) designates cordierite as potentially superior to other methods such as reaction bonding, which produces a porous SiC layer with an excess of metallic silicon (100% covalent) in the joint.

5.7 Conclusions

A high strength room temperature SiC/SiC joint, in excess of 500 MPa, can be obtained using a cordierite glass-ceramic, provided good wetting coverage (> 95%) with a thin layer (< 7 μm) can be achieved. These conditions were arrived at by processing in vacuum, quenching from high temperature in flowing helium, preconditioning the SiC substrate by either preoxidation or ion implantation to enhance reactive wetting, and doping the glass with fluoride ion to reduce surface tension and viscosity. Control of the nucleation and crystallization conditions is essential in producing a fine grained, equiaxed microstructure with a coefficient of thermal expansion matching that of α-SiC.

5.8 References

1. W. Kingery, H. Bowen, and D. Uhlmann, in *Introduction to Ceramics*, 2nd ed., John Wiley and Sons, New York, (1976), chapters 7,11.
2. G. Morey, *The Properties of Glass*, 2nd. ed., Reinhold, New York, (1954).
3. CRC Handbook of Materials Science and Engineering, ed. J. Shackelford and W. Alexander, CRC Press, Inc., Boca Raton, FL, (1992).
4. Ferro Corp., EG-0221 product data.
5. W. Zdaniewski, P. Shah, and H. Kirchner, "Crystallization Toughening of Ceramic Adhesives for Joining Alumina," *Advanced Ceramic Materials* **2** [3A] 204-08 (1987).
6. P. Rocco, H. Scholz, and M. Zucchetti, "Silicon carbide and the new low activation requirements for a fusion reactor first wall," *J. Nuclear. Materials*, **191-94** 1474-79 (1992).
7. S. Nargolwalla and E. Przybylowicz, in Activation Analysis with Neutron Generators, John Wiley and Sons, New York, NY, (1973), pp. 282-624.
8. P. Burnett and T. Page, "Criteria for Mechanical Property Modifications of Ceramic Surfaces by Ion Implantation," *Radiation Effects*, 97 283-96 (1986).

Chapter 6 Concluding Remarks

The highest fracture strength results were obtained with preoxidized substrates, where fracture occurred in the base material. With titanium ion-implanted substrates, failure occurred more often along the interface. However, the Weibull modulus for the ion-implanted parts was superior, indicating betting wetting coverage. In addition, the Weibull modulus for the ion-implanted parts processed with rougher surface finish was better than that for the fine polished substrates. However, for the sample set with a high degree of wetting coverage, the fine polished substrates performed better (Weibull modulus 5.7, compared to 3.9). Initial evaluation of the oxidative resistance of the joints (1000°C, 24 hours) indicated that the ion-implanted parts were unstable. The preoxidized parts showed no evidence of interfacial phase transformation, but surface grain growth was observed. Since cordierite recrystallization is expected above 900°C, some grain growth at the expense of the β-quartz phase is expected. Therefore, the parts should be annealed in air at or above the projected service temperature to ensure thermodynamic stability.

The technological viability of this approach can be more fully ascertained by studying the oxidation and creep resistance, along with response to neutron irradiation (for fusion reactor wall requirements). The peak temperature used excludes this material from joining of most SiC_f/SiC composites, but doping with higher concentrations of fluorine or other oxides can be explored in the hopes of producing a fugitive phase or other low expansion phases that further lower the melting point. Other work should focus on improving the wetting coverage. The slightly higher Weibull modulus of the as-ground

ion-implanted substrates is an encouraging result, and should be investigated with preoxidized substrates. The extreme sensitivity of the wetting process was demonstrated during an experiment designed to assess the effect of a rough surface with a preoxidized substrate, in which furnace contamination inhibited wetting, and compromised the results. In general, the high coplanarity, machining, and finishing requirements inherent in the joining of ceramics needs to be addressed before the process could be scaled up.

The processing window for a joining process, intended to produce materials to withstand high temperature environments without degrading the base materials of interest, is limited. . The highest toughness monolithic SiC ceramics would begin to evolve microstructurally and lose their *in situ* toughening properties above 1700°C. There is evidence that SiC_f/SiC composites can be fabricated to withstand maximum temperatures of 1400°C, if the fibers are first coated with carbon. This is a very expensive material to produce, however. The processing temperature for superalloys would have to be under 1100°C to prevent the loss of dispersion strengthening designed into these materials. Even if the part could be reheat-treated subsequent to joining, the melting points of Inconel 718 and Inconel 600 are 1260 and 1365°C, respectively. Doping with higher concentrations of alkali metal oxides, the most promising of which is Li_2O, would significantly lower the melting point of a cordierite-based glass-ceramic, without an associated increase in the coefficient of thermal expansion (due to the low expansion spodumene and β-eucryptite phases expected to form). It has already been demonstrated that minor additions of fluxing agents such as CaF_2 can lower the contact angle of the glass on the SiC substrate. In addition, the high ionic character of cordierite, along with

the fully dense resulting interlayer, make it more radiation resistant than reaction-bonded SiC joints, making it attractive as a nuclear material. Thus, glass-ceramics such as cordierite have emerged as a promising group of materials for joining, by having the intrinsic advantages of oxidation, thermal shock, and radiation resistance, as well as the chemical flexibility for adaptation to a multitude of different materials.

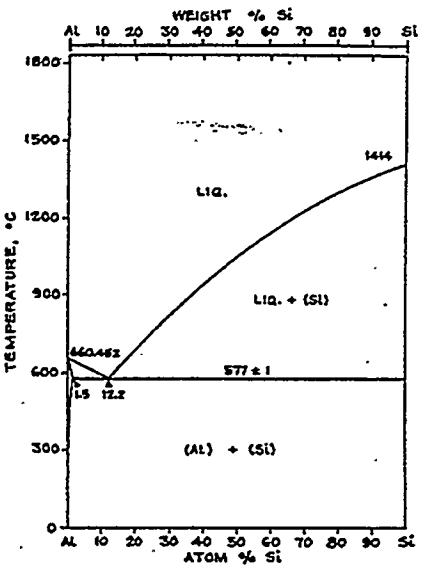

Figure 2-1. The Aluminum-Silicon system, taken from *Bull. Alloy Phase Diagrams* 5 (1), 1984.

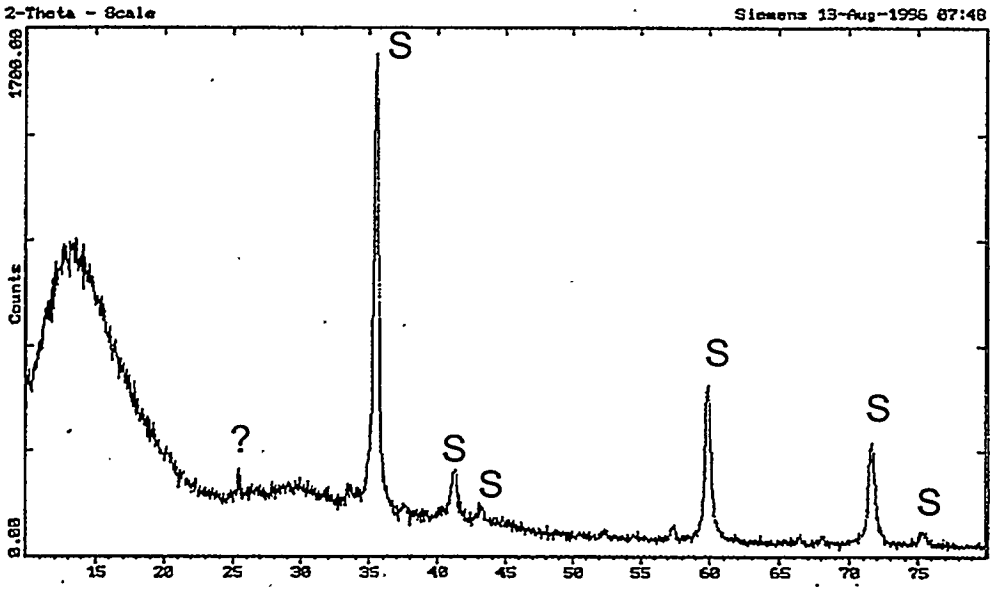

Figure 2-2. X-ray diffraction spectrum of reaction-bonding powder removed from joint. S = SiC.

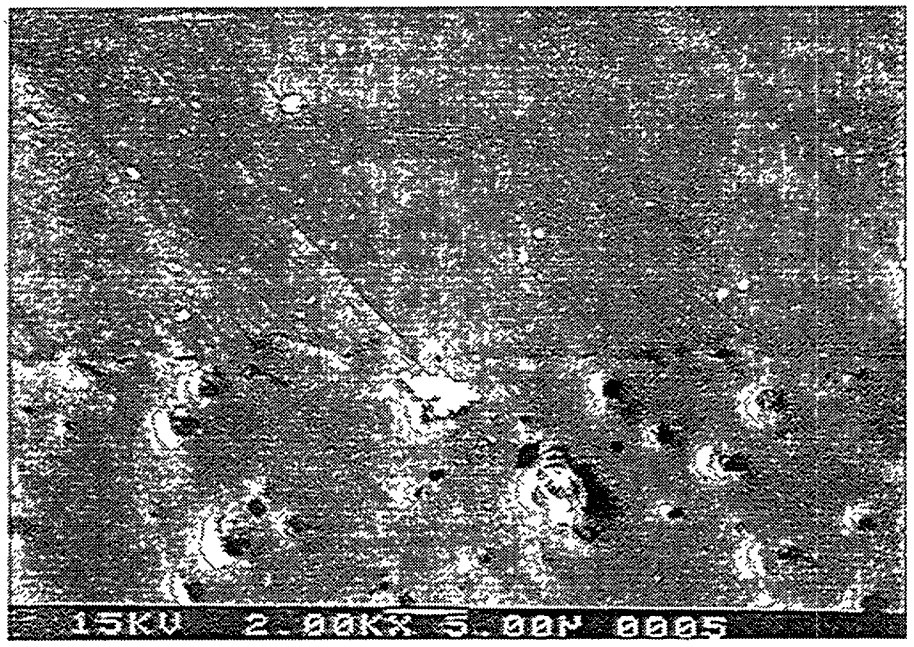

Figure 2-3. SEM micrograph of silicon (top) on dense SiC exhibiting the absence of infiltration.

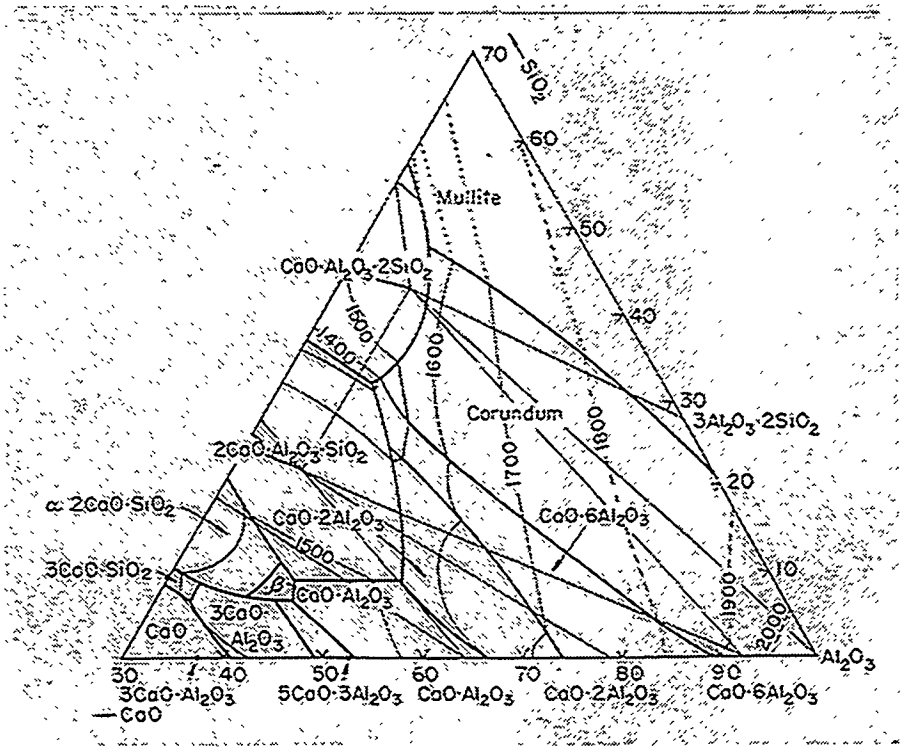

Figure 2-4. $CaO-Al_2O_3-SiO_2$ system, after A. Gentile and W. Forster, *J. Am. Ceram. Soc.* **46** (2) 76 (1963).

Before infiltration

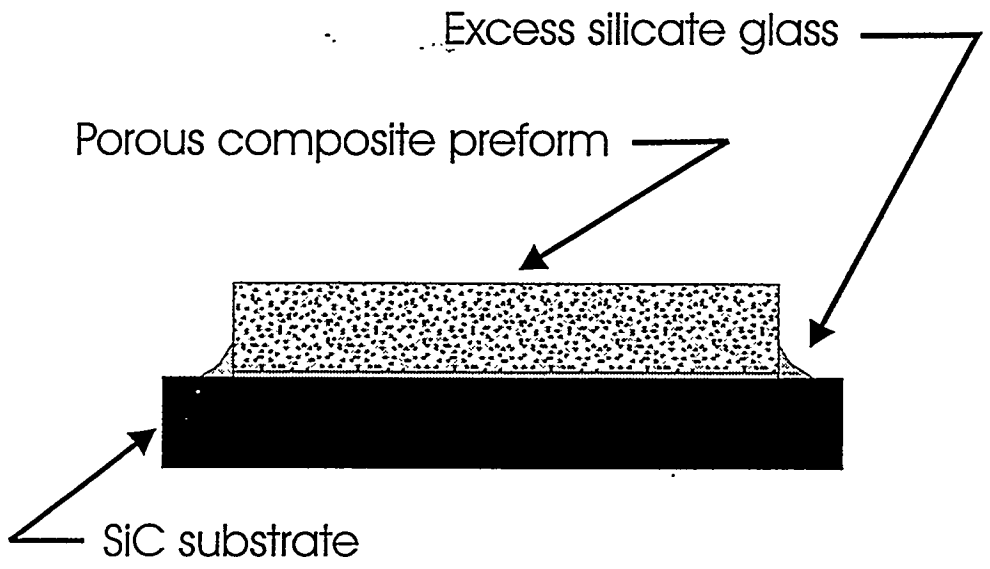

After infiltration

Pore-free infiltrated composite with
thin wetting layer to substrate

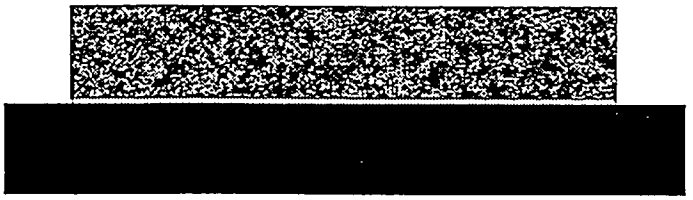

Figure 2-5. Schematic of reaction/infiltration process.

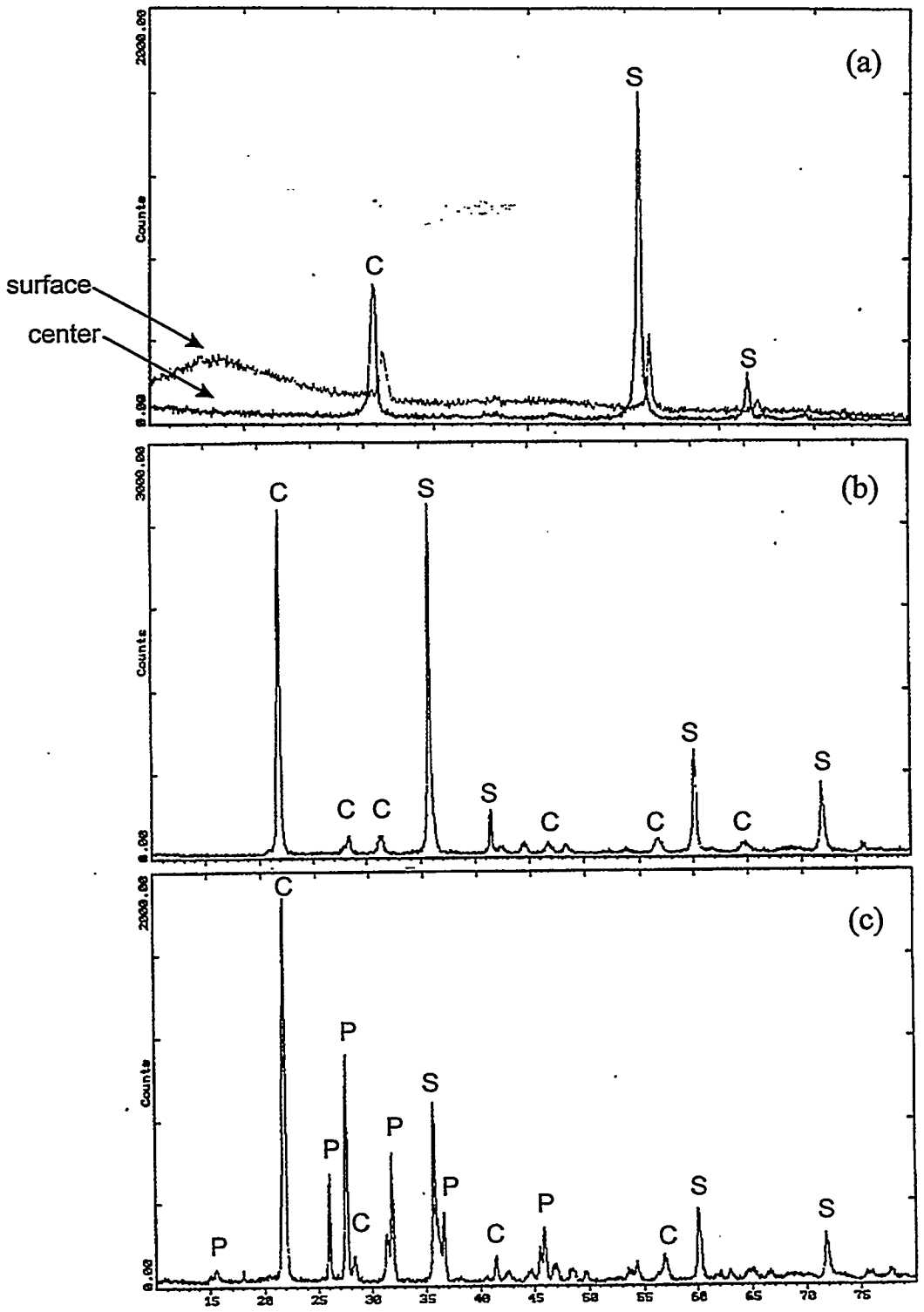

Figure 2-6. X-ray diffraction spectra of CAS 1170°C eutectic composites processed at a) 1200°C; b) 1350°C; and c) 1500°C, illustrating the progression of crystallization. C = cristobalite, S = SiC, P = pseudowollastonite.

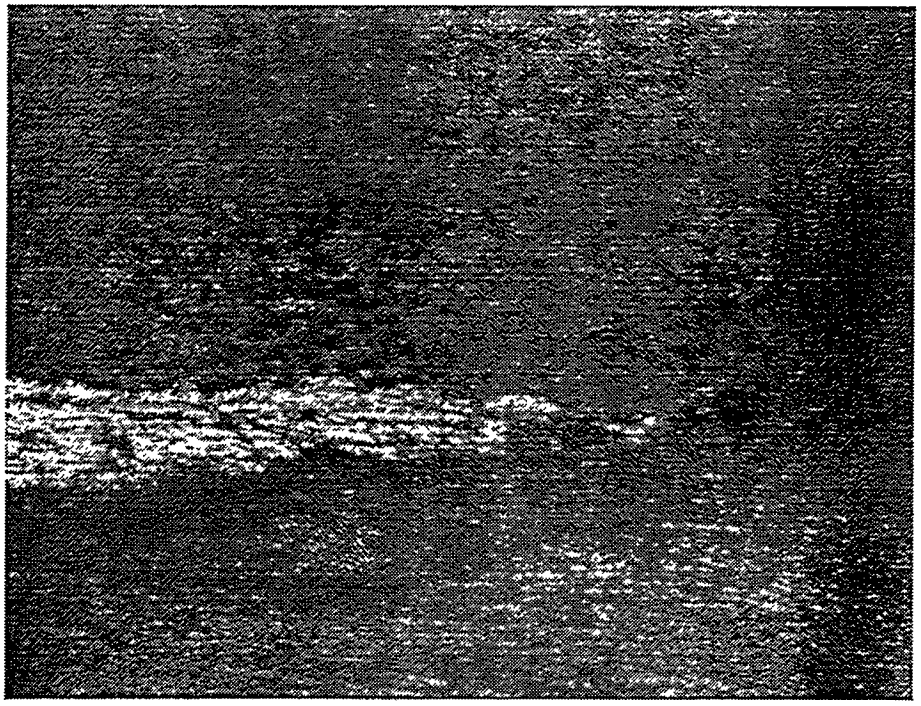

Figure 2-7. Optical micrograph of reaction/infiltration process with 1170°C eutectic glass. Note cracking in substrate.

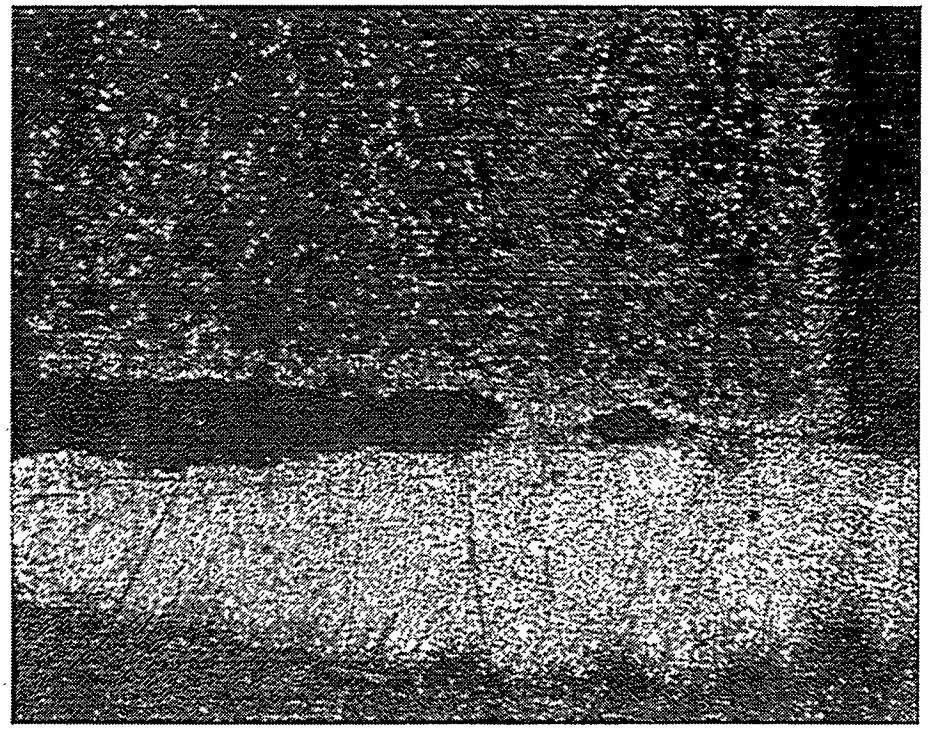

Figure 2-8. Optical micrograph (50X) of reaction/infiltration process with 1265°C eutectic glass, indicating warpage and debonding.

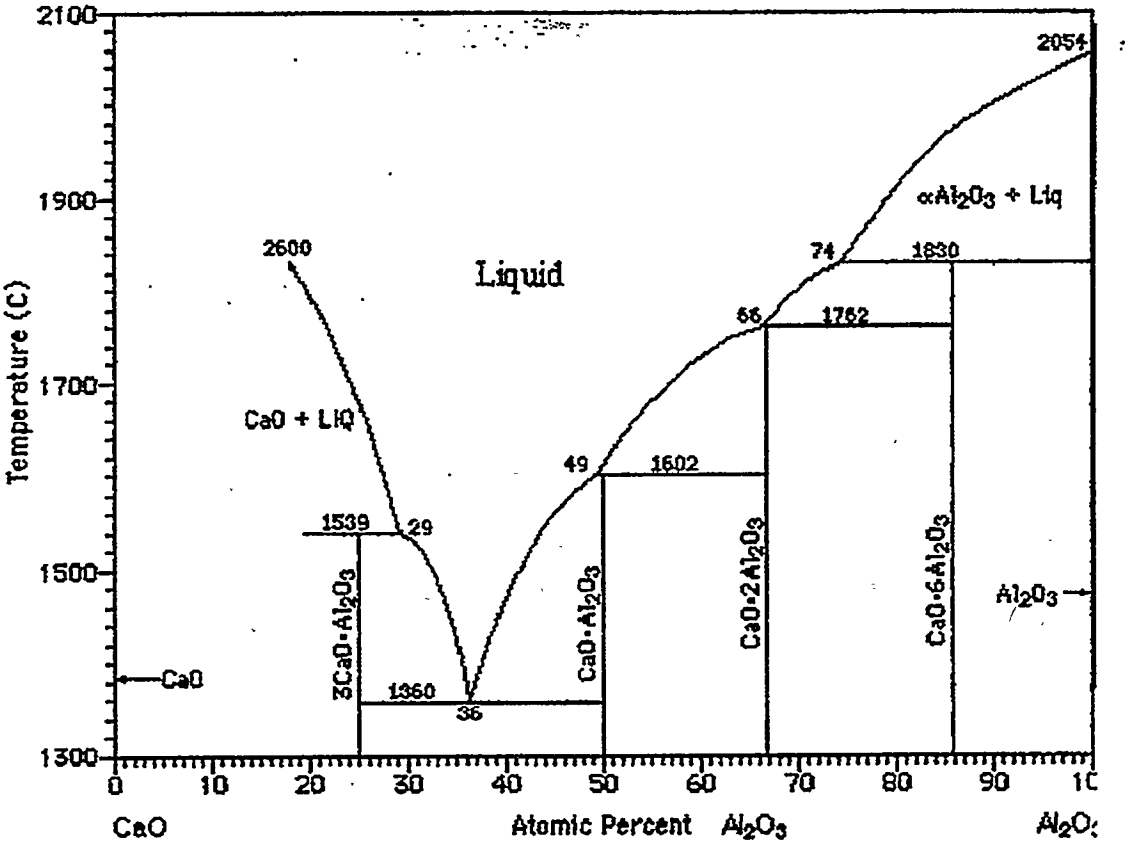

Figure 2-9. CaO-Al_2O_3 system, after E. Levine and H. McMurdie, *Phase Diagrams for Ceramists*, Vol. 3; Am. Ceram. Soc., Westerville, OH (1975).

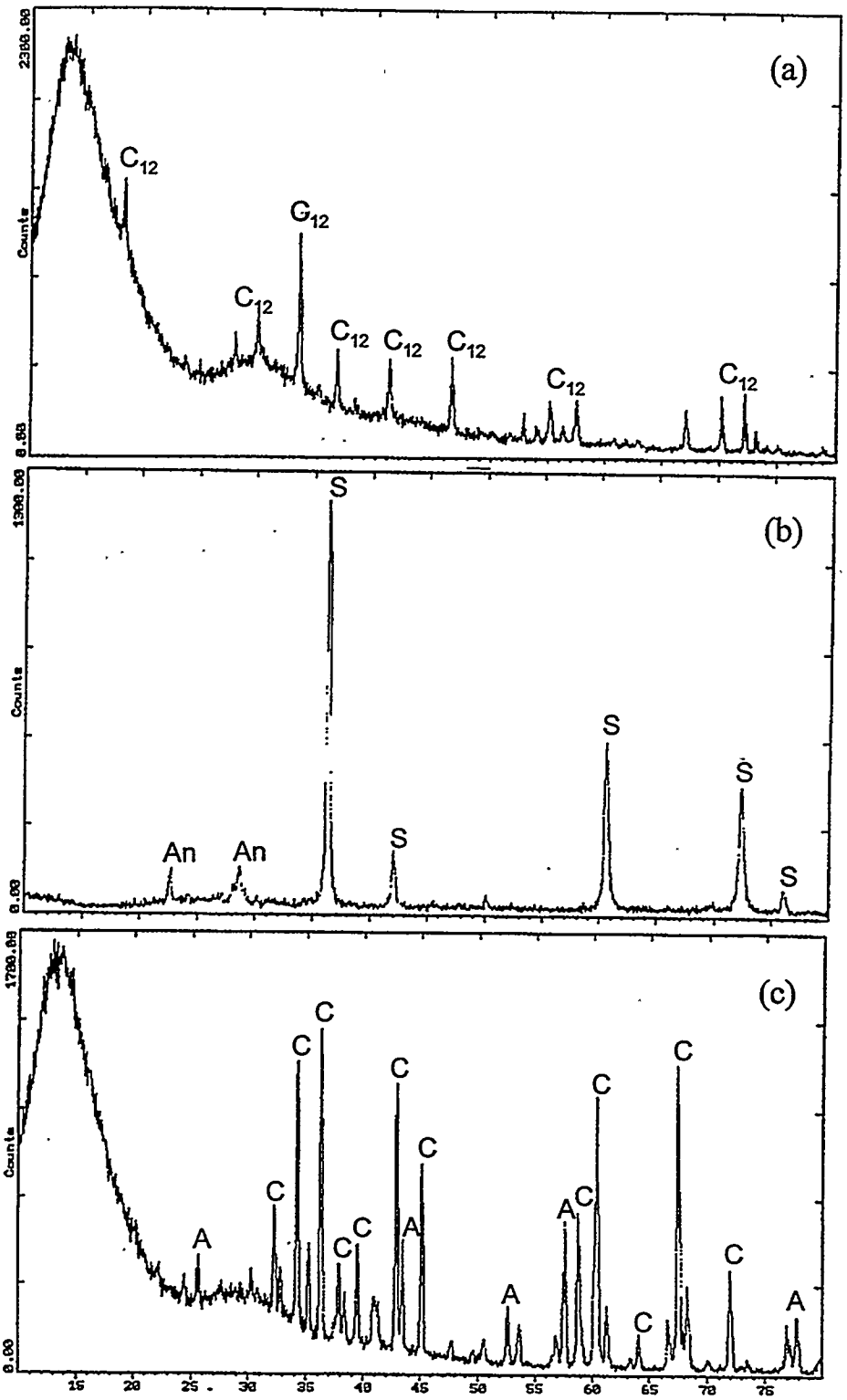

Figure 2-10. X-ray diffraction spectra of a) homogenized calcium aluminate powder; b) SiC/$C_{12}A_7$ composite mixture; and c) $C_{12}A_7$/excess Al_2O_3 composite mixture. A=Al_2O_3, C=CA_6, S=SiC, C_{12}=$C_{12}A_7$, An=Anorthite.

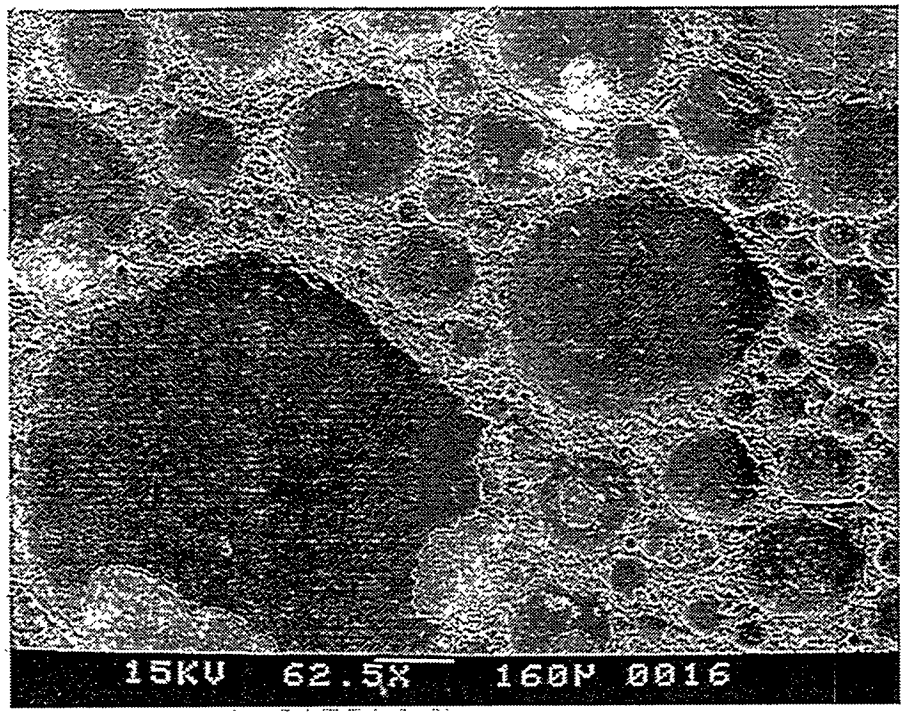

Figure 2-11. Calcium Aluminate film on SiC, fired in air at 1400°C.

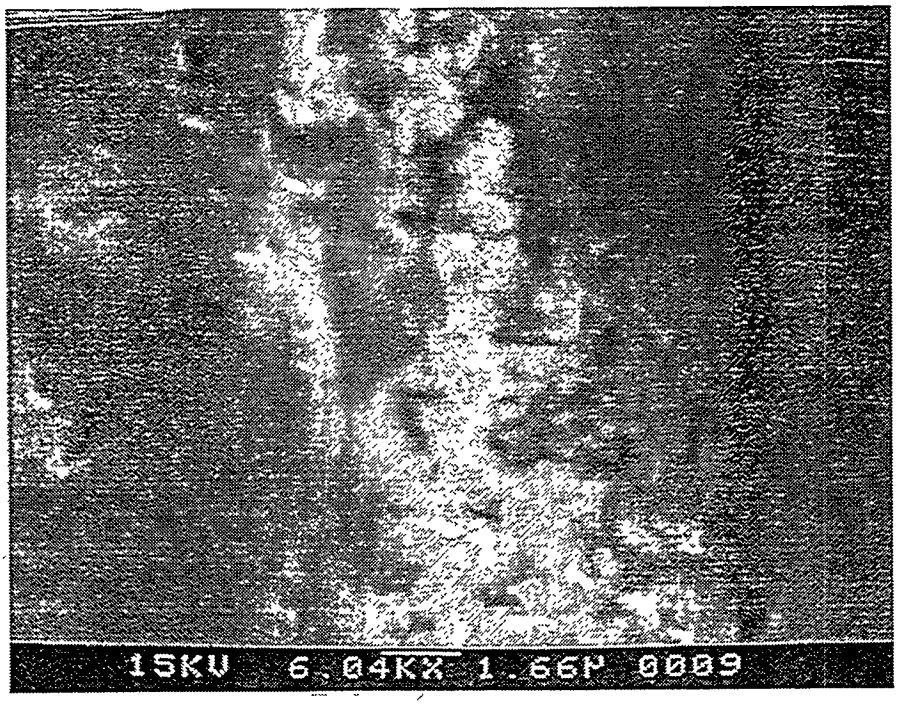

Figure 2-12. SEM micrograph of SiC/Calcium Aluminate joint interface, exhibiting formation of porous reaction byproduct.

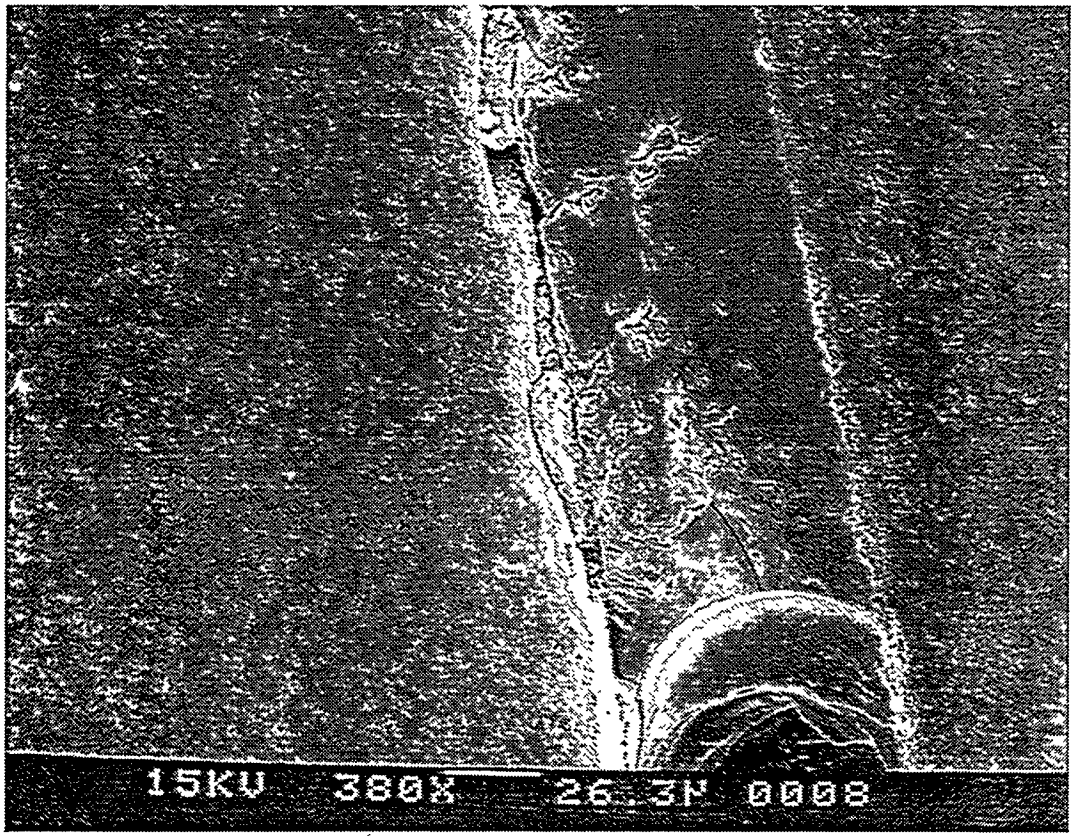

Figure 2-13. SiC/Calcium Aluminate joint, with crack propagating along interface.

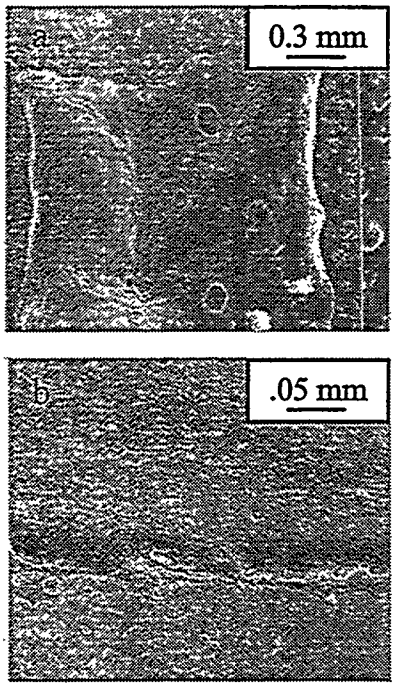

Cordierite film on SiC processed in a) air, b) argon.

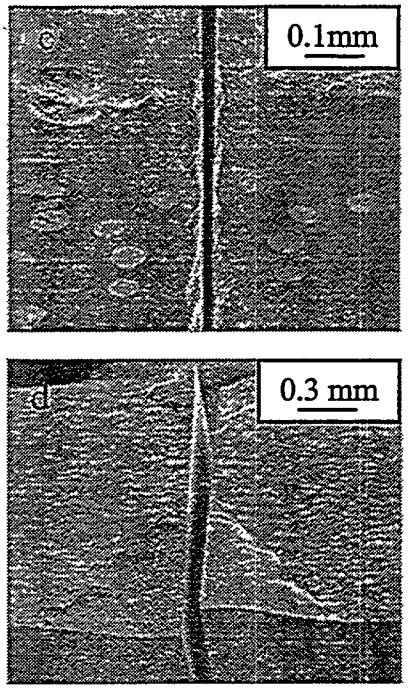

Matching fracture surfaces when processed in c) argon, d) vacuum. In vacuum voids due to bubbling are absent.

Figure 2-14. Processing atmosphere for SiC/Cordierite joining.

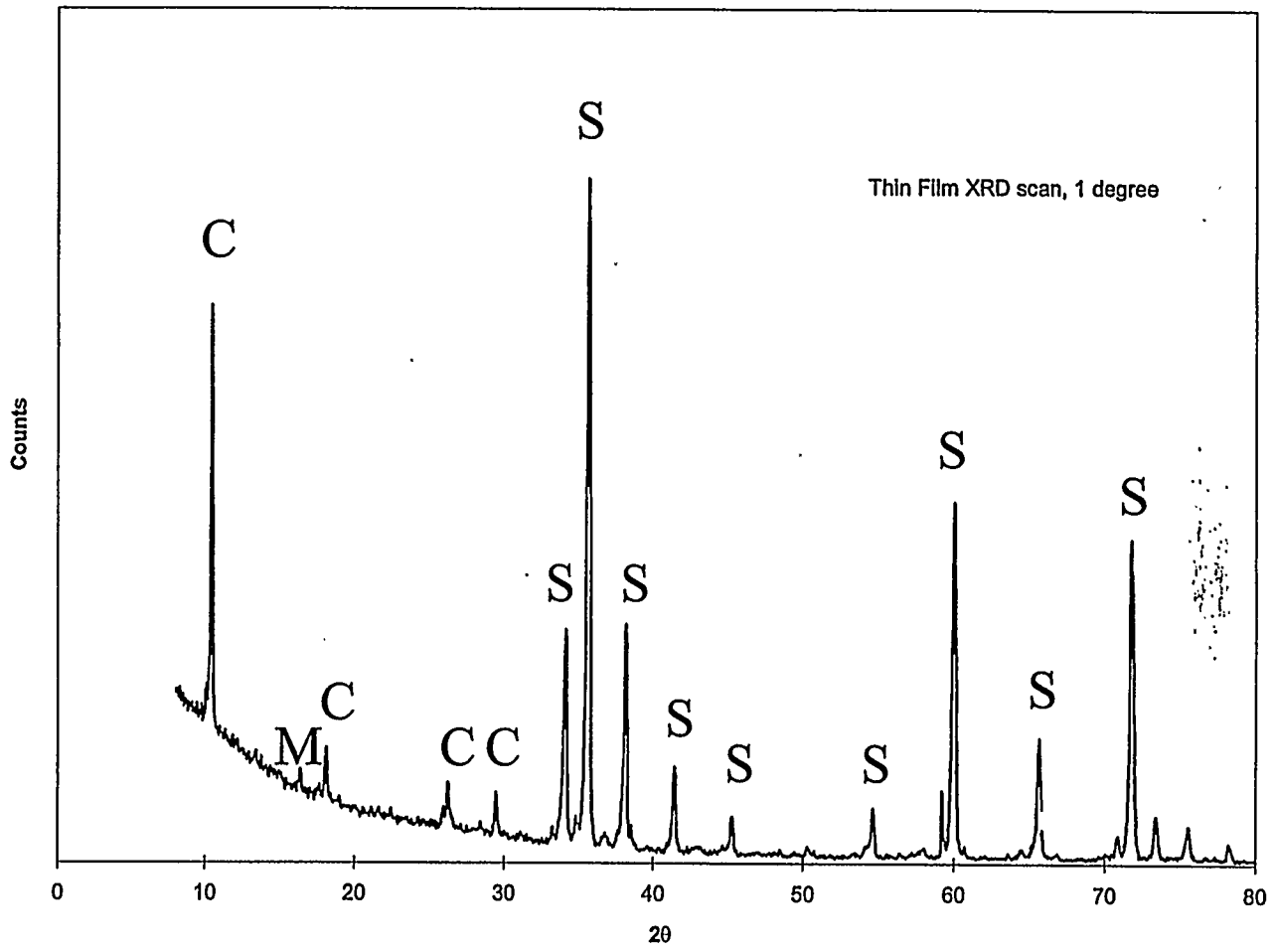

Figure 2-15. Thin-film x-ray spectrum of fractured SiC/cordierite joint. C = cordierite, M = mullite, S = SiC.

- No interface debonding seen
- Crack seeks low modulus material

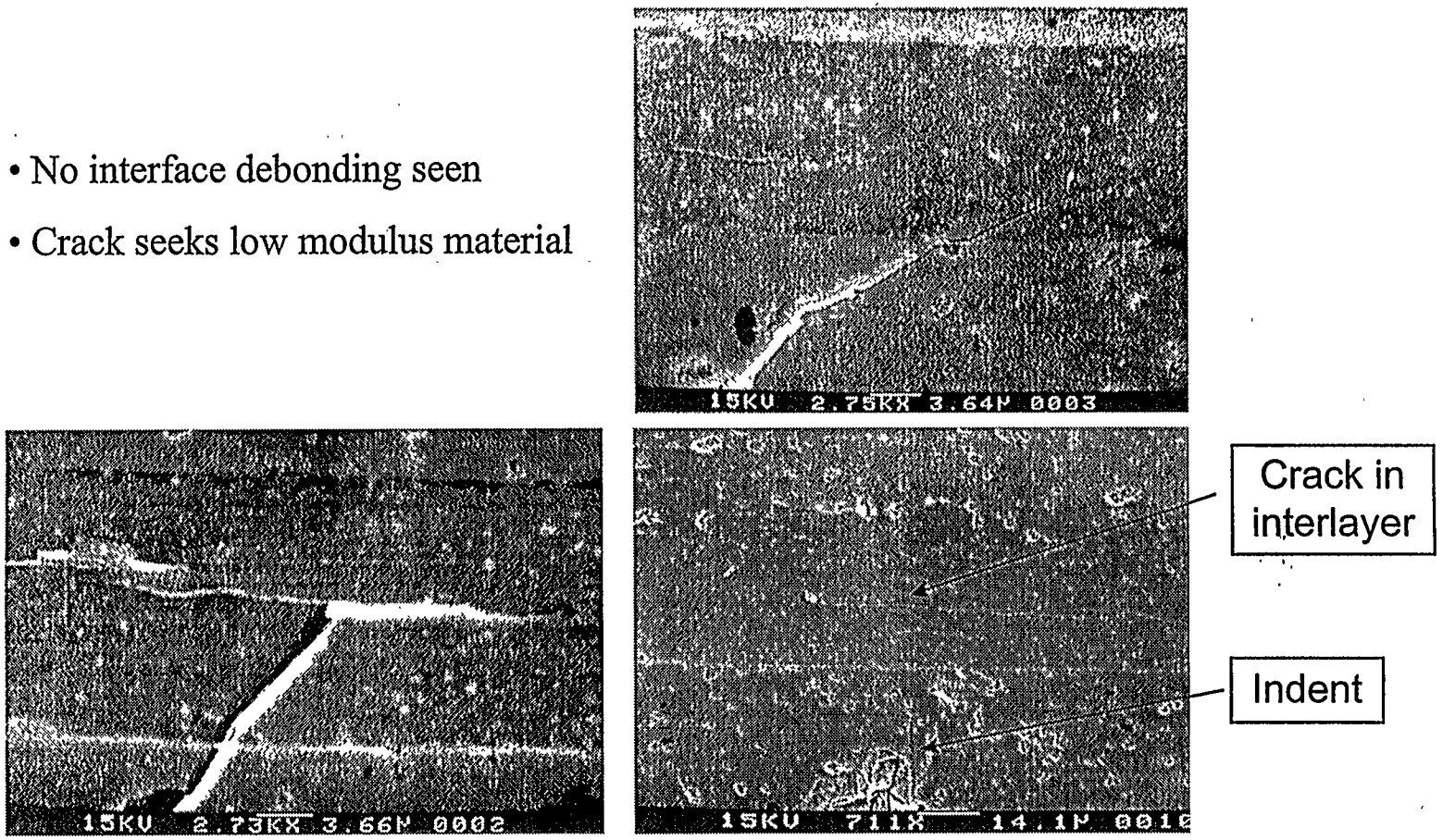

Figure 2-16. Indentation crack path in joints of increasing thickness. 35 micron joint cracked, although indent did not reach interface .

$$\cos\theta = \frac{\gamma_{sv} - \gamma_{sl}}{\gamma_{lv}}$$

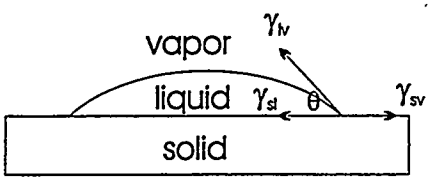

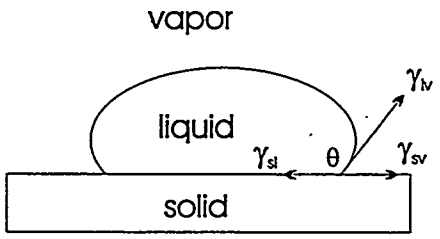

Wetting: $\theta < 90$

Nonwetting: $\theta > 90$

Figure 3-1 Wetting and Contact Angle

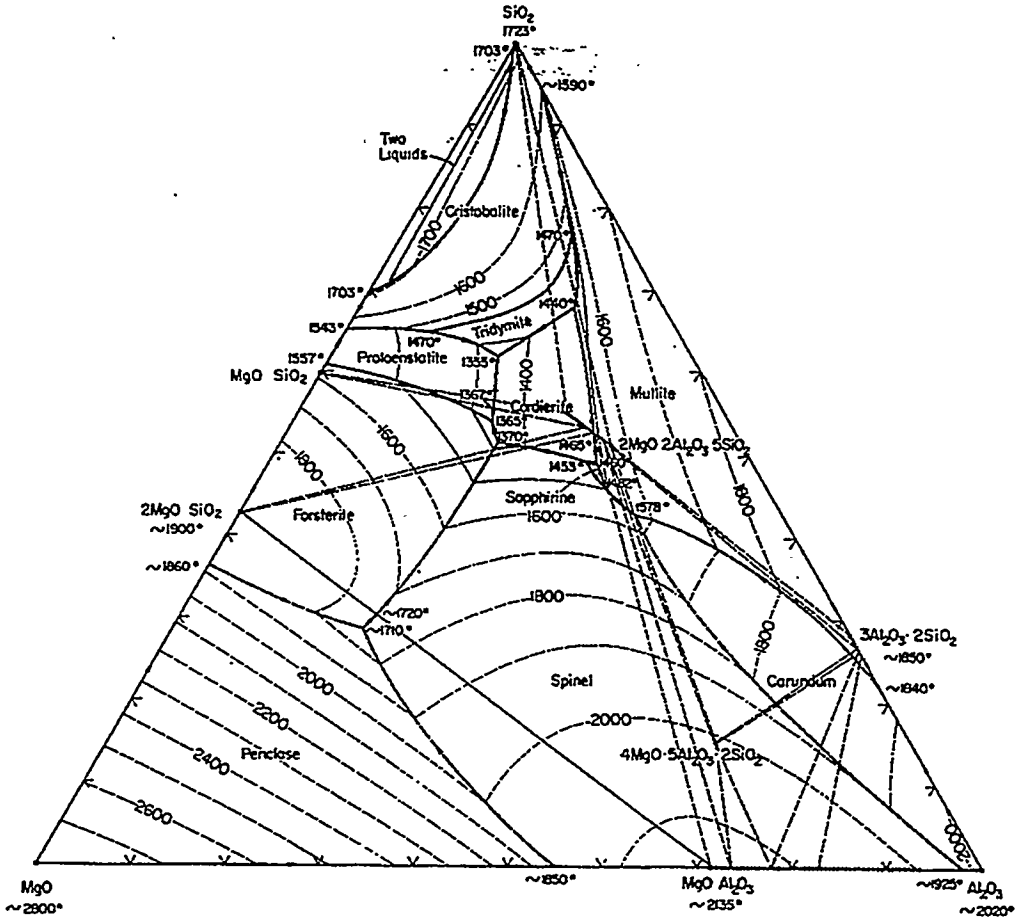

Figure 3-2. MgO-Al_2O_3-SiO_2 system, after E. Levine and H. McMurdie; *Phase Diagrams for Ceramists*, Vol. 3, Am. Ceram. Soc., Westerville, OH (1975).

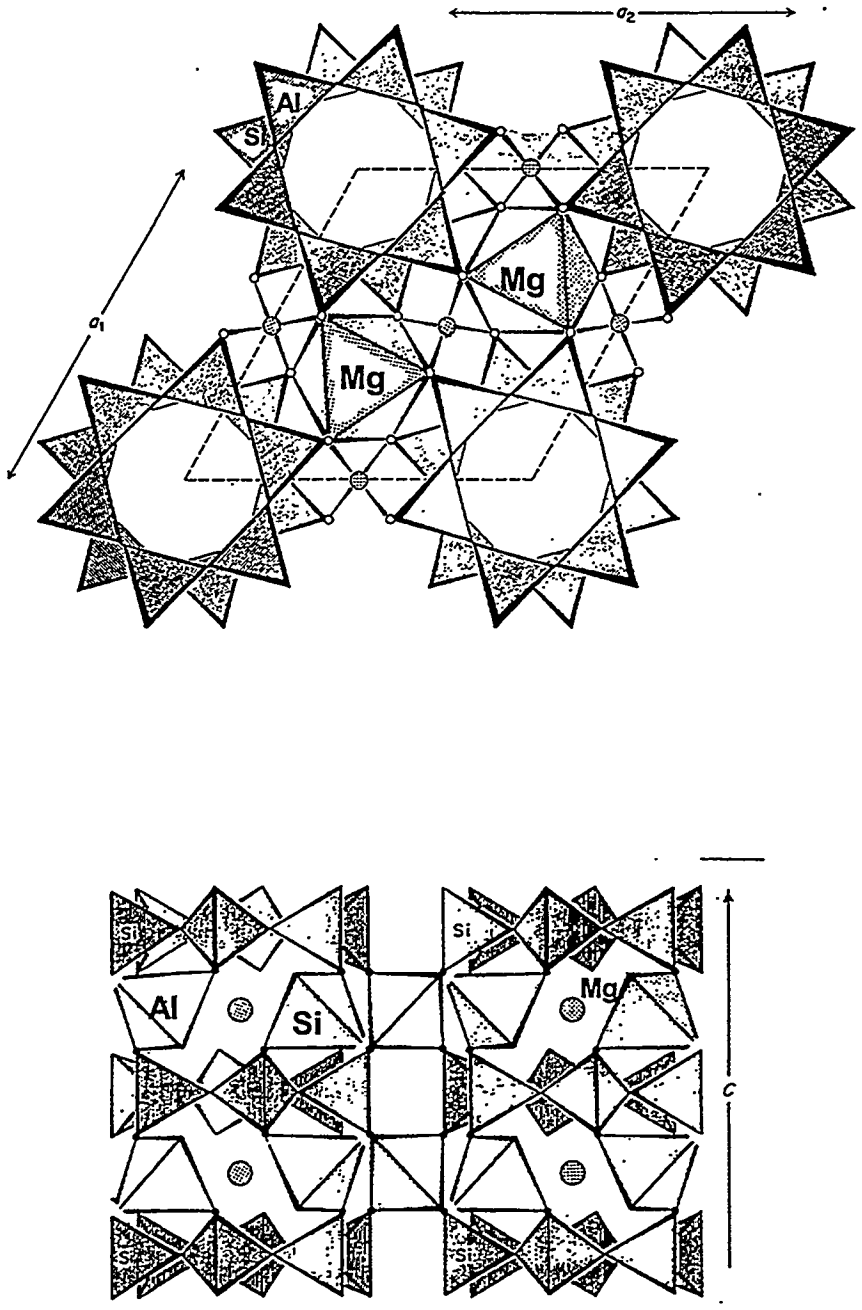

Figure 3-3. Crystal Structure of Cordierite

- Cordierite glass-ceramic, when fired rapidly, remains amorphous and can be crystallized during a subsequent heat treatment
  - Nucleating agents: TiO_2, BaO, e.g.

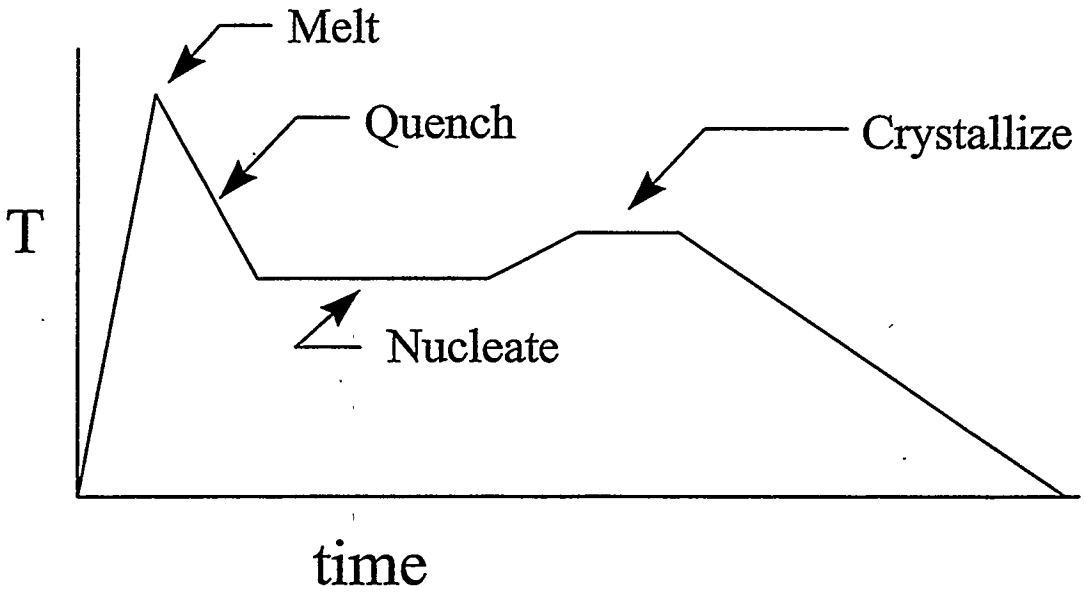

Figure 4-1. Heating schedule for bonding with glass-ceramic materials.

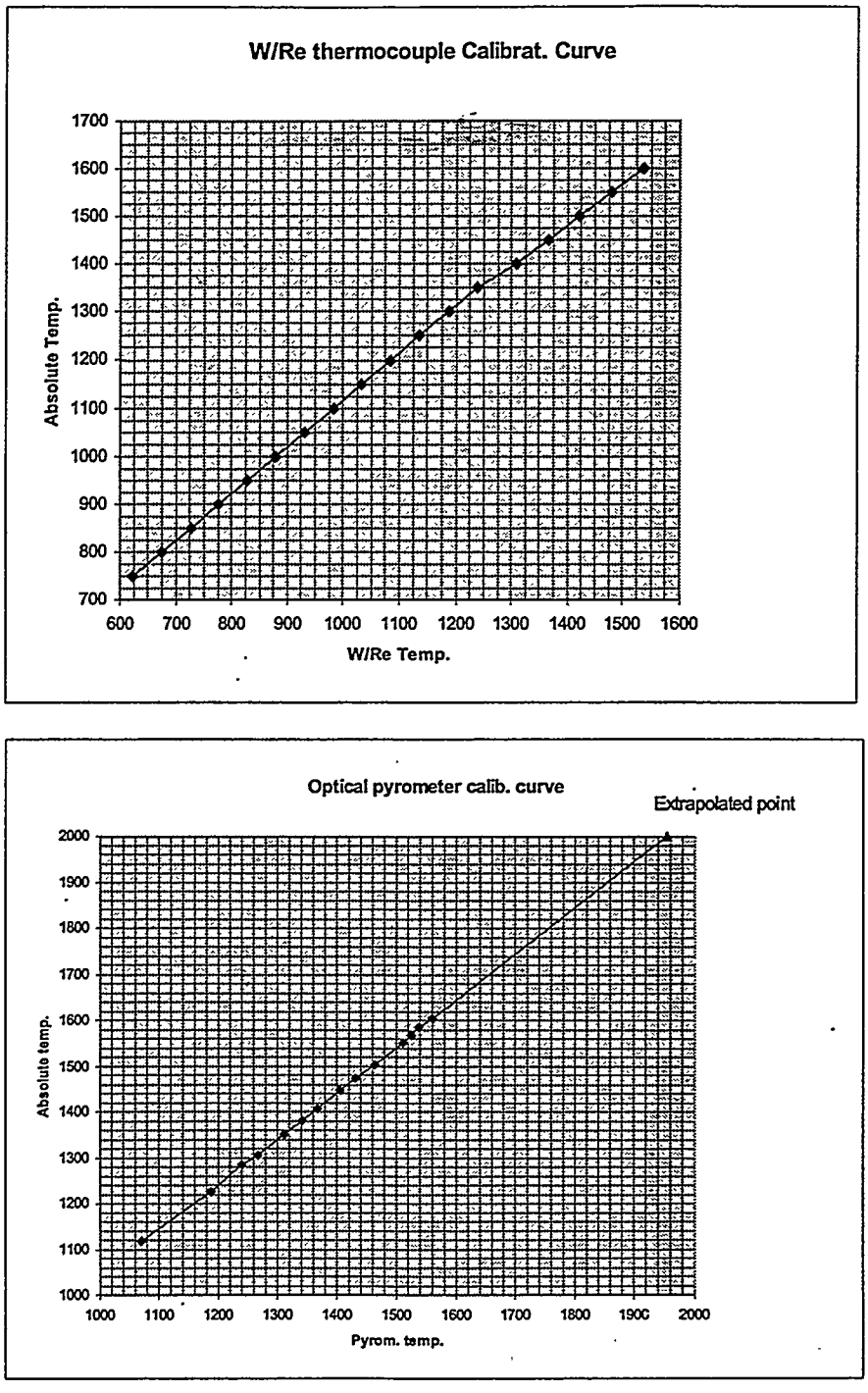

Figure 4-2. Temperature calibration curves for graphite element furnace.

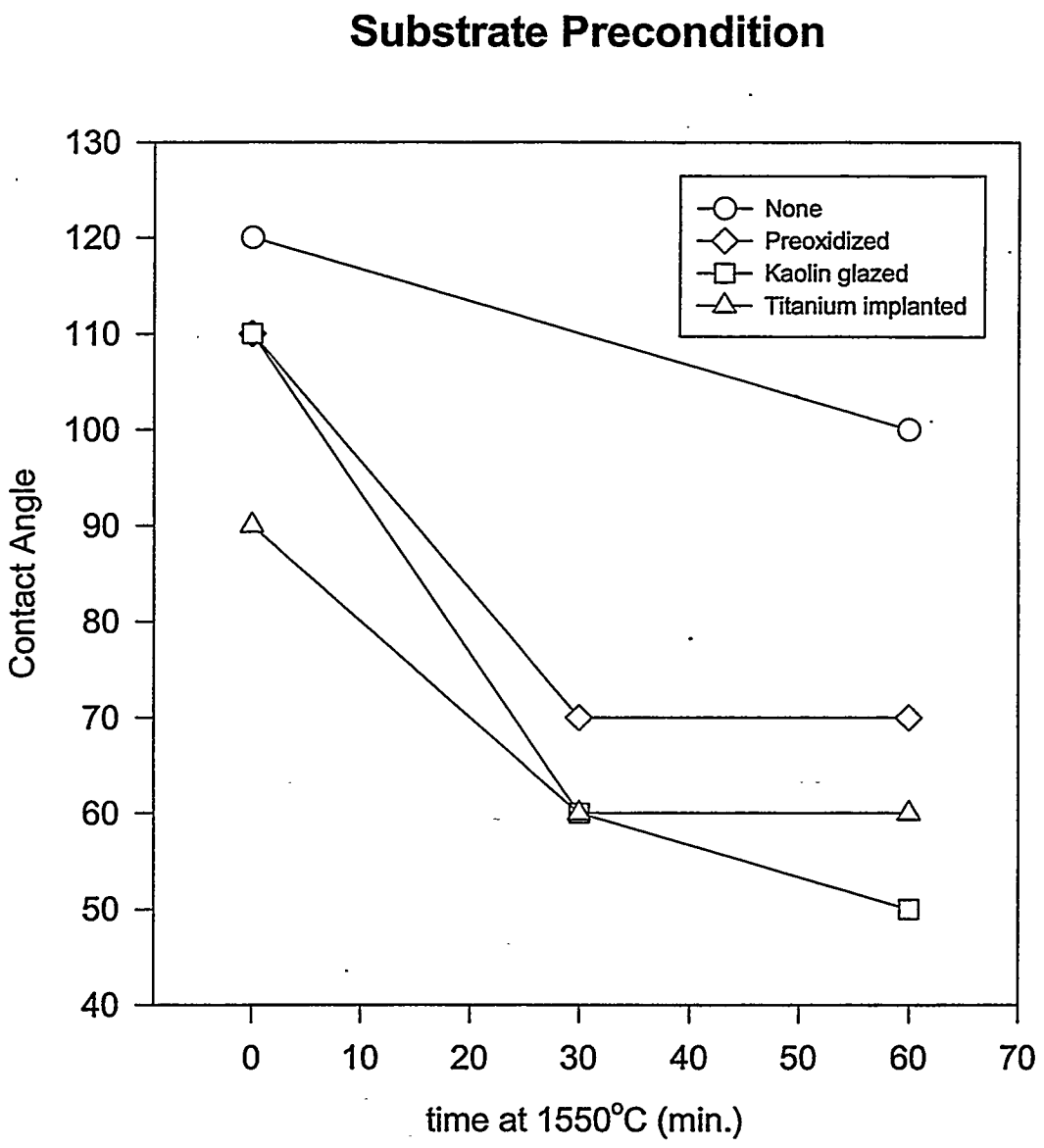

Figure 5-1. Effect of substrate precondition on contact angle.

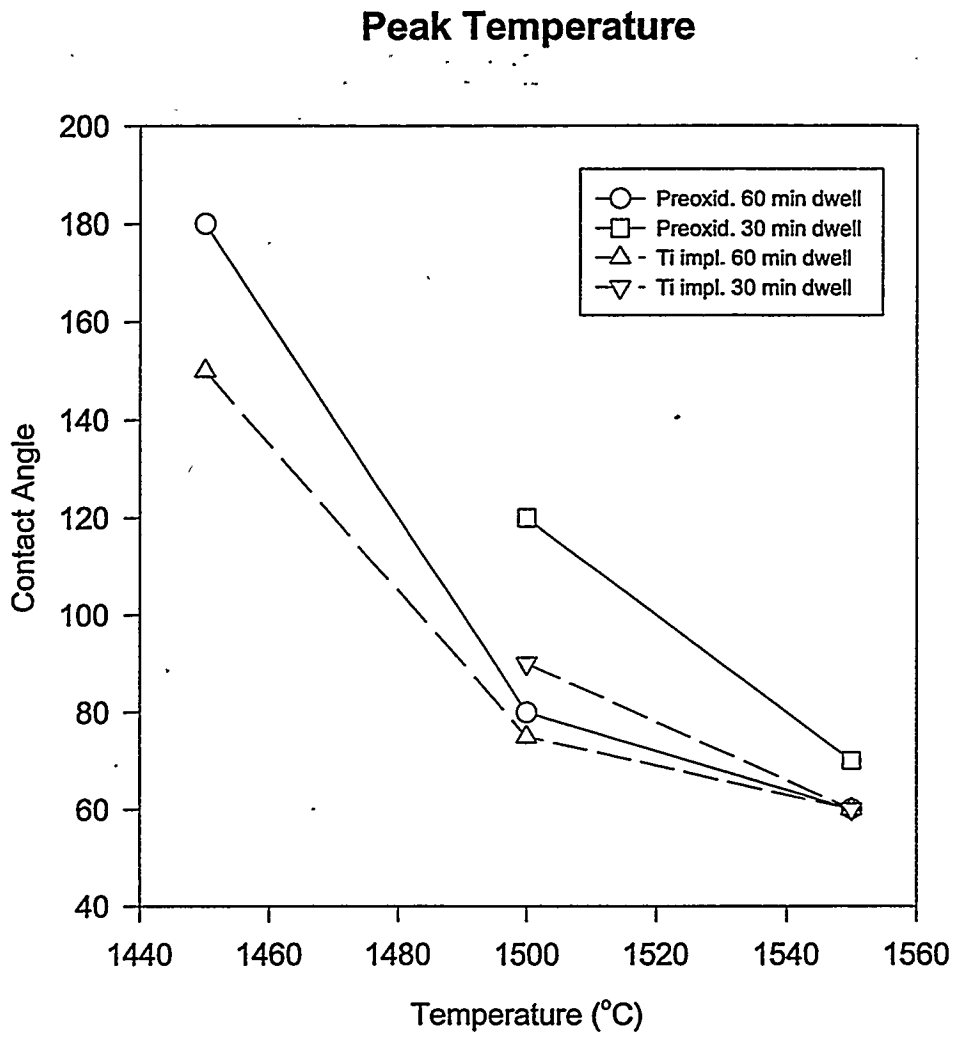

Figure 5-2. Effect of peak temperature on contact angle.

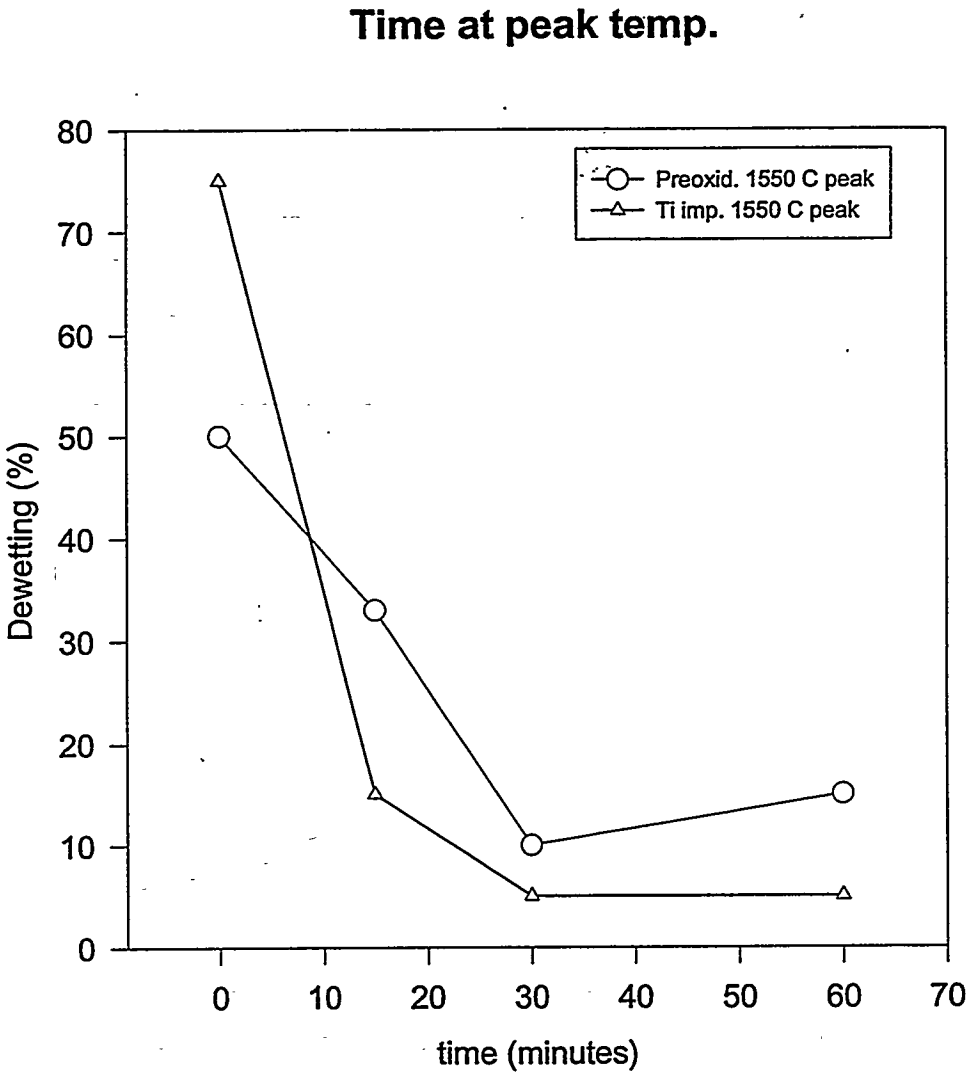

Figure 5-3. Effect of peak dwell time on interfacial voiding.

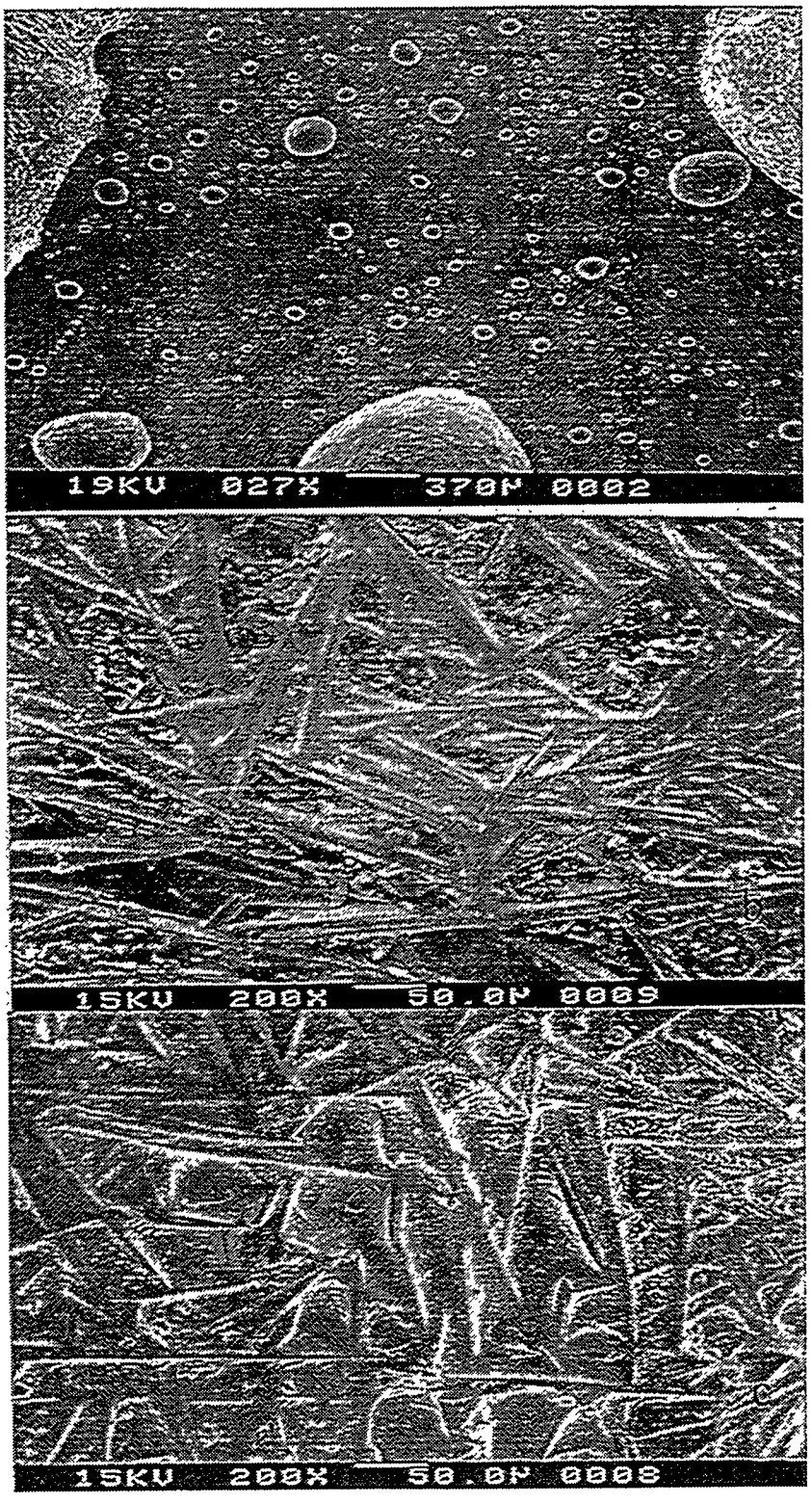

Figure 5-4. Phase separation in glass (a); SEM micrograph of droplet on right-hand side (b); SEM micrograph of droplet on left-hand side (c).

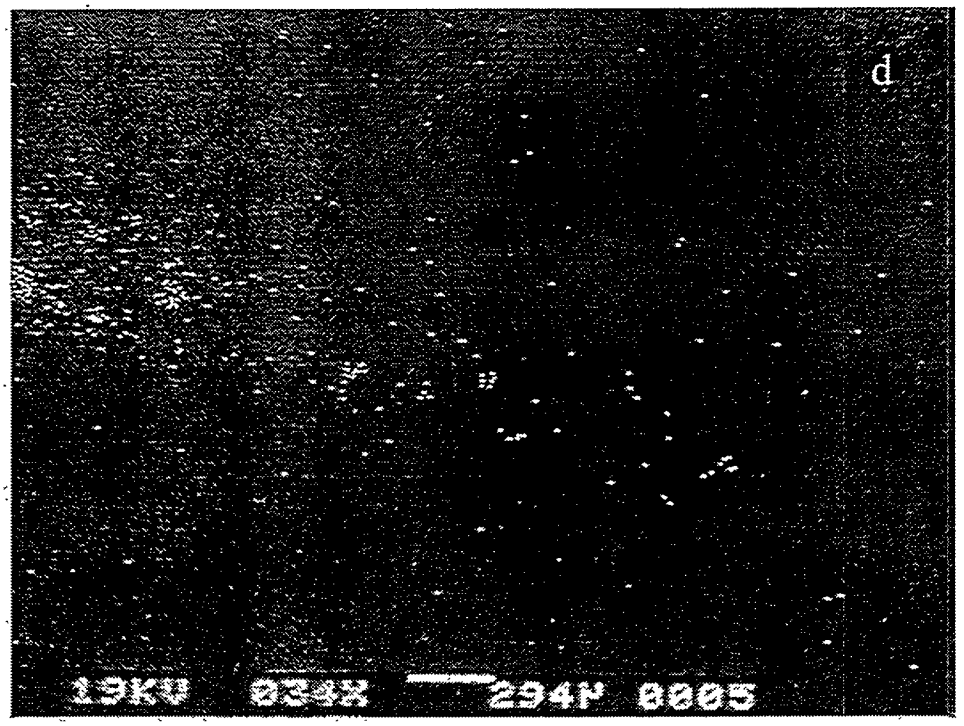

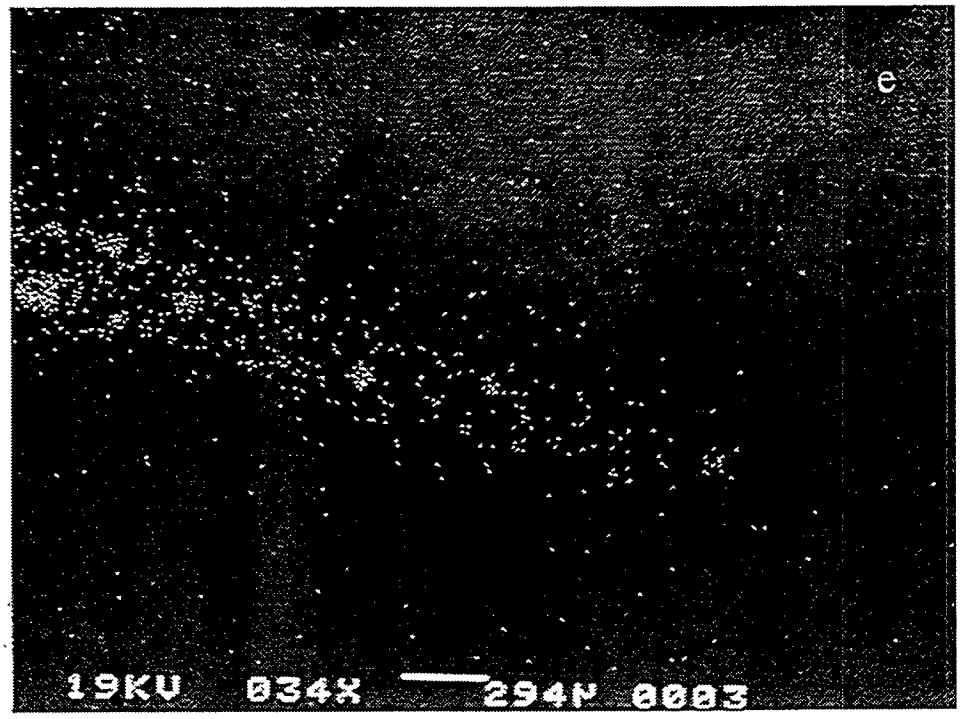

Figure 5-4. X-ray maps of phase separated glass droplets indicating d) enrichment of Mg; and e) enrichment of Al, in the wetting phase.

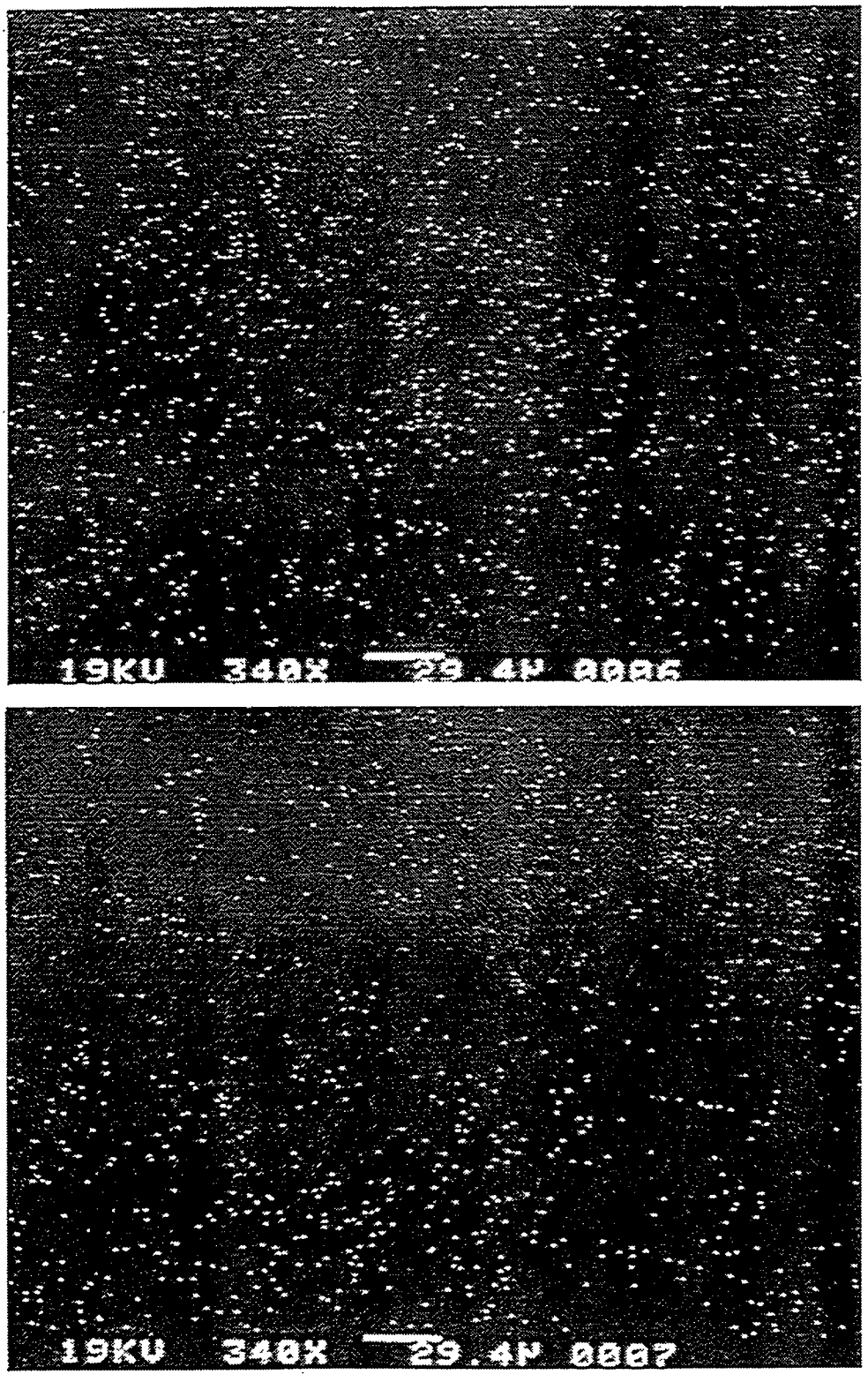

Figure 5-4f. Barium x-ray map of wetting (top) and nonwetting (bottom) glass phases after phase separation, denoting Ba-rich wetting phase.

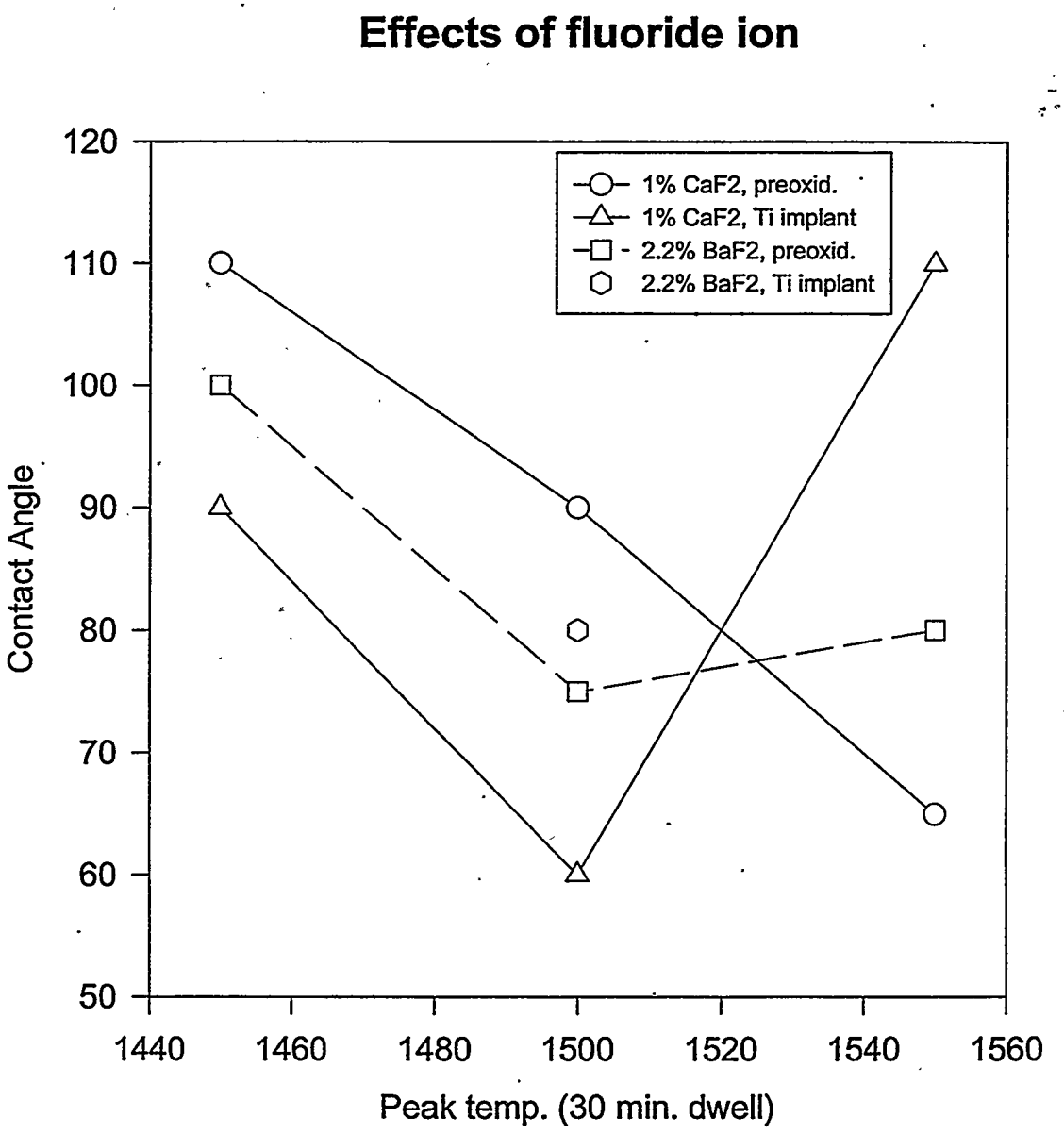

Figure 5-5. Effects of fluoride ion flux on contact angle.

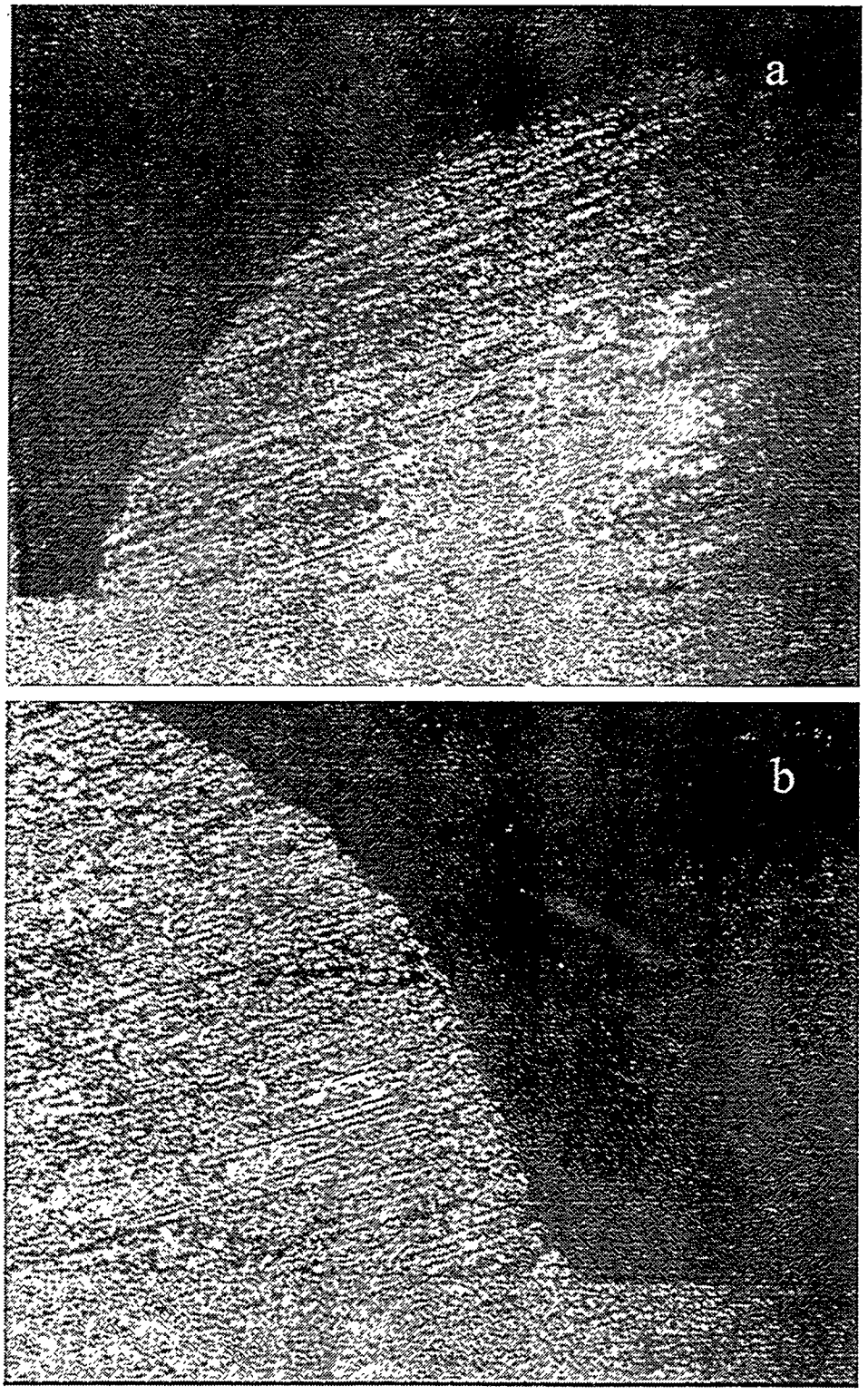

Figure 5-6. Optical micrographs (50X) of a) sessile drop fired at 1550°C, 30 min. ($\theta = 68^{\circ}$); and b) sessile drop with 1 wt. % CaF_2, fired at 1500°C, 30 min. ($\theta = 46^{\circ}$).

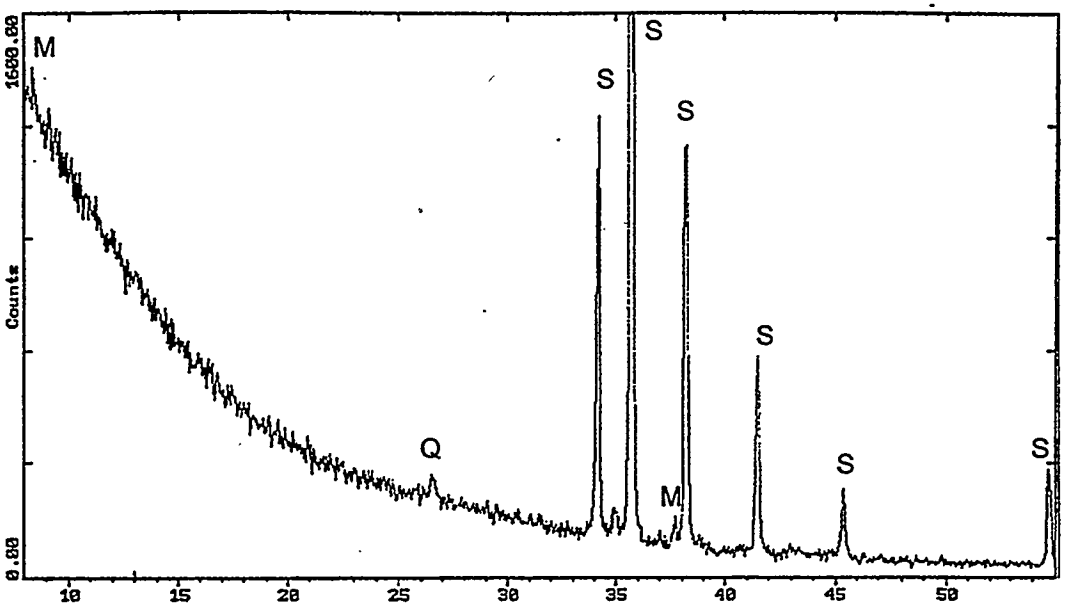

Figure 5-7. Thin-film x-ray spectrum (2°) of interfacial reaction phase on preoxidized substrate. S = SiC, Q = quartz, M = $Mg_3Si_2O_5(OH)_4$.

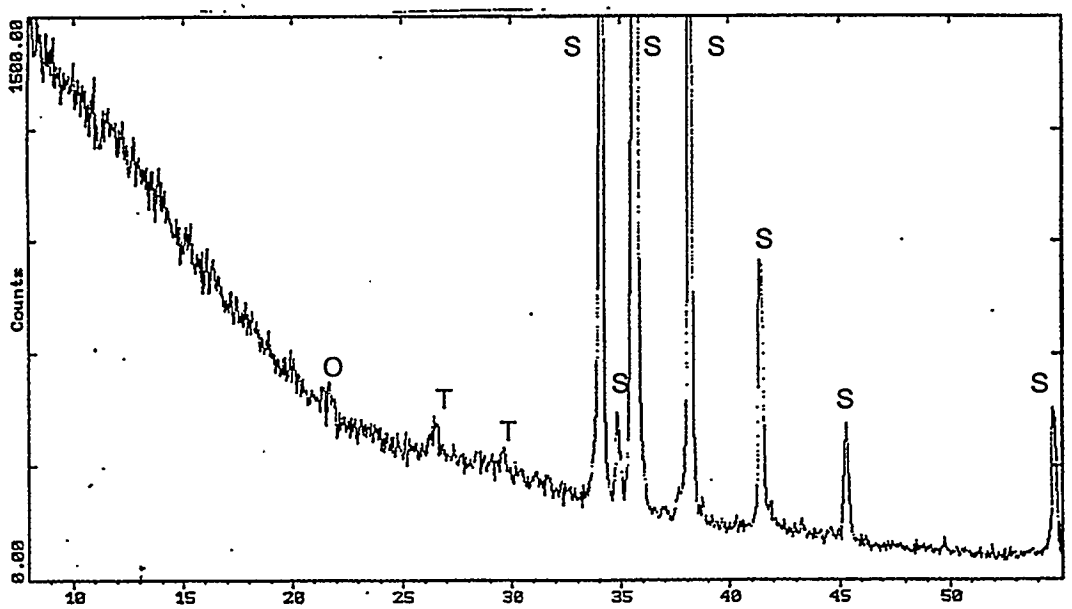

Figure 5-8. Thin-film x-ray spectrum (2°) of interfacial reaction phase on titanium ion-implanted substrate. S = SiC, T = Ti_7O_{13}, O = silicon oxide.

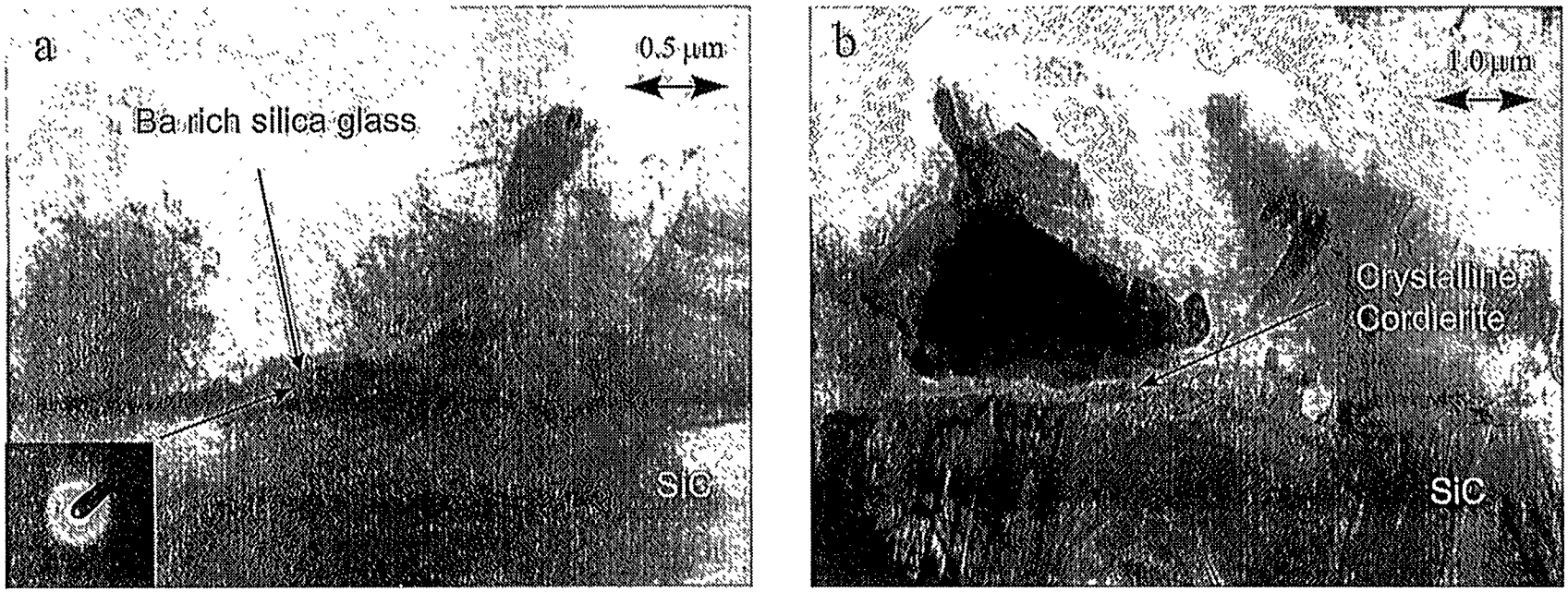

Figure 5-9. TEM of Cordierite/SiC interface after a) 1 hr. nucleation time; and b) 5 hr. nucleation time. Longer dwell promotes precipitation of the barium precursor phase. Crystallized 2 hr. at 1200°C. TEM courtesy of Dr. W. MoberlyChan.

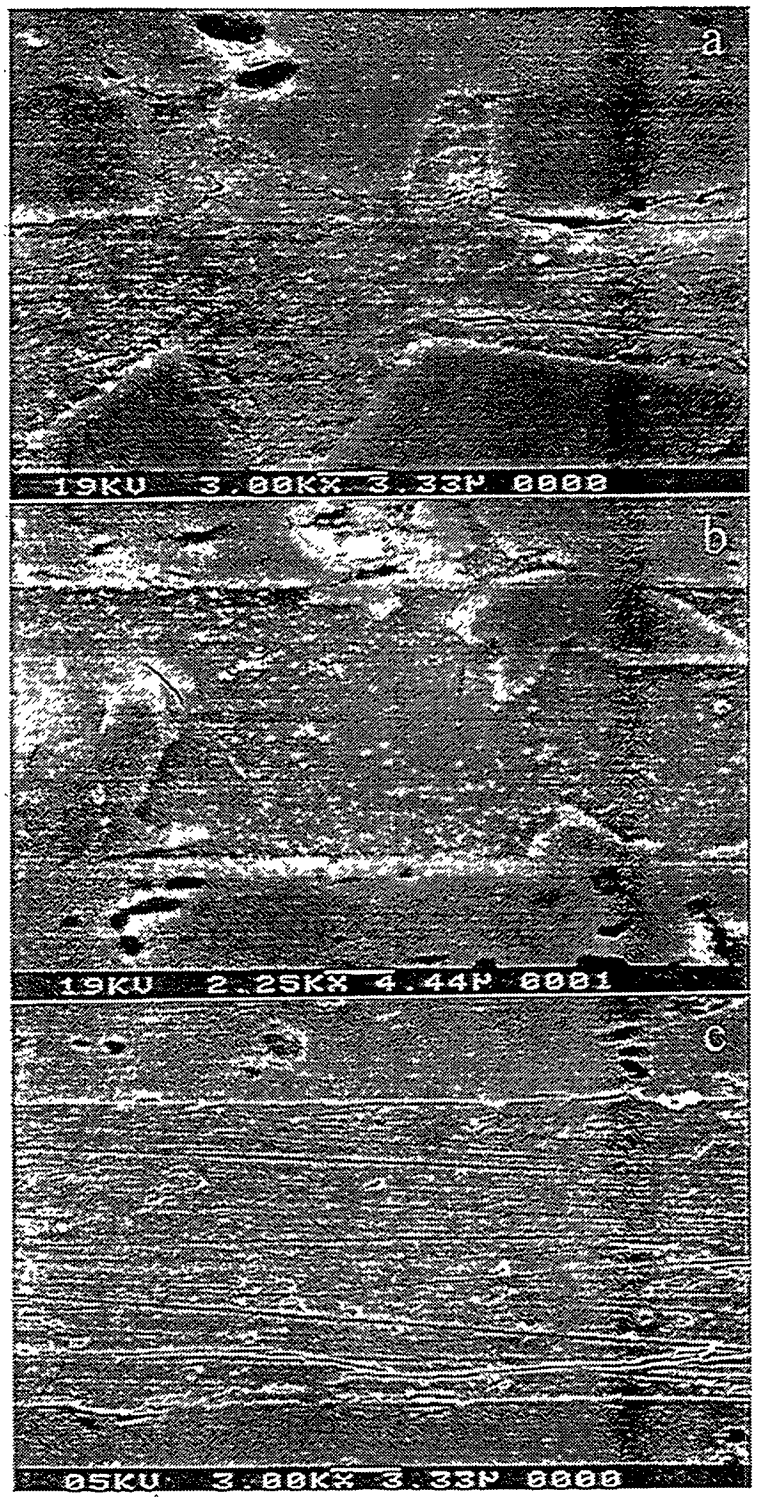

Figure 5-10. Effect of quench rate on phase morphology. Slow cooling (10°C/min) resulting in a) mullite nucleation; and b) cordierite nucleation at the interface. Rapid quench (25°C/min) resultingin amorphous joint, (c). Samples were examinced prior to crystallization heat treatment.

Figure 5-11. TEM of interlayer, with characteristic morphologies of cordierite (dendritic), and mullite (polygonal). TEM courtesy of Dr. W. MoberlyChan.

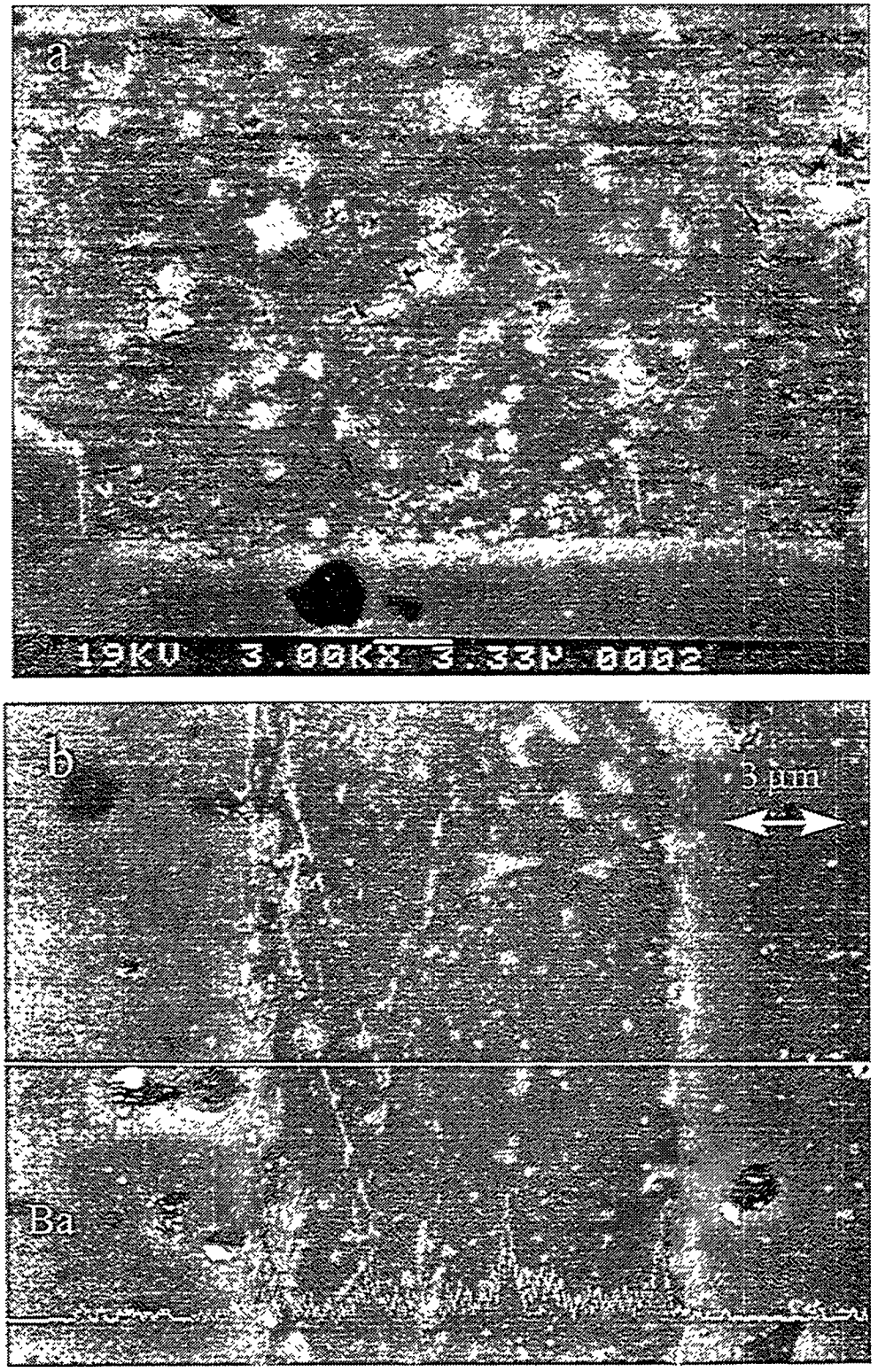

Figure 5-12. Joint morphology after 5 hr. nucleation dwell at 850°C (a); and WDS barium line scan depicting secondary phase barium enrichment (b).

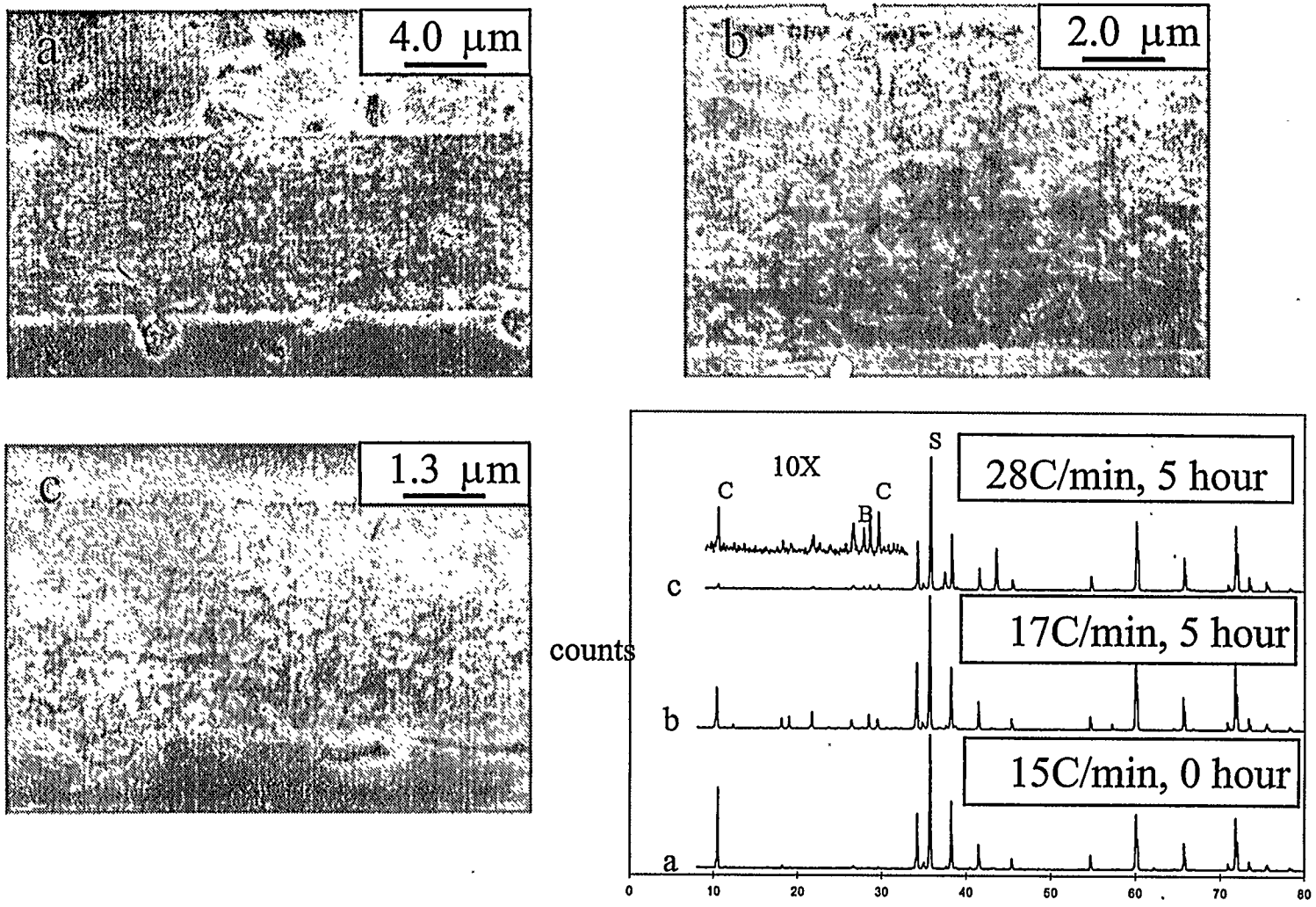

Figure 5-13. Evolution of fine-grained equiaxed microstructure obtained with high quench rate and 5 hr. nucleation dwell.

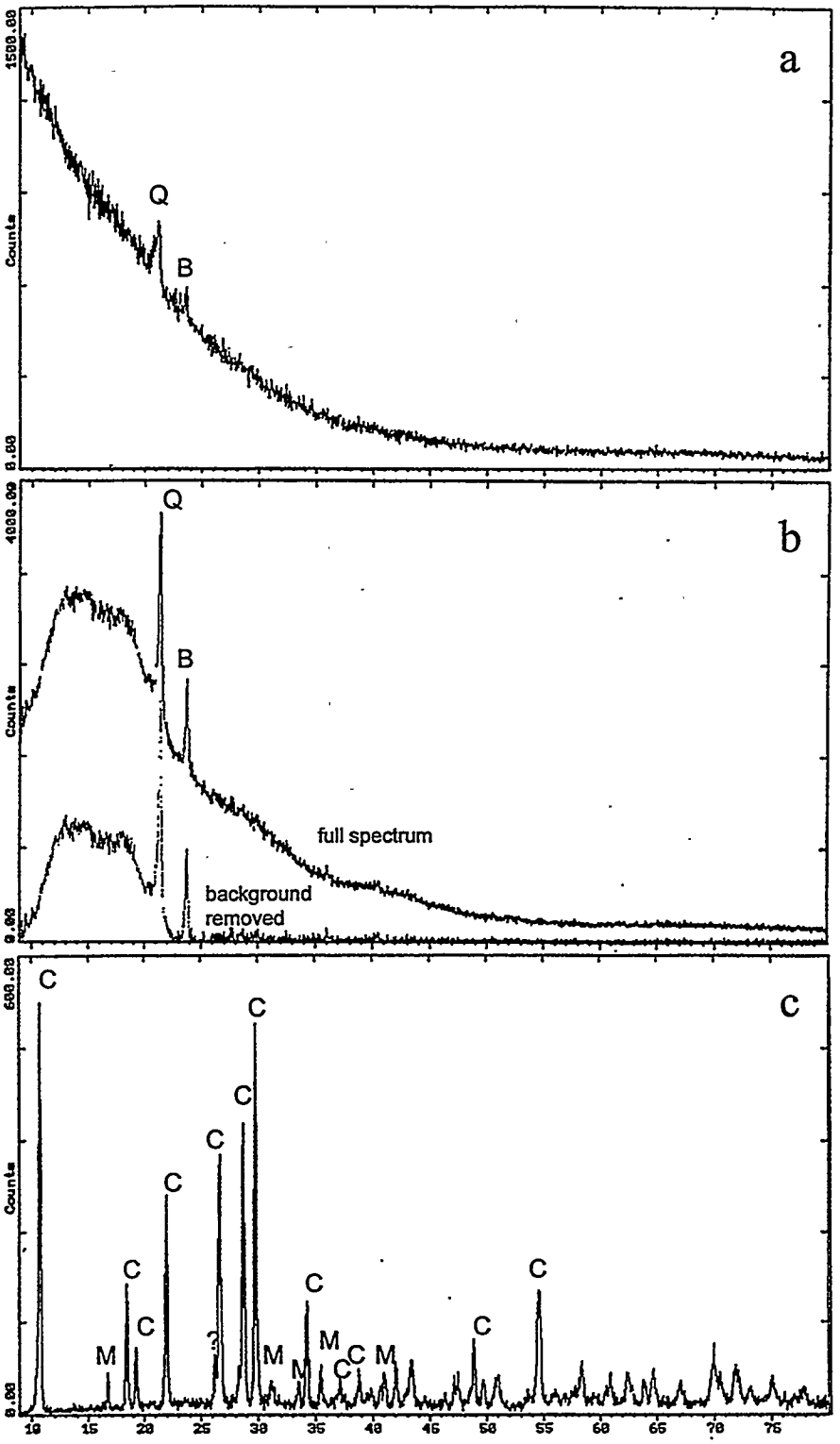

Figure 5-14. Thin-film x-ray spectra (2°) of cordierite powder, a) removed after quench; b) removed after quench and 5 hr. nucleation dwell; and c) removed after full process. Q = stuffed β-quartz, B = 3 $BaO \cdot 5SiO_2$, C = cordierite, M = mullite, ? = sanbornite?

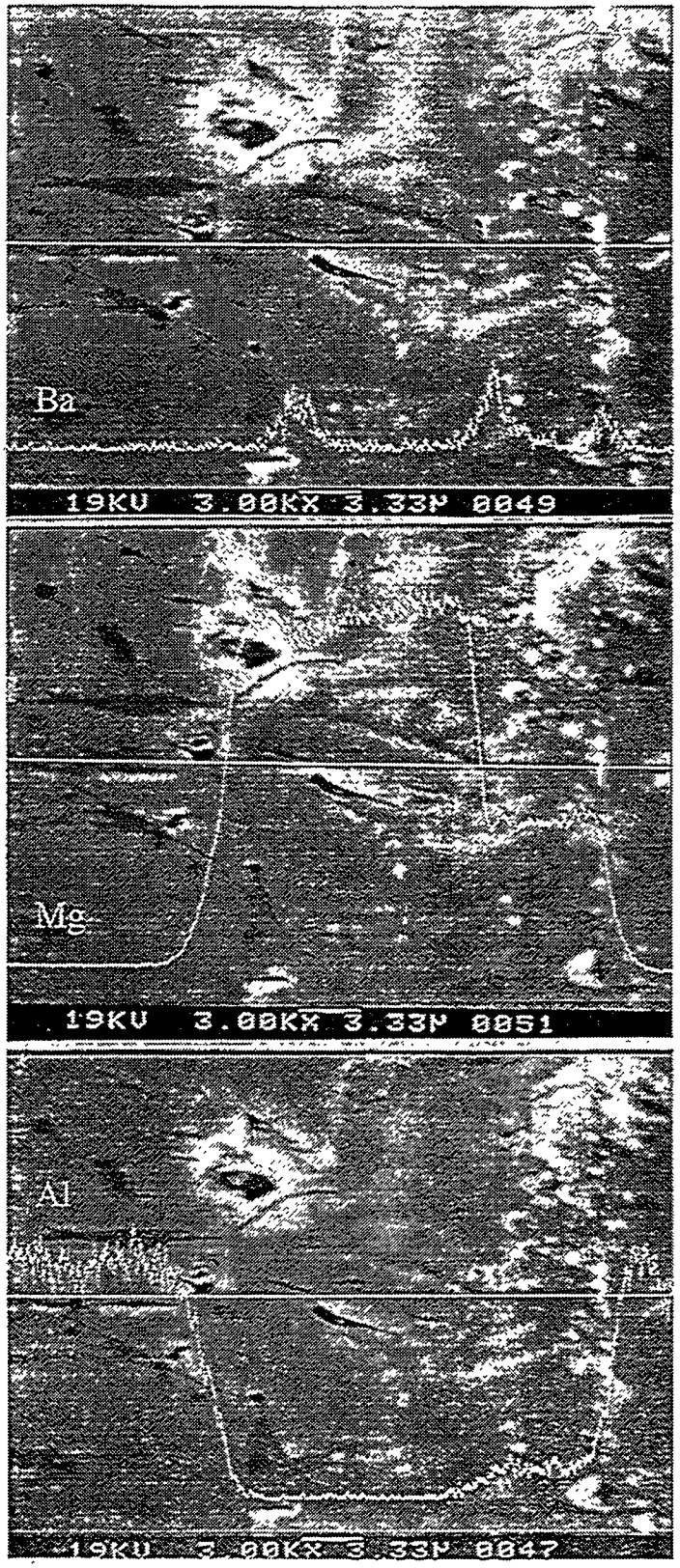

Figure 5-15. WDS line scans across cordierite joint.

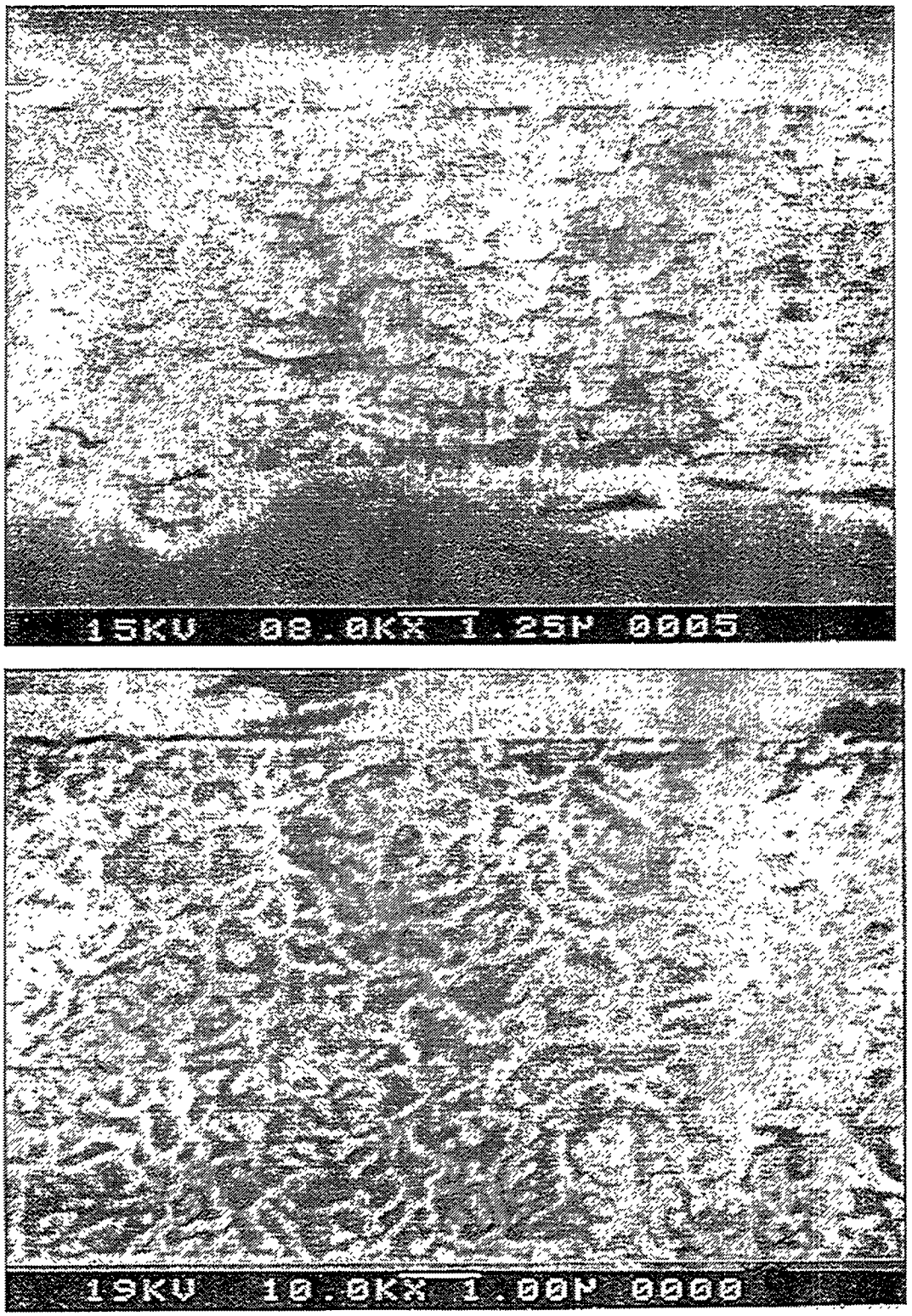

Figure 5-16. SEM micrographs of cordierite joints after full process (1.5 hr. crystallization at 1200°C).

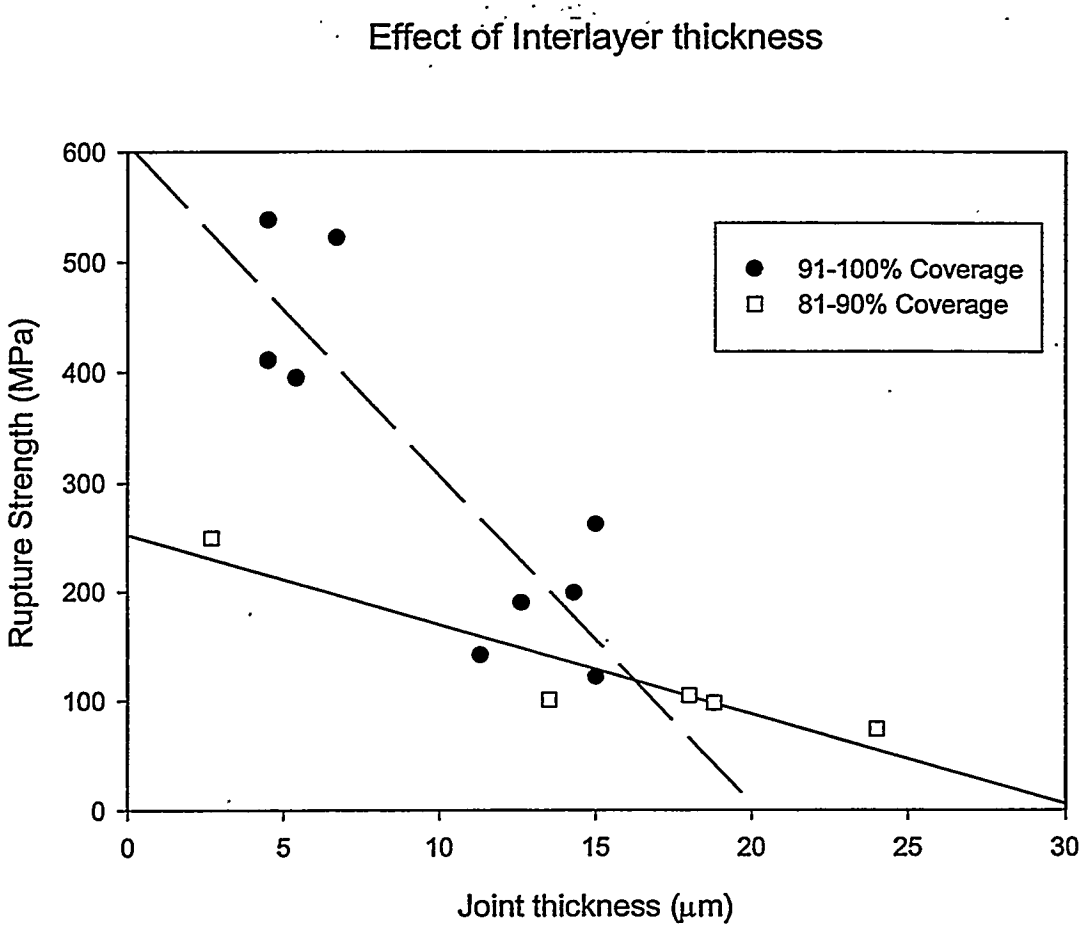

Figure 5-17. Effect of interlayer thickness on rupture strength, for SiC/Cordierite joints with preoxidized substrates.

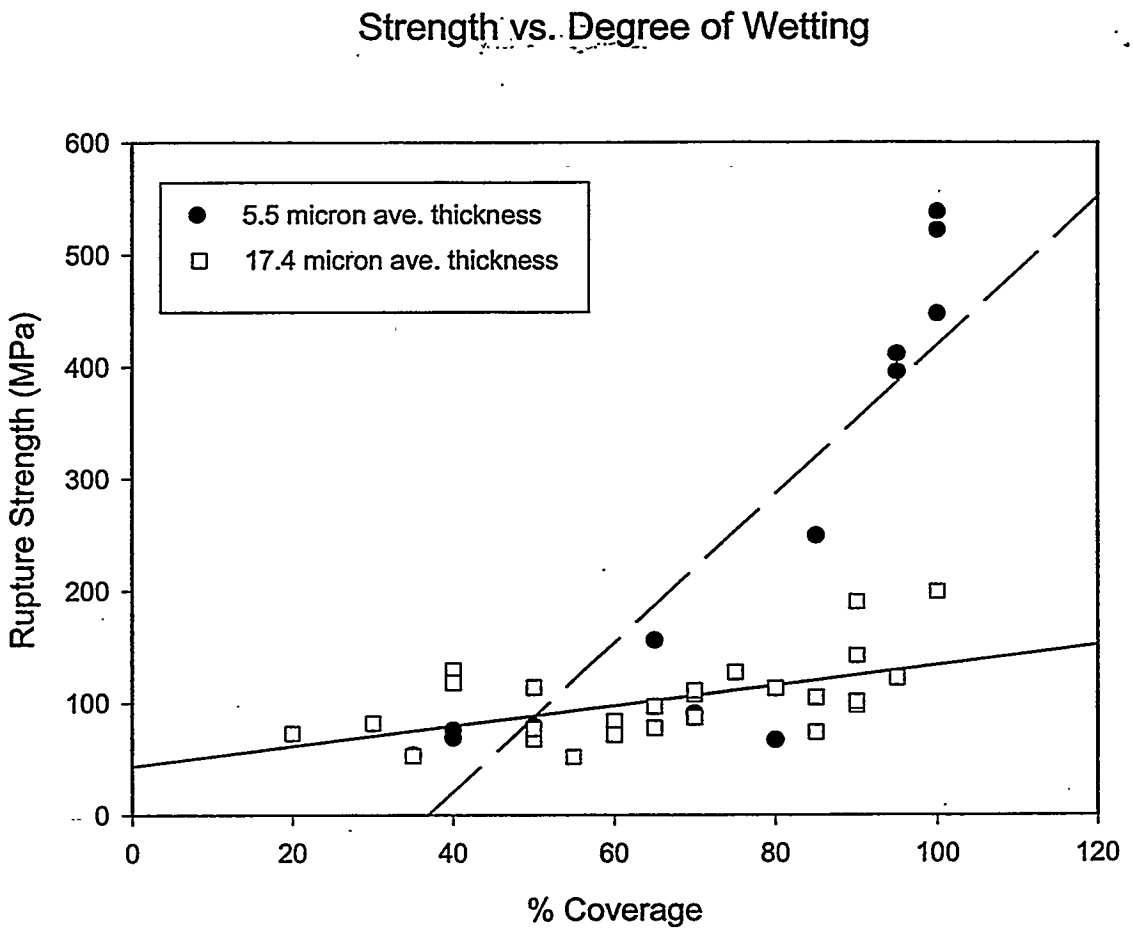

Figure 5-18. Effect of wetting coverage on rupture strength, for SiC/Cordierite joints with preoxidized substrates.

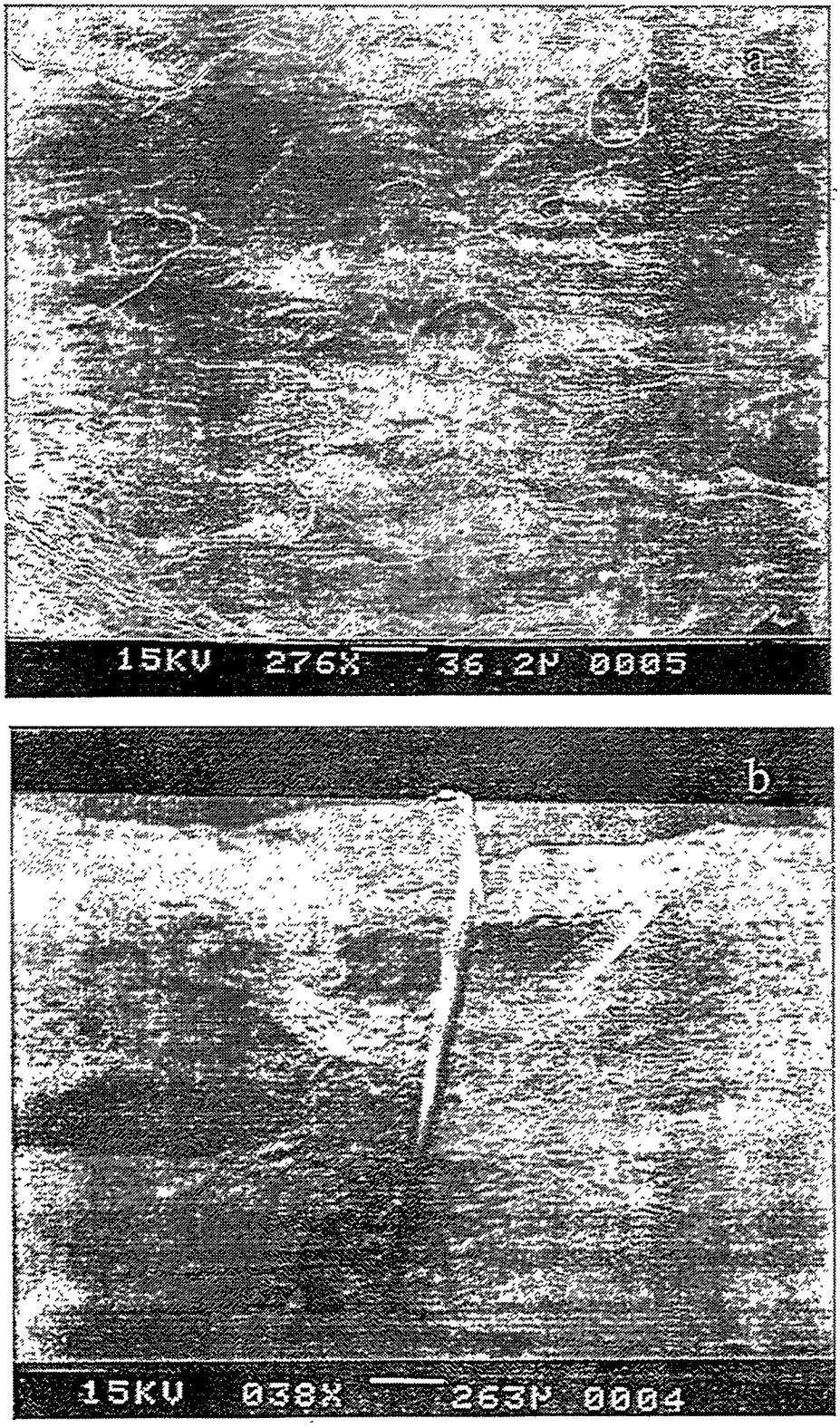

Figure 5-19. Fracture surface of SiC joined with cordierite illustrating a) faceted cordierite fracture; and b) failure in ceramic on opposing SiC beam surfaces.

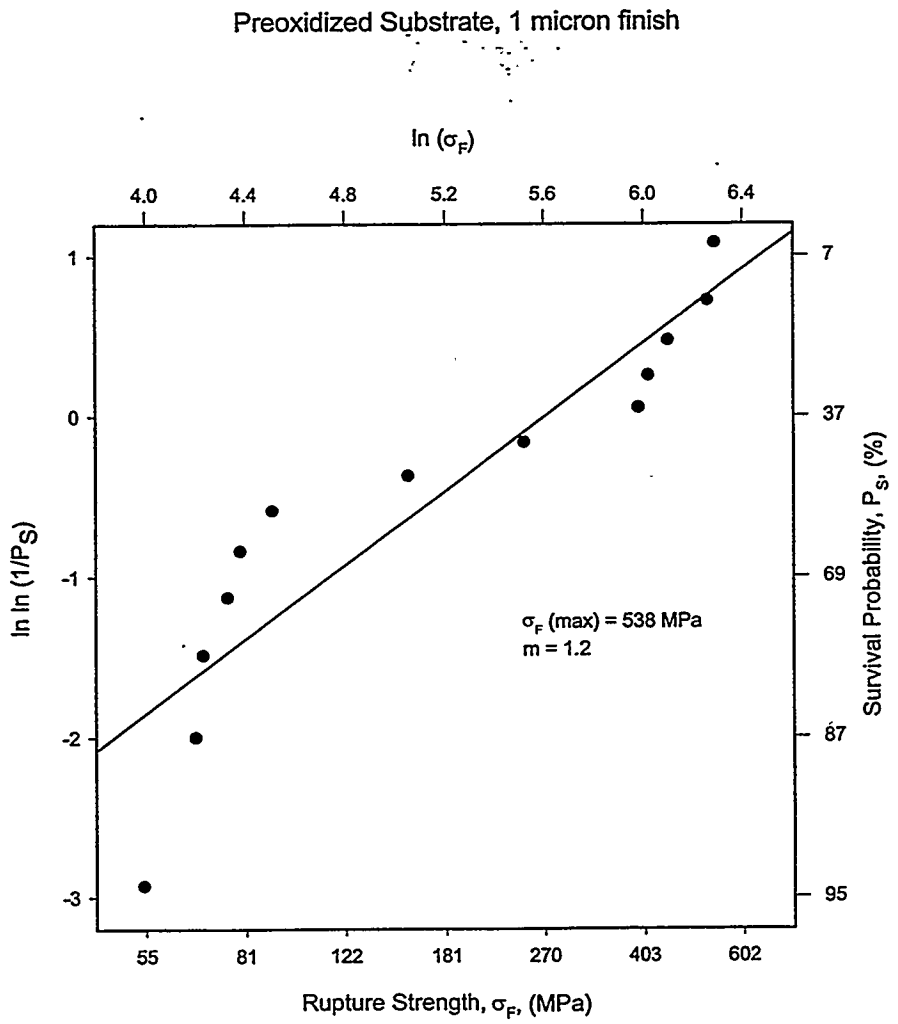

Figure 5-20. Weibull distribution of rupture strength of SiC/Cordierite joints, depicting two distributions dependent upon surface coverage.

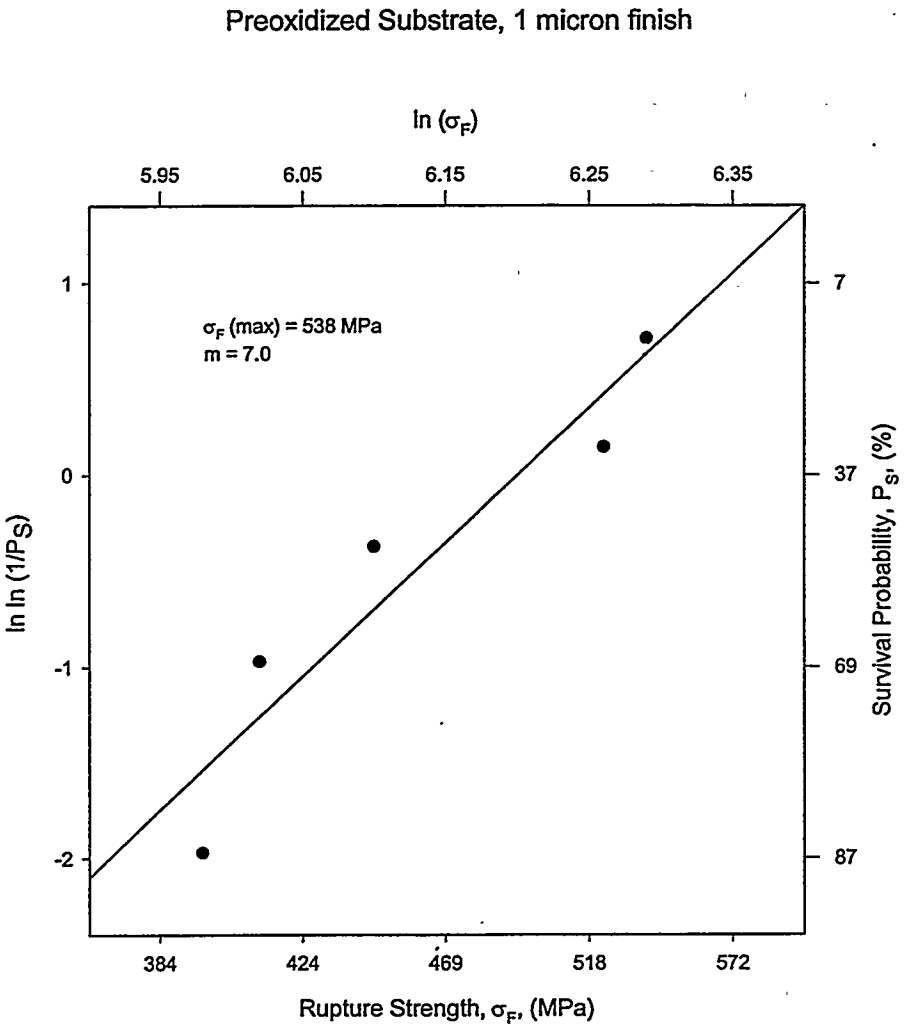

Figure 5-21. Weibull distribution of rupture strength of SiC/Cordierite joints, showing sample set with wetting coverage > 85%.

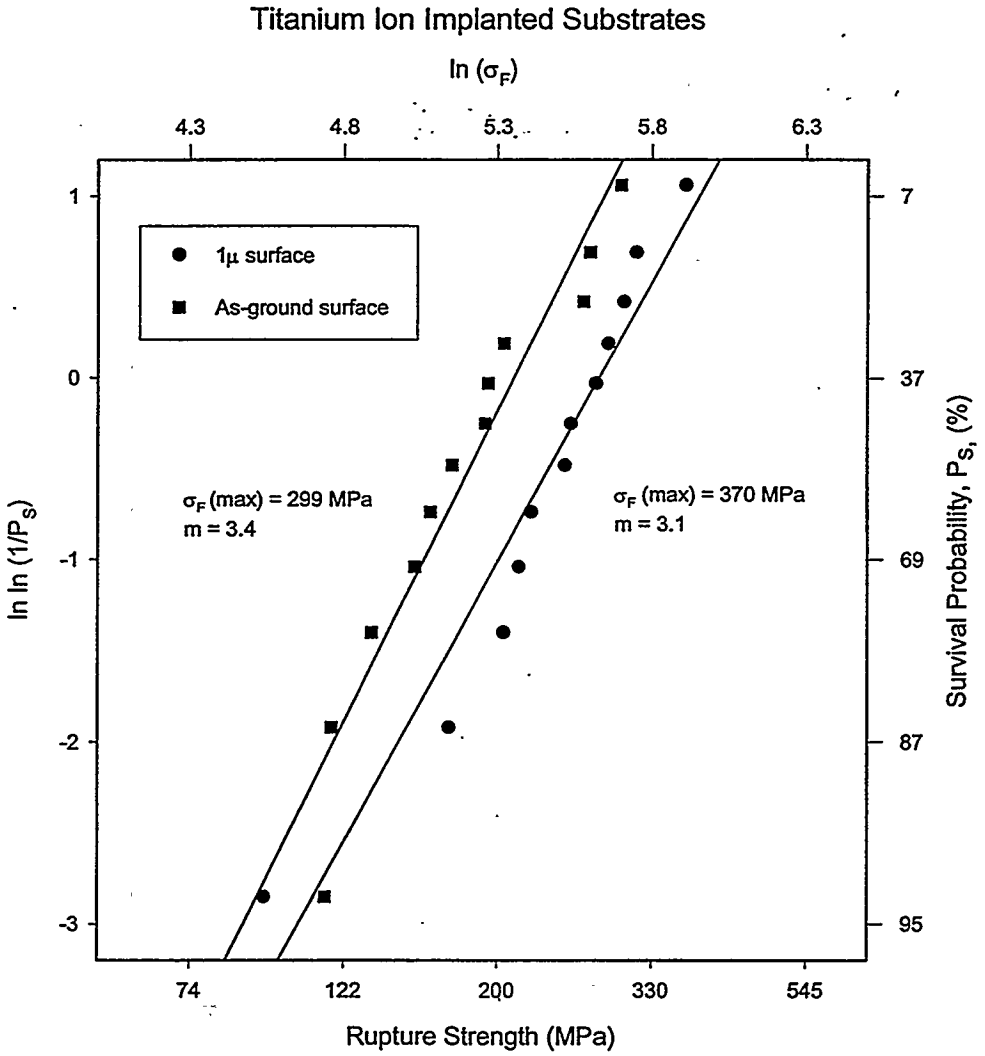

Figure 5-22. Weibull distributions of rupture strength of SiC/Cordierite joints, with titanium ion-implanted substrates, showing higher strength for 1 μm surface finish.

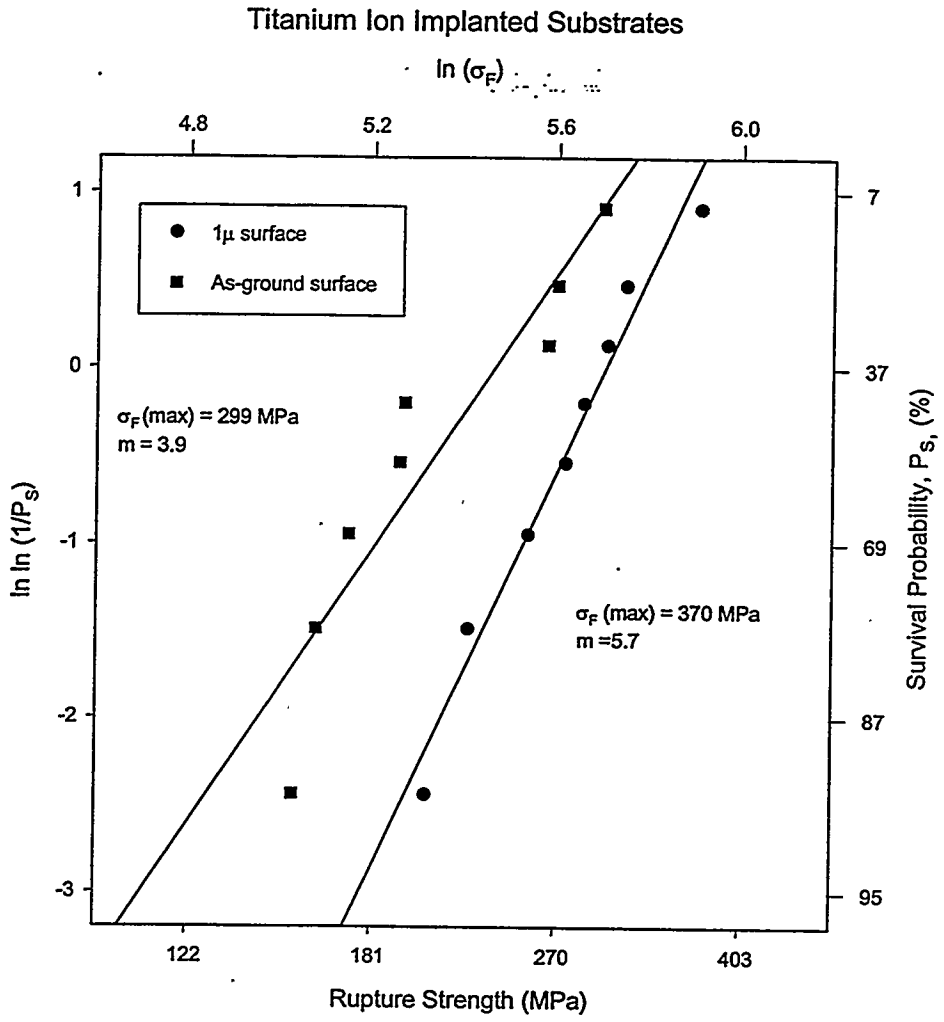

Figure 5-23. Weibull distributions of rupture strength of SiC/Cordierite joints with titanium-ion implanted substrates, showing sample set with wetting coverage > 85%.